

# Non-classical photon-phonon correlations at room temperature

Présentée le 13 août 2021

Faculté des sciences de base  
Groupe Galland  
Programme doctoral en physique

pour l'obtention du grade de Docteur ès Sciences

par

**Santiago TARRAGO VELEZ**

Acceptée sur proposition du jury

Prof. O. Yazyev, président du jury  
Prof. C. M. G. Galland, directeur de thèse  
Prof. V. Lorenz, rapporteuse  
Prof. B. Sussman, rapporteur  
Dr N. J. Engelsen, rapporteur



# Acknowledgements

I'd like to give my most sincere thank you to everyone who played a role in the development of my PhD.

To Professor Christophe Galland, for giving me a chance to pursue research in his lab, and for offering an endless supply of support and motivation throughout this journey.

To Dr. Mitchell Anderson, who taught me how to do experimental work in optics when I arrived in Lausanne, and who I'm lucky to count on as a friend.

To Dr. Anna Pogrebna, for her support and friendship; working in the lab would not have been the same without you.

To Aqeel Ahmed, Hossein Babashah, and Arslan Raja my office-mates (honorary office-mate, in the case of Arslan), for their friendship, support, and camaraderie.

To Tianqi Zhu, Nils Kipfer, Sakthi Priya, Sachin Suresh, Wen Chen, Valeria Vento, Shahwat Kumar, Elena Losero, Martin Pototschnig, and all the people who passed through LQNO during my stay.

To all my friends and family for their unconditional love and support. I would not have been able to do this without you.

*Lausanne, July 30, 2021*

Santiago Tarragó Vélez



# Abstract

With the development of quantum optics, photon correlations acquired a prominent role as a tool to test our understanding of physics, and played a key role in verifying the validity of quantum mechanics. The spatial and temporal correlations in a light field also reveal information about its origin, and allow us to probe the nature of the physical systems interacting with it. Additionally, with the advent of quantum technologies, they have acquired technological relevance, as they are expected to play an important role in quantum communication and quantum information processing.

This thesis develops techniques that combine spontaneous Raman scattering with Time Correlated Single Photon Counting, and uses them to study the quantum mechanical nature of high frequency vibrations in crystals and molecules. We demonstrate photon bunching in the Stokes and anti-Stokes fields scattered from two ultrafast laser pulses, and use their cross-correlation to measure the 3.9 ps decay time of the optical phonon in diamond. We then employ this method to measure molecular vibrations in CS<sub>2</sub>, where we are able to excite the respective vibrational modes of the two isotopic species present in the sample in a coherent superposition, and observe quantum beating between the two signals. Stokes scattering, when combined with a projective measurement, leads to a well defined quantum state. We demonstrate this by measuring the second order correlation function of the anti-Stokes field conditional on detecting one or more photons in the Stokes field, which allows us to observe a phonon mode's transition from a thermal state into the first excited Fock state, and measure its decay over the characteristic phonon lifetime. Finally, we use this technique to prepare a highly entangled photon-phonon state, which violates a Bell-type inequality. We measure  $S = 2.360 \pm 0.025$ , violating the CHSH inequality, compatible with the non-locality of the state. The techniques we developed open the door to the study of a broad range of physical systems, where spectroscopic information is obtained with the preparation of specific quantum states. They also hold potential for future technological use, and promote vibrational Raman scattering to a resource in nonlinear quantum optics – where it used to be considered as a source of noise instead.

**Keywords:** Quantum Optics, Raman Spectroscopy, Photon Correlations, Vibrational Dynamics, Phonons, Molecular Vibrations, Entanglement



# Résumé

Avec le développement de l'optique quantique, la mesure des corrélations entre photons a acquis un rôle prépondérant en tant qu'outil permettant de tester notre compréhension de la physique, et joue un rôle clé en ce qui concerne la vérification de la validité de la mécanique quantique. Les corrélations spatiales et temporelles existant au sein d'un champ lumineux révèlent également des informations sur l'origine de ce dernier et nous permettent de sonder la nature des systèmes physiques qui interagissent avec lui. De plus, suite à l'avènement des technologies quantiques, ces corrélations ont acquis une pertinence technologique, car elles sont appelées à jouer un rôle important dans la communication quantique et le traitement de l'information quantique.

Cette thèse développe des techniques qui combinent la diffusion Raman spontanée avec le comptage de photons uniques corrélés dans le temps, et les utilise pour étudier la nature quantique des vibrations à haute fréquence dans les cristaux et les molécules. Nous démontrons le regroupement de photons dans les champs Stokes et anti-Stokes diffusés par deux impulsions laser ultrarapides, et utilisons leur corrélation croisée pour mesurer un temps de déclin de 3,9 ps du phonon optique dans le diamant. Nous utilisons ensuite cette méthode pour mesurer les vibrations moléculaires dans le CS<sub>2</sub>, où nous sommes capables d'exciter les modes vibratoires respectifs des deux espèces isotopiques présentes dans l'échantillon dans une superposition cohérente, et d'observer le battement quantique entre les deux signaux. La diffusion Stokes, lorsqu'elle est combinée à une mesure projective du nombre de photon, conduit à un état quantique pur. Nous le démontrons en mesurant la fonction de corrélation de second ordre du champ anti-Stokes conditionnée par la détection d'un ou plusieurs photons dans le champ Stokes, ce qui nous permet d'observer la transition d'un mode phononique d'un état thermique vers le premier état de Fock excité, et de mesurer son déclin pendant la durée de vie caractéristique du phonon. Enfin, nous utilisons cette technique pour préparer un état photon-phonon hautement intriqué, qui viole une inégalité de Bell. Nous mesurons le paramètre  $S = 2,360 \pm 0,025$ , violant l'inégalité CHSH, compatible avec la non-localité de l'état. Les techniques que nous avons développées ouvrent la voie vers l'étude d'un large éventail de systèmes physiques, où des informations spectroscopiques sont obtenues par la préparation d'états quantiques spécifiques. Elles présentent également un potentiel pour une utilisation technologique future, et élèvent la diffusion Raman vibrationnelle au rang de ressource pour l'optique quantique non linéaire alors qu'elle était auparavant considérée comme une source de bruit.

**Mots-clés :** Optique quantique, spectroscopie Raman, corrélations entre photons, dynamique

## Résumé

---

vibratoire, phonons, vibrations moléculaires, intrication quantique.



# Contents

<b>Acknowledgements</b>	<b>i</b>
<b>Abstract (English/Français)</b>	<b>iii</b>
<b>1 Prologue</b>	<b>1</b>
<b>2 Photon correlations in quantum optics</b>	<b>5</b>
2.1 Second Order Correlation Function . . . . .	6
2.1.1 Non-Classical Values for the Second Order Correlation Function . . . . .	7
2.2 Examples of Photon States and their Statistics . . . . .	8
2.2.1 Coherent States . . . . .	8
2.2.2 Thermal States . . . . .	10
2.2.3 Fock States . . . . .	10
2.3 Two-Mode Squeezed States . . . . .	11
2.3.1 Cross-Correlation Function of a Two-Mode Squeezed State . . . . .	12
2.3.2 Conditional Auto-Correlation Function in a Two-Mode Squeezed State .	13
2.3.3 Independent Auto-Correlation Functions of Two-Mode Squeezed State .	13
2.4 Correlations due to entanglement . . . . .	14
<b>3 Interaction between light and vibration</b>	<b>17</b>
3.1 The Raman Effect . . . . .	17
3.2 Stokes and anti-Stokes interaction . . . . .	18
3.3 Readout through anti-Stokes Scattering . . . . .	20
<b>4 Two-Color Pump-Probe Measurement of Photonic Quantum Correlations Mediated by a Single Phonon</b>	<b>23</b>
4.1 Main Text . . . . .	24
<b>5 Collective Vibrational Quantum Coherence in Spontaneous Raman Scattering</b>	<b>33</b>
5.1 Main text . . . . .	33
<b>6 Preparation and decay of a single quantum of vibration at ambient conditions</b>	<b>45</b>
6.1 Main Text . . . . .	45
6.2 Theoretical description . . . . .	48
6.2.1 Write operation . . . . .	49
	vii

## Contents

---

6.2.2	Read operation . . . . .	50
6.2.3	Statistics of the heralded intensity correlation . . . . .	50
6.3	Experimental Realization . . . . .	52
6.3.1	Setup and measurement procedure . . . . .	52
6.3.2	Ambient thermal state . . . . .	52
6.3.3	Fock state preparation . . . . .	54
6.3.4	Fock state dynamics . . . . .	55
6.4	Conclusion . . . . .	56
<b>7</b>	<b>Bell correlations between light and vibration</b>	<b>59</b>
7.1	Main Text . . . . .	59
7.2	Supplementary Information . . . . .	67
7.2.1	Experimental Methods . . . . .	67
7.2.2	Data Acquisition Methods . . . . .	72
7.2.3	Theoretical Methods . . . . .	73
7.2.4	Modelling of the source and detection devices . . . . .	73
7.2.5	Cross-Correlation Measurement . . . . .	75
7.2.6	The Interference Pattern for $\alpha = 0$ . . . . .	76
7.2.7	Interference Pattern for $\alpha = \pi/4$ . . . . .	78
7.2.8	CHSH Value from the Interference Patterns . . . . .	79
7.2.9	Inferring Phonon Coherence Time from the CHSH Value . . . . .	79
7.2.10	Estimating experimental parameters . . . . .	80
7.2.11	Extracting the rate of pure dephasing . . . . .	81
7.2.12	Evolution of the CHSH parameter under ideal conditions . . . . .	81
7.2.13	Evaluation of the CHSH value from finite statistics . . . . .	84
<b>8</b>	<b>Epilogue</b>	<b>87</b>
8.1	Position-momentum entanglement in Raman scattering . . . . .	88
8.2	Photon correlations away from phonon frequencies . . . . .	89
8.3	Advances for practical applications . . . . .	89
<b>9</b>	<b>Code for "Two-Color Pump-Probe Measurement of Photonic Quantum Correlations Mediated by a Single Phonon"</b>	<b>91</b>
9.1	Code for data analysis . . . . .	91
<b>10</b>	<b>Code for "Preparation and decay of a single quantum of vibration at ambient conditions"</b>	<b>95</b>
10.1	Code for data analysis . . . . .	95
10.2	Code for data acquisition . . . . .	101
<b>11</b>	<b>Jones calculus for "Bell Correlations between light and vibration"</b>	<b>107</b>
11.0.1	Jones calculus to model the experiment . . . . .	107
11.0.2	Corner density matrix . . . . .	108

11.0.3 Unbalanced initial state . . . . .	109
11.0.4 Pure initial state . . . . .	110
11.0.5 Initial state with a mixed component . . . . .	110
<b>12 Code for "Bell Correlations between light and vibration"</b>	<b>115</b>
12.1 Code for data acquisition . . . . .	115
12.2 Code for data analysis . . . . .	119
<b>13 Numerical model for "Collective Vibrational Quantum Coherence in Spontaneous Raman Scattering"</b>	<b>129</b>
<b>Bibliography</b>	<b>135</b>
<b>Bibliography</b>	<b>143</b>
<b>Curriculum Vitae</b>	<b>145</b>



# 1 Prologue

Light has always played a fundamental role in how we understand the world. When leaves absorb the red and blue present in sunlight we see their color as green. When light scatters through the atmosphere we see the sky as blue. When light is absorbed by our skin we feel the energy being transferred into our bodies as heat. Through our senses we can only directly perceive the spectrum and intensity of electromagnetic radiation, but light carries with it a lot more information. It should come as no surprise that the use of light has played a fundamental role in the development of the physical theories we use to explain the universe around us, and that those developments have in turned changed our understanding of the nature of light itself.

It has been known since time immemorial that an object emits light when it is heated, and yet it wasn't until the beginning of the last century that we had a good understanding of why. One of the key pieces of the puzzle that led to the formulation of quantum mechanics was the shape of the spectrum of light emitted by a black body. The light emitted by an object – which in an ideal scenario depends only on its temperature – was well described at low frequencies by the Rayleigh–Jeans law. At high frequencies, however, the theory predicted extremely high amounts of radiation, a problem which was termed the "Ultraviolet Catastrophe", and solving this problem required a radical departure from previous ways of thinking. In 1900, Max Plank proposed an equation that was able to reproduce the observed shape of the black body radiation, which he was later able to deduce from first principles(1; 2). His model consisted of having a collection of charged oscillators inside a cavity, and by requiring that the energy levels of the oscillators be discrete – as opposed to the continuous energy levels that would result from a typical oscillator like a mass on a spring – he was able to reproduce the observed spectrum. This insight had a tremendous significance for the development of physics, even if this fact was not immediately apparent, and earned him the 1918 Nobel Prize in Physics. Indeed, it was this fundamental change from continuous to discrete energies that kick-started the development of quantum mechanics when Einstein applied it to light in 1905 (3), and proposed the existence of the photon.

The information carried by light is not limited to its frequency and intensity. It has been well

known since the 1800s that light has some wave-like behavior, and with this knowledge came the foundation of the field of interferometry. In classical interference experiments two fields are added at the amplitude level, giving rise to interference when looking at the intensity of light (which depends on the electric field squared). The intensity interferometer (which depends on the electric field to the fourth power), was devised by Hanbury Brown and Twiss (4). Their device, which consisted of two radio-detectors, looked at the correlation between the intensities they measured as they changed their direction, and used this correlation to determine the angular spread of stellar bodies. They further studied this phenomenon in a series of table top experiments using a high pressure mercury lamp and a partially reflective mirror that separated the signal between two photo-detectors (5). The initial results were highly controversial, and attempts to reproduce them initially failed due to what was later revealed to be insufficient temporal resolution (6), but progressive experimental improvements made it clear that the effect was also taking place with visible light. Hanbury Brown and Twiss were able to demonstrate that, when both detectors were measuring photons emitted at the same time, they were twice as likely to detect fluctuations together as when they were measuring photons emitted at different times. These experimental observation lead to the formulation of a comprehensive theory of quantum optics (7; 8; 9), for which Roy Glauber received half of the 2005 nobel prize in physics. The experimental work described in this thesis relies heavily on the measurement of photon correlations, and they will be described in greater detail in Chapter 2.

So far we have only talked about the properties of light that is being emitted by an object, but there is also a lot to be learned from what happens to light when it interacts with matter. Raman spectroscopy is one of the most widely used forms of spectroscopy, and provides information about the ways in which molecules and crystals vibrate. Named after C.V. Raman, who was first able to experimentally demonstrate the technique in 1928 (10), the technique requires shining intense monochromatic light (at the visible or near infra-red wavelengths) on a sample, and uses the difference in wavelength between the incident and scattered radiation to determine the characteristic vibrational frequencies of the material.

Charged particles interact with a varying electromagnetic field according to the laws of electrodynamics. This allows the electrons in a material to interact with an incident light field, and the electrons can in turn interact with the underlying nuclei, providing a mechanism for light to couple to movements in the underlying molecule or crystal lattice. The quantum nature of atomic vibrations means that energy can only be exchanged by integer multiples of the energy of the vibrational quanta ("phonons"). This gives rise to two different types of Raman scattering: Stokes scattering, where an incident photon creates a quantum of vibration – losing its energy in the proces – and anti-Stokes scattering, where an incident phonon annihilates a quantum of vibration – gaining its energy in the process.

It is now quite natural to ask: What happens to the correlations in the optical fields during Raman Scattering?

---

The question was first theoretically addressed in 1977, when it was found that under certain conditions Raman scattering from a laser pulse should result in the correlated emission of Stokes and anti-Stokes scattered photons (11). It was only in the last decade that this question was explored experimentally, where non-classical correlations were demonstrated using solids (12) and molecular liquids (13). These experiments provide a snapshot of what occurs when the creation and annihilation of a phonon can occur within the same laser pulse, but looking at it's temporal evolution requires a second laser pulse in order to introduce a pump-probe measurement scheme. Researchers trying to develop quantum memories implemented such a scheme, using the polarization of light to distinguish the signals coming from the first and second laser pulses (14). With this they were able to demonstrate the storage of a photon inside diamond (15; 16; 17) and hydrogen (18) vibrational memories, as well the possibility to change their wavelength during the readout process (19; 20).

We now take our previous question a step further and asks: Can we use the correlations in the Raman-scattered light fields to study and manipulate the state of the underlying vibration?

We answer this question in the affirmative. This thesis explores how Raman scattering can be combined with Time Correlated Single Photon Counting in order to look at the correlations in the light fields scattered by crystals and molecules at room temperature. It uses the correlations to obtain knowledge about the quantum state and behavior of the underlying vibration. Additionally, it shows how to exploit the measurement process in order to control and manipulate the state into which the vibration is prepared.

We start by presenting a brief introduction to the theory behind photon statistics and photon correlations in Chapter 2, followed by a brief description of the way light interacts with vibrations, presented in Chapter 3.

Chapter 4 shows how to extend the methods developed for quantum memories to make them more widely applicable. The experimental protocols developed for quantum memories, as discussed above, require the samples to have specific polarization-dependent selection rules in their Raman cross-section. By using two laser frequencies, we encode information in the frequency domain instead of polarisation, circumventing this restriction. This gives us the ability to measure photon-phonon correlations in a much broader range of samples.

When Stokes scattering takes place in a liquid, the interaction gives rise to a phonon existing in a state of superposition involving all the molecules in the interaction volume. In Ch. 5 we use our newly developed technique to measure carbon disulfide ( $\text{CS}_2$ ) in its liquid form, and provide a striking demonstration of this phenomenon. There are two dominant isotopes present in our sample,  $\text{CS}_2^{32}$  and  $\text{CS}_2^{32}\text{S}^{34}$ , that have a symmetric stretch mode separated by  $8.6 \text{ cm}^{-1}$  (258 GHz). By using laser pulses that – due to the uncertainty relation between time and energy – do not provide enough spectral information to distinguish them, we are able to create a phonon that exists in a superposition shared by the two isotopes. The beating between the two isotopes oscillating at different frequencies then translates into a beating in the photon correlation measurement.

## Chapter 1. Prologue

---

We follow this by taking a closer look at the photon statistics of the scattered signals in Chapter 6, and use them to obtain information about the underlying vibrational state. We use diamond for this demonstration, and show that we can take a vibrational mode that exists initially in a thermal state, and prepare it in the  $n=1$  Fock state, which is intrinsically quantum mechanical.

We continue building towards more complex quantum states in Chapter 7. In this chapter, we show how to take advantage of the strong correlations present in the Raman-scattered fields in order to prepare an entangled state. We present a scheme that uses the erasure of temporal information in order to create a phonon in a temporal superposition, and use this to produce an entangled state where the correlations are strong enough to violate a Bell inequality.

We finish by exploring future potential research directions in Chapter 8



## 2 Photon correlations in quantum optics

In this chapter we briefly cover the theoretical foundations of photon correlations, emphasizing the tools which are required to understand and model the experiments of Sections 4 - 7.

We start by recalling the solution to the quantum harmonic oscillator (21). For a one-dimensional oscillator of mass  $m$ , and angular frequency  $\omega$ , the Hamiltonian of the system is

$$\hat{H} = \frac{\hat{p}^2}{2m} + \frac{1}{2}m\omega^2 \hat{x}^2 \quad (2.1)$$

where  $\hat{x}$  and  $\hat{p}$  are the position and momentum operators, respectively. The Hamiltonian can be rewritten in terms of the creation and annihilation operators

$$\begin{aligned} \hat{a} &= \sqrt{\frac{m\omega}{2\hbar}} \left( \hat{x} + \frac{i}{m\omega} \hat{p} \right) \\ \hat{a}^\dagger &= \sqrt{\frac{m\omega}{2\hbar}} \left( \hat{x} - \frac{i}{m\omega} \hat{p} \right) \end{aligned} \quad (2.2)$$

The Hamiltonian then becomes

$$H = \hbar\omega \left( \hat{a}^\dagger \hat{a} + \frac{1}{2} \right) \quad (2.3)$$

with energy levels  $E_n = \hbar\omega \left( n + \frac{1}{2} \right)$

The second quantization approach uses these operators to quantize the electromagnetic field, and expresses them in the Fock representation (also known as the number representation) (22).

The creation and annihilation operators acting on a state written in the Fock basis act as

$$\begin{aligned} \hat{a}^\dagger |n\rangle &= \sqrt{n+1} |n+1\rangle \\ \hat{a} |n+1\rangle &= \sqrt{n+1} |n\rangle \end{aligned} \quad (2.4)$$

From the definitions in Eq. 2.4 it is clear that the photon number operator (or more generally the bosonic number operator) is obtained by combining the operators as

$$\hat{n}|n\rangle = \hat{a}^\dagger \hat{a}|n\rangle = n|n\rangle \quad (2.5)$$

Throughout this work we will be constantly dealing with experiments that involve multiple independent bosonic modes, so it is worth explicitly stating that

$$[\hat{a}_k, \hat{a}_l^\dagger] = \hat{a}_k \hat{a}_l^\dagger - \hat{a}_l^\dagger \hat{a}_k = \delta_{kl} \quad (2.6)$$

i.e. the creation and annihilation operators do not commute unless they are describing different modes. Additionally, for the number operator the commutation relationships are

$$\begin{aligned} [\hat{a}, \hat{n}] &= \hat{a} \\ [\hat{a}^\dagger, \hat{n}] &= -\hat{a}^\dagger \end{aligned} \quad (2.7)$$

The non-commutativity of the ladder operators with the photon number operator plays an important role in the description of coherent states, as will be explained in Sec. 2.2.1.

### 2.1 Second Order Correlation Function

As mentioned in Ch. 1, the intensity interferometer was first developed by Hanbury Brown and Twiss in 1954 in order to measure the angular spread of stellar bodies (4), and later adapted for use in optics (5). It consists of two photodetectors, which in modern experiments are typically avalanche photodiodes or superconducting nanowire single-photon detectors, and an electronic mean to find the correlation between the signals. The two detectors can be used to look at different optical fields (measuring the second order cross-correlation function), or a single field (measuring the second order auto-correlation function), in which case the detectors are placed at the outputs of a beamsplitter.

The second order correlation function for two optical fields described by  $\hat{a}_1$  and  $\hat{a}_2$  is defined as

$$g_{a_1, a_2}^{(2)}(\tau) = \frac{\langle \hat{a}_1^\dagger(t) \hat{a}_2^\dagger(t+\tau) \hat{a}_2(t+\tau) \hat{a}_1(t) \rangle}{\langle \hat{a}_1(t)^\dagger \hat{a}_1(t) \rangle \langle \hat{a}_2^\dagger(t+\tau) \hat{a}_2(t+\tau) \rangle} \quad (2.8)$$

#### Measurements under realistic detection conditions

One of the properties that makes the second order correlation function so useful as an experimental measure is its insensitivity to losses (23). This only holds, however, in the absence of detection and experimental noise. In order to account for the presence of dark counts, which are unavoidable when considering a real experiment, we must introduce realistic detection

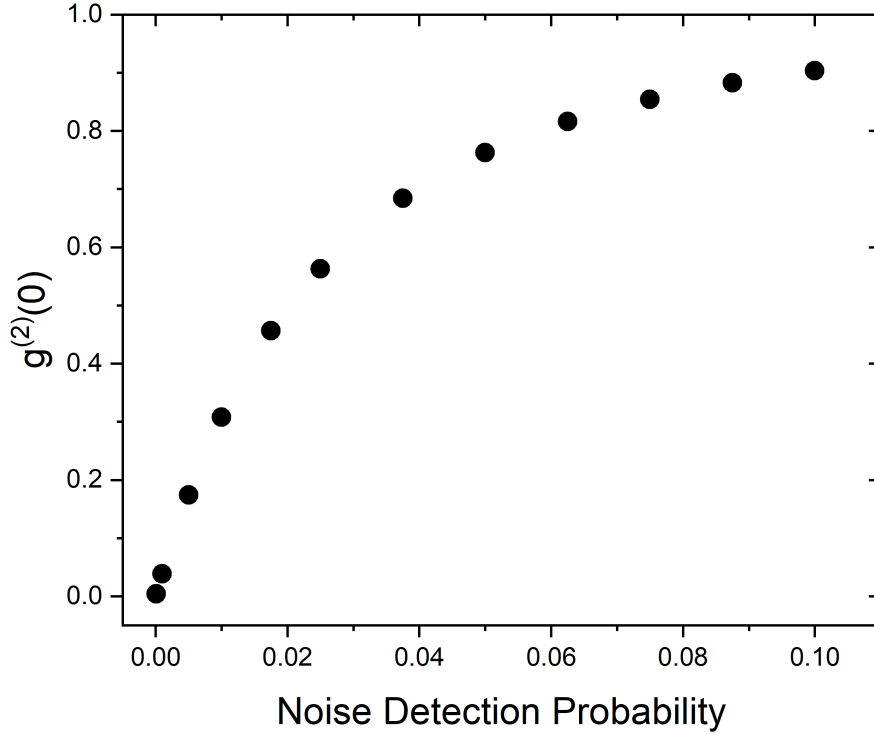


Figure 2.1: Value of the second order correlation function  $g^{(2)}(0)$  as a function of the probability of detecting a noise 'click'. The results shown were obtained for the state  $|\psi\rangle = |1\rangle$ , with a detection efficiency  $\eta = 0.1$ .

operators, as developed in (24)

$$\hat{D} = 1 - (1 - p^{dc})(1 - \eta)^{\hat{a}^\dagger \hat{a}} \quad (2.9)$$

where  $\eta$  is the detection efficiency, and  $p^{dc}$  is the dark count rate.

We show the effect of detector imperfections in Fig. 2.1, where we model a measurement of the  $n=1$  Fock state to illustrate how visibility is reduced as the dark count rate increases, and it is effectively lost when  $p^{dc}$  becomes comparable with the detection efficiency.

### 2.1.1 Non-Classical Values for the Second Order Correlation Function

The quantum-mechanical description of the second order coherence allows it to take any non-negative value. In contrast, some values of  $g_{a_1, a_2}^{(2)}(\tau)$  are incompatible with a classical description of light. We go through the three most common criteria for non-classicality in the following sections.

### Cauchy-Schwarz Inequality

For two vectors  $\vec{x}$  and  $\vec{y}$ , the Cauchy-Schwarz inequality states that  $\|\vec{x} \cdot \vec{y}\|^2 \leq \|\vec{x}\| \|\vec{y}\|$ . When dealing with a classical field,  $g^{(2)}$  is expressed in terms of intensities, and the inequality is directly applicable. This is not the case when working with operators, and as a consequence we have the inequality

$$g_{a_1, a_2}^{(2)}(0) \leq \sqrt{g_{a_1, a_1}^{(2)}(0) g_{a_2, a_2}^{(2)}(0)} \quad (2.10)$$

and a violation indicates non-classical behavior (25).

### Sub-Poissonian Statistics

A light field has sub-Poissonian statistics when its variance  $\Delta n^2 < \langle n \rangle$ . In terms of the second order correlation function, it simply means that  $g_{a_1, a_2}^{(2)}(0) < 1$ .

### Photon Anti-Bunching

Photon anti-bunching is defined as  $g_{a_1, a_2}^{(2)}(0) < g_{a_1, a_2}^{(2)}(\tau)$ , which indicates that the photon field becomes more correlated after a certain time  $\tau$ . This phenomena does not have a classical or semi-classical explanation (26). It was first demonstrated by measuring the light emitted by a single atom excited by resonant fluorescence (27), which provided the first direct evidence for quantum energy jumps.

## 2.2 Examples of Photon States and their Statistics

In this section we show different photon states that will be of interest when interpreting the experimental results shown in this thesis. We summarize the differences in their photon statistics in Fig. 2.2, which shows the probability of having a certain number of photons for a state with mean photon number  $\langle n \rangle = 1$ .

### 2.2.1 Coherent States

Coherent states are the eigenstates of the annihilation operator  $\hat{a}$ . They are defined as

$$|\alpha\rangle = \exp\left(-\frac{1}{2} |\alpha|^2\right) \sum_{n=0}^{\infty} \frac{\alpha^n}{\sqrt{n!}} |n\rangle \quad (2.11)$$

They are also the states where the product of their quadratures have minimal uncertainty, which makes a qualitative link with the definition used in classical optics.

When computing the second order cross correlation function using Eq. 2.8, their position as eigenstates of  $\hat{a}$  means that we can factor the numerator into  $\langle \hat{a}(t)^\dagger \hat{a}(t) \rangle \langle \hat{a}^\dagger(t+\tau) \hat{a}(t+\tau) \rangle$ ,

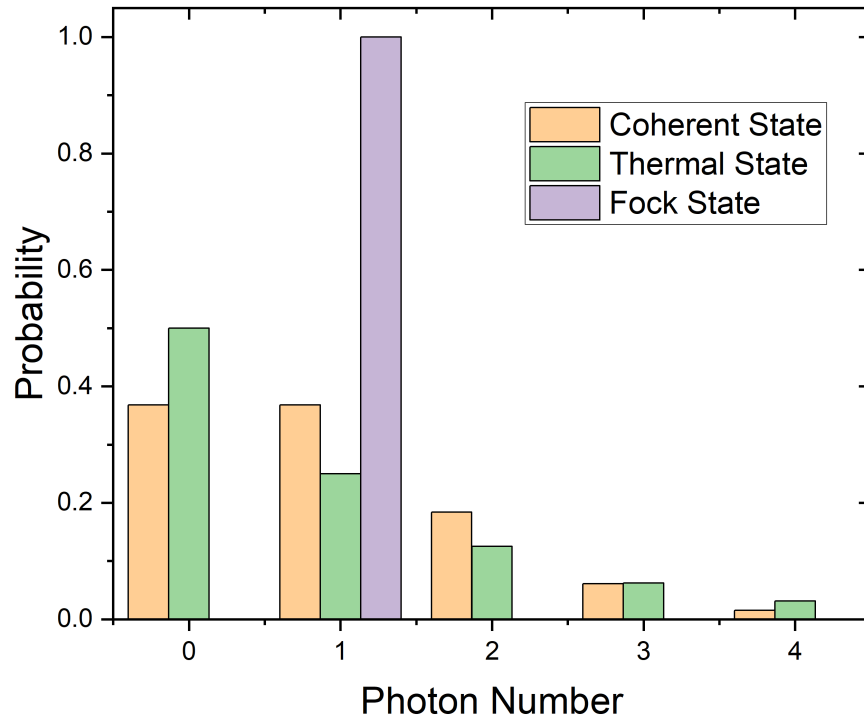


Figure 2.2: Probability distribution of the number of photons for a coherent, thermal, and for the  $n=1$  Fock state. The three states have an average photon occupancy of  $\langle n \rangle = 1$ , but have very different probabilities of observing the vacuum or multi-photon states.

and will therefore always have

$$g_{\alpha}^{(2)} = 1 \quad (2.12)$$

### 2.2.2 Thermal States

A thermal state maximizes the entropy of a system at a constant average energy. The probability of finding a certain number of photons is determined by a Bose-Einstein distribution

$$P_n = \frac{1}{Z} \exp(-\beta E_n) \quad (2.13)$$

where  $\beta = \frac{1}{k_B T}$  (with  $k_B$  the Boltzmann constant and  $T$  the temperature), and

$$Z = \frac{1}{1 - \exp(-\beta E_n)} \quad (2.14)$$

is the partition function.

The density matrix representing the state is then

$$\hat{\rho} = \sum_{n=0}^{\infty} P_n |n\rangle \langle n| \quad (2.15)$$

and has an average photon number

$$\langle \hat{n} \rangle = \text{Tr}(\hat{n} \hat{\rho}) = \frac{1}{\exp(\beta \hbar \omega) - 1} \quad (2.16)$$

We can therefore rewrite the state in terms of the average photon number as

$$\hat{\rho} = \frac{1}{1 + \langle n \rangle} \sum_{m=0}^{\infty} \left( \frac{\langle n \rangle}{1 + \langle n \rangle} \right)^m |m\rangle \langle m| \quad (2.17)$$

With this definition we can calculate the second order correlation function, and obtain  $g^{(2)}(0) = 2$ , which is independent of the temperature of the mode.

### 2.2.3 Fock States

For a Fock state  $|n\rangle$ , a direct calculation yields

$$g^{(2)}(0) = \frac{\langle \hat{N}(\hat{N} - 1) \rangle}{\langle \hat{N} \rangle^2} = \frac{n(n-1)}{n^2} = 1 - \frac{1}{n} \quad (2.18)$$

A measurement of  $g^{(2)}(0)$  can therefore be used to discriminate between the presence of one

and two photons, making it extremely useful when studying a field in an unknown quantum state, as will be used in Ch. 6. This property is also regularly used in the field of quantum emitters, where it can be used to guarantee the presence on an individual photon source.

## 2.3 Two-Mode Squeezed States

The two-mode squeezed state plays a key role in the quantum state preparation of all the experiments described in this thesis. For that reason, this section goes in detail into the mathematical description of the generation and properties of this type of state.

Squeezed states are obtained experimentally through the interaction of an optical field with a non-linear optical medium, such as a beta barium borate (BBO) crystal. This interaction can be used to reduce the uncertainty of one of the quadratures, which are analogous to the position and momentum operators we used for a harmonic oscillator, at the cost of increasing it in the other. This make it a very useful tool in metrology, where a measurement can be done that only uses the quadrature with reduced uncertainty. Squeezed states can also be used to generate single photon states, which play a key role in quantum cryptography. Here, we will focus only on the relation between squeezed states and their photon number.

Squeezed states are most typically generated by Spontaneous Parametric Down Conversion (SPDC), a three wave interaction where a pump photon is 'split' into two photons of lower energy, called 'signal' and 'idler', through the interaction with a non-linear crystal. The process can only create perfectly correlated pairs of photons, as required by energy conservation, and the properties of the 'signal' and 'idler' photons are determined by the conservation of energy and momentum in the process.

In order to simplify the calculations we consider a strong pump beam, which lets us approximate it's description by a classical (complex) amplitude  $\alpha_0$  instead of treating it quantum mechanically. The 'signal' and 'idler' modes are described by the annihilation operators  $\hat{a}_1$ ,  $\hat{a}_2$ , and they start in the vacuum state  $|\psi\rangle = |0\rangle_1 \otimes |0\rangle_2 \equiv |00\rangle$ . The interaction takes place according to the Hamiltonian

$$H_I = i\hbar g_0 \alpha_0 \left( \hat{a}_1^\dagger \hat{a}_2^\dagger - \hat{a}_1 \hat{a}_2 \right) \quad (2.19)$$

where  $g_0$  is the coupling strength governing the squeezing interaction. In Sec. 3.2, once we have gone through the basics of Spontaneous Raman Scattering, we will show the link between the Stokes interaction and the squeezing interaction Hamiltonian.

The evolution of the quantum state is described by the Schrödinger equation, and its unitary time evolution is

$$|\psi(t)\rangle = \exp \left( g_0 \alpha_0 t \left( \hat{a}_1^\dagger \hat{a}_2^\dagger - \hat{a}_1 \hat{a}_2 \right) \right) |00\rangle \quad (2.20)$$

In order to solve this equation we use the disentangling theorem for the  $SU(1,1)$  group in Lie

algebra in order to obtain (28)

$$\begin{aligned} \exp\left(g_0\alpha_0 t\left(\hat{a}_1^\dagger\hat{a}_2^\dagger - \hat{a}_1\hat{a}_2\right)\right) = \\ \exp\left(\tanh(\theta)\hat{a}_1^\dagger\hat{a}_2^\dagger\right)\exp\left(\ln(\cosh(\theta))(\hat{a}_1^\dagger\hat{a}_1 + \hat{a}_2^\dagger\hat{a}_2 - 1)\right)\exp\left(\tanh(\theta)\hat{a}_1\hat{a}_2\right) \end{aligned} \quad (2.21)$$

where  $\theta = g_0\alpha_0 t$ . Before applying Eq. 2.21 we simplify the problem by observing that for the third exponential only the zeroth order term of the expansion will give a non-zero result. Further, for the second to last exponential term the number operators will yield zero. We can now evaluate the expression by expanding the first exponential, leading to

$$\begin{aligned} |\psi(t)\rangle &= \frac{1}{\cosh(\theta)} \exp\left(\tanh(\theta)\hat{a}_1^\dagger\hat{a}_2^\dagger\right)|00\rangle \\ &= \frac{1}{\cosh(\theta)} \sum_{n=0}^{\infty} \tanh^n(\theta)|n, n\rangle \end{aligned} \quad (2.22)$$

We finally make the change  $p \equiv \tanh\theta$  to arrive at the common expression

$$|\psi(t)\rangle = \sqrt{1-p} \sum_{n=0}^{\infty} p^n |n, n\rangle \quad (2.23)$$

From Eq. 2.23 we can see that the probability of finding a particular state  $|n, n\rangle$  will be given by  $P(n, n) = p^n(1-p)$ , and  $p$  will be the probability of finding one or more photons.

There are three different cases where the photon statistics will be relevant for this work, and which we explore in the following subsections. The first case involves the measurement of the cross-correlation between the two optical fields. The second involves the auto-correlation of one of the optical fields, conditional on having detected at least one photon in the other. The third involves the auto-correlation of one of the given fields, measured in isolation.

### 2.3.1 Cross-Correlation Function of a Two-Mode Squeezed State

We start by considering the second order cross correlation between the two fields of the two-mode squeezed state. A direct calculation gives

$$\begin{aligned} \langle \hat{N}_1 \rangle &= \langle \hat{N}_2 \rangle = (1-p) \sum_{n=0}^{\infty} np^n = \frac{p}{1-p} \\ \langle \hat{N}_1 \hat{N}_2 \rangle &= (1-p) \sum_{n=0}^{\infty} n^2 p^n = \frac{p(p+1)}{(1-p)^2} \\ g_{1,2}^{(2)}(0) &= \frac{\langle \hat{N}_1 \hat{N}_2 \rangle}{\langle \hat{N}_1 \rangle \langle \hat{N}_2 \rangle} = 1 + \frac{1}{p} \end{aligned} \quad (2.24)$$

where  $|p| < 1$  is a requirement for the convergence of the series. From Eq. 2.24 we can see that as  $p$  tends to zero  $g_{1,2}^{(2)}$  tends towards infinity, while a larger  $p$  decreases the value of  $g_{1,2}^{(2)}$ . This result shows that the value of  $g_{1,2}^{(2)}$  can increase dramatically when measuring a two-mode



squeezed state prepared with low probability  $p$ , which will play a key role in the experiment shown in Ch. 4. The strength of the correlations also plays a role as a quantum resource, as will be explained in Ch. 7.

### 2.3.2 Conditional Auto-Correlation Function in a Two-Mode Squeezed State

We now consider another experimentally relevant scenario by examining the second order auto correlation function of one of the optical modes, conditional on the detection of one or more photons in the other mode. In order to do this we first calculate the density matrix  $\hat{\rho} = |\psi\rangle\langle\psi|$  which corresponds to the state in Eq. 2.23. We then define an operator  $\hat{D}_2(m) = |0\rangle_2\langle m|$  for  $m \geq 1$ , which operates on the second subsystem, and corresponds to the detection of  $m$  photons before returning it to the vacuum state. We now calculate the density matrix conditional on this measurement, i.e.

$$\hat{\rho}_1^{cond} = \frac{\hat{D}_2 \hat{\rho} \hat{D}_2^\dagger}{\text{Tr}(\hat{D}_2 \hat{\rho} \hat{D}_2^\dagger)} = \frac{1-p}{p} \sum_{m \geq 1} p^m |m\rangle\langle m| \quad (2.25)$$

We can then calculate the second order auto correlation function, and find that

$$g_{cond}^{(2)}(0) = \frac{\langle \hat{N}(\hat{N}-1) \rangle}{\langle \hat{N} \rangle^2} = 2p \quad (2.26)$$

From Eq. 2.25 we can see that after a photon is detected in one of the modes, the other mode of the two-mode squeezed state closely resembles the  $n=1$  Fock state, and that this approximation improves when preparing the state with a lower probability  $p$ . This is also reflected in the autocorrelation function of the mode, which tends towards zero for  $p \ll 1$ , approaching those of the  $n=1$  Fock state discussed in Sec. 2.2.3. This result will play a key role in Ch. 6.

### 2.3.3 Independent Auto-Correlation Functions of Two-Mode Squeezed State

Finally, we look at what happens when the statistics of each photon field are observed in isolation. We start by taking the density matrix of the two-mode squeezed state and calculate the trace with respect to the second subsystem,

$$\begin{aligned} \hat{\rho}_1 &= \text{Tr}_2(\hat{\rho}) = \sum_{m=0}^{\infty} \langle m|_2 \hat{\rho} |m\rangle_2 \\ &= (1-p) \sum_{n=0}^{\infty} p^n |n\rangle\langle n| \end{aligned} \quad (2.27)$$

We can now calculate the second order correlation function, and find that  $g^{(2)} = 2$ , which does not depend on  $p$ . In contrast with Sec. 2.3.2, we see that the correlations in each mode – when taken independently – exhibit thermal statistics. This shows that there are key properties that

can only be measured through the correlation between the two fields, and will play a key role in the experiment shown in Sec. 6.

### 2.4 Correlations due to entanglement

In this section we consider a different type of photon correlation. So far we have only covered correlations between the number of photons, either between two light fields or within a single one. Here we will consider the correlations between two fields, each one containing a single excitation, and each having a degree of freedom with two states. For this, we include the polarization of light, where the vertical and horizontal polarization basis is defined as

$$|H\rangle = \begin{bmatrix} 1 \\ 0 \end{bmatrix} \quad |V\rangle = \begin{bmatrix} 0 \\ 1 \end{bmatrix} \quad (2.28)$$

where the number of photons is not explicitly included, as it is fixed at one.

In quantum mechanics, a multipartite state is said to be entangled if it cannot be expressed as a product of its sub-states. To illustrate this, let's consider a quantum state  $|\psi'\rangle$  that is the product of two arbitrary photon states, i.e.  $|\psi'\rangle = (a|H\rangle + b|V\rangle) \otimes (c|H\rangle + d|V\rangle) = ac|HH\rangle + ad|HV\rangle + bc|VH\rangle + bd|VV\rangle$ , where  $a, b, c, d \in \mathbb{C}$ , and  $a^*a + b^*b = 1$ ,  $c^*c + d^*d = 1$ . From the previous computation it is clear that no choice of coefficients can produce a state of the form  $|\phi^+\rangle = \frac{1}{\sqrt{2}}(|HH\rangle + |VV\rangle)$ . Interestingly, such a state has the property that the measurement of one of the subsystems will yield the outcomes  $|H\rangle$  or  $|V\rangle$  with 50-50 probability, but the measurement of both two sub-systems will always be perfectly correlated.

The perfect correlation between measurements performed on the two sub-systems of  $|\phi^+\rangle$  still holds after transforming the state into a different measurement basis. In a circular polarization basis, defined by

$$|R\rangle = \frac{1}{\sqrt{2}} \begin{bmatrix} 1 \\ i \end{bmatrix} \quad |L\rangle = \frac{1}{\sqrt{2}} \begin{bmatrix} 1 \\ -i \end{bmatrix} \quad (2.29)$$

the state becomes  $|\phi^+\rangle = \frac{1}{\sqrt{2}}(|RR\rangle + |LL\rangle)$ , which has the exact same properties. Indeed, the two photons will always be perfectly correlated when measured in the same basis, a property which is known as rotational invariance.

This leads to an apparent paradox, where the measurement of one of the subsystems 'forces' the other to collapse into a particular state, but this action does not appear to be bound by the speed of light. This paradox was described by Einstein, Podolsky, and Rosen in 1935, and used as an argument against the completeness of the theory of quantum mechanics (29). Bell's theorem offered a way to test this paradox experimentally, with the subsequent demonstrations showing that the predictions made by quantum mechanics are correct (30; 31; 32; 33).

Any state that cannot be decomposed into its sub-systems without loss of information is

consider entangled. There are, however, different degrees of entanglement, and states capable of violating a Bell-type inequality belong to the highest position in that hierarchy(34). It is this type of state which will be the subject of chapter 7.



## 3 Interaction between light and vibration

In this chapter we give a short summary of the way in which light interacts with an atomic vibration through the Raman effect. The goal of the chapter is not to provide an exhaustive description, but only to highlight the aspects required to make the link between an atomic vibration and the quantum optics formalism used when discussing our experiments. We are particularly interested in the way that the Raman interaction affects the photon and phonon numbers, and how this is reflected in a measurement of their second order correlation function.

### 3.1 The Raman Effect

When a light field is scattered by matter, the process may be elastic – where the outgoing radiation has the same energy as the incoming one – or inelastic, where there is a change in energy in the scattered radiation. Raman scattering, in which a light field exchanges energy with the vibrational degrees of freedom of a molecule or crystal, is the dominant inelastic effect at optical frequencies.

Light does not couple directly to the nuclear motion of atoms. Instead, it couples to the electric dipole of the electrons, which in turn may interact with the lattice vibrations. This provides a mechanism for light to interact with the vibrational degree of freedom of the material, which in the quantum picture means that it can create or annihilate discrete units of vibrational energy, called phonons. The frequency of the phonons depends on the molecule or crystal lattice involved, and this technique therefore provides a "fingerprint" of the sample under study.

Energy conservation requires that during the Stokes interaction – when a quantum of vibration is created – the photon driving the interaction will lose the energy imparted to the phonon mode, becoming red-shifted as a result. Conversely, during the anti-Stokes process – when a quantum of vibration is annihilated – the photon driving the interaction absorbs the energy from the phonon mode, and becomes blue shifted as a result. Due to the virtual nature of the

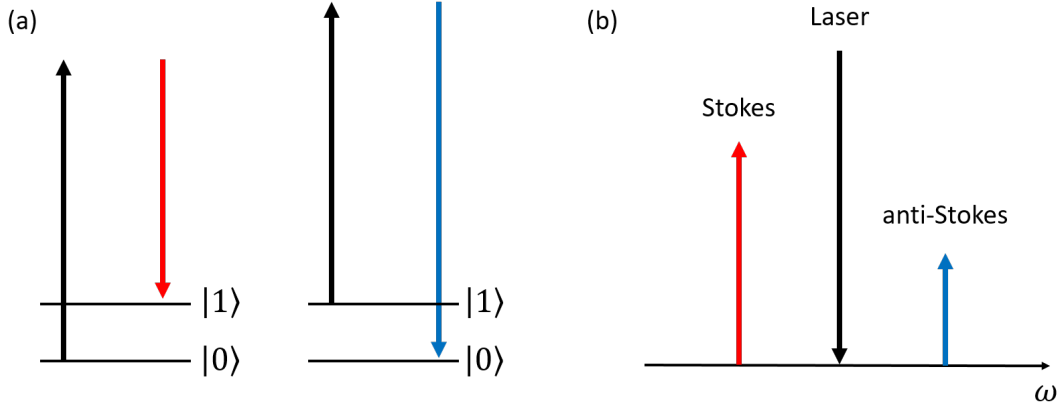


Figure 3.1: Schematic illustration of the Raman effect. **(a)** An incoming laser (black arrows) interacts with matter, it has a chance of creating (left) or annihilating (right) a quantum of vibration. **(b)** The change in energy during the Raman interaction leads to the emergence of two sidebands, separated from the incoming laser by the characteristic phonon frequency of the material. The asymmetry between the two sidebands reflects the low probability of finding a quantum of vibration at room temperature for the systems studied in this thesis.

interaction, the creation of a scattered photon and creation/annihilation of a phonon are also correlated in time.

### 3.2 Stokes and anti-Stokes interaction

To illustrate the relation between the Raman interaction and the squeezing interaction discussed in Ch. 2, we follow a similar analysis to that outlined in (35). We consider a simple example where a plane wave, propagating along  $x$  and polarized among  $z$ , interacts with a linear chain of atoms arranged along  $x$ , and whose displacement is described by  $u(x, t)$ .

The polarizability of the chain is defined in terms of its electric susceptibility  $\chi(u(x, t))$  as

$$P(x, t) = \epsilon_0 \chi(u(x, t)) E(x, t) = \epsilon_0 E(x, t) [\chi_0 + \chi_R u(x, t) + \mathcal{O}(u(x, t)^2)] \quad (3.1)$$

where the first order expansion of the electric susceptibility gives the Raman tensor, and we neglect the higher order terms. The electric displacement in the crystal is then

$$D(x, t) = \epsilon_0 E(x, t) + P(x, t) = (1 + \chi_0) \epsilon_0 E(x, t) + \epsilon_0 E(x, t) \chi_R u(x, t) \quad (3.2)$$

The energy density of the system is

$$\begin{aligned} H_{Tot} &= \frac{1}{2}D(x, t)E(x, t) + \frac{1}{2}B(x, t)B(x, t) \\ &= \frac{1}{2}(1 + \chi_0)\epsilon_0 E(x, t)E(x, t) + \frac{1}{2}B(x, t)B(x, t) + \frac{1}{2}\chi_R\epsilon_0 E(x, t)E(x, t)u(x, t) \end{aligned} \quad (3.3)$$

where we can separate the total Hamiltonian into a free and an interacting component such that  $H_{Tot} = H_{free} + H_I$ , where

$$\begin{aligned} H_{free} &= \frac{1}{2}(1 + \chi_0)\epsilon_0 E(x, t)E(x, t) + \frac{1}{2}B(x, t)B(x, t) \\ H_I &= \frac{1}{2}(\chi_R)\epsilon_0 E(x, t)E(x, t)u(x, t) \end{aligned} \quad (3.4)$$

We now separate the electric field into  $E(x, t) = E_L(x, t) + E'(x, t)$ , where  $E_L(x, t)$  is the monochromatic wave being sent into the system, and  $E'(x, t)$  represents everything else. The interaction Hamiltonian now becomes

$$H_I = \frac{1}{2}\epsilon_0\chi_R E_L^2(x, t)u(x, t) + \epsilon_0\chi_R E_L(x, t)E'(x, t)u(x, t) + \frac{1}{2}\epsilon_0\chi_R E'^2(x, t)u(x, t) \quad (3.5)$$

In Eq. 3.5 the first term on the right hand side corresponds to a shift in the zero point energy of the vibration, but has no further physical consequences for the interaction. For the components of the electric field  $E_L(x, t) \gg E'(x, t)$ , which means that the second term will play a much larger role than the third one, so we can further simplify the interaction Hamiltonian to

$$H_I = \epsilon_0\chi_R E_L(x, t)E'(x, t)u(x, t) \quad (3.6)$$

We now expand the fields in terms of complex exponentials,

$$\begin{aligned} E_L(x, t) &= \frac{E_L}{2}e^{i(k_L x - \omega_L t)} + \frac{E_L}{2}e^{-i(k_L x - \omega_L t)} = E_L^{(+)} + E_L^{(-)} \\ E'(x, t) &= \sum_p \sqrt{\frac{\hbar\omega_p}{2\epsilon_0 N_{E'}}} \left( \hat{a}_p e^{i(k_p x - \omega_p t)} + \hat{a}_p^\dagger e^{-i(k_p x - \omega_p t)} \right) = E'^{(+)} + E'^{(-)} \\ u(x, t) &= \sum_q \sqrt{\frac{\hbar}{2\omega_0 N_u}} \left( \hat{b}_q e^{i(k_q x - \omega_0 t)} + \hat{b}_q^\dagger e^{-i(k_q x - \omega_0 t)} \right) = u^{(+)} + u^{(-)} \end{aligned} \quad (3.7)$$

where we have taken  $E_L(x, t)$  to be a large classical field, while we describe  $E'(x, t)$  and  $u(x, t)$  in terms of the bosonic operators  $\hat{a}$  and  $\hat{b}$ , respectively, and the terms  $X^{(+)}$  contain the terms rotating with  $e^{-i\omega t}$ , while the terms  $X^{(-)}$  rotate with  $e^{i\omega t}$ . The constants  $N_{E'}$  and  $N_u$  are normalization factors related to the geometry being considered.

When we apply the expansion to the interaction Hamiltonian, we will have terms with  $E_L^{(+)}E'^{(+)}$  and  $E_L^{(-)}E'^{(-)}$ , which will rotate much faster than the rest. These fast oscillating terms will

### Chapter 3. Interaction between light and vibration

---

average out to zero, so we can neglect them to obtain

$$H_I = \epsilon_0 \chi_R \left( E_L^{(+)} E'^{(-)} u^{(-)} + E_L^{(-)} E'^{(+)} u^{(+)} + E_L^{(+)} E'^{(-)} u^{(+)} + E_L^{(-)} E'^{(+)} u^{(-)} \right) \quad (3.8)$$

The first and second terms on the right hand side oscillate with frequency  $\omega_S = \omega_L - \omega_0$ , corresponding to the Stokes signal, while the third and fourth terms oscillate with frequency  $\omega_A = \omega_L + \omega_0$ , corresponding to the anti-Stokes frequency. We group the terms associated with each frequency to obtain

$$H_S = \epsilon_0 \chi_R \left( E_L^{(+)} E'^{(-)} u^{(-)} + E_L^{(-)} E'^{(+)} u^{(+)} \right) \quad (3.9)$$

$$H_A = \epsilon_0 \chi_R \left( E_L^{(+)} E'^{(-)} u^{(+)} + E_L^{(-)} E'^{(+)} u^{(-)} \right) \quad (3.10)$$

The derived interaction Hamiltonian  $H_S$  has the same form as Eq. 2.19, which lets us apply the properties we derived in Sec. 2.3 to the Stokes interaction. The main difference will be that, when considering SPDC, the two modes in the squeezed state consisted of propagating optical fields. In contrast, in Stokes scattering one of the bosonic modes refers to a vibrational excitation in the sample, and is not directly available in measurements.

### 3.3 Readout through anti-Stokes Scattering

In the previous section we showed that the Stokes scattering behaves as a squeezing interaction affecting the phonon and Stokes fields. In this section we consider the anti-Stokes interaction in more detail, and show how the photon statistics of the anti-Stokes field faithfully reproduce those of the vibrational state.

In order to find the link between the correlations in the anti-Stokes field and those present in the phonon field, we start by considering the time evolution of the  $\hat{a}$  and  $\hat{b}$  operators in the Heisenberg representation. In order to simplify the notation, we group the constants present in Eq. 3.10 into  $g$ , and use  $H_A = g \hat{a} \hat{b}^\dagger + h.c.$ , and find the Heisenberg equations of motion

$$\frac{\partial \hat{a}}{\partial t} = \frac{g^*}{i\hbar} \hat{b} \quad \frac{\partial \hat{b}}{\partial t} = \frac{g}{i\hbar} \hat{a} \quad (3.11)$$

$$\frac{\partial^2 \hat{a}}{\partial t^2} = \frac{-g^* g}{\hbar^2} \hat{a} \quad \frac{\partial^2 \hat{b}}{\partial t^2} = \frac{-g^* g}{\hbar^2} \hat{b} \quad (3.12)$$

Eq. 3.12 describes a system of second-order linear differential equations, which can be solved to obtain

$$\begin{aligned} \hat{a}(t) &= \hat{a}_0 \cos(gt) + \hat{b}_0 \sin(gt) \\ \hat{b}(t) &= \hat{b}_0 \cos(gt) + \hat{a}_0 \sin(gt) \end{aligned} \quad (3.13)$$

where  $\hat{a}_0(0)$  and  $\hat{b}_0(0)$ . We can now use the temporal evolution given by Eq. 3.13 to calculate



the expectation values that are necessary for the second order correlation function of the anti-Stokes field. We assume that the anti-Stokes field starts in the vacuum state, which will make all the terms of the form  $\hat{x}\hat{a}_0|\psi\rangle = 0$ . Additionally, we recall that in the Fock basis  $\langle i||j\rangle = \delta_{i,j}$ , so all the terms that contain an unbalanced number of creation and annihilation operators will also become zero. Using this we find

$$\begin{aligned}\langle \hat{a}^\dagger(t)\hat{a}(t) \rangle &= \sin^2(gt) \langle \hat{b}_0^\dagger\hat{b}_0 \rangle \\ \langle \hat{a}^\dagger(t)\hat{a}^\dagger(t)\hat{a}(t)\hat{a}(t) \rangle &= \sin^4(gt) \langle \hat{b}_0^\dagger\hat{b}_0^\dagger\hat{b}_0\hat{b}_0 \rangle\end{aligned}\tag{3.14}$$

We combine these equations to obtain the second order correlation function

$$g_{a(t)}^{(2)} = \frac{\langle \hat{a}^\dagger(t)\hat{a}^\dagger(t)\hat{a}(t)\hat{a}(t) \rangle}{\langle \hat{a}^\dagger(t)\hat{a}(t) \rangle^2} = \frac{\langle \hat{b}_0^\dagger\hat{b}_0^\dagger\hat{b}_0\hat{b}_0 \rangle}{\langle \hat{b}_0^\dagger\hat{b}_0 \rangle^2} = g_{b_0}^{(2)}\tag{3.15}$$

This shows that, by measuring the second order correlation function of the anti-Stokes field, we are able to probe the correlations that exist in the phonon field.

Having shown that the measurement of the anti-Stokes field is also a measurement of the phonon field, we have all the tools we need in order to address the experiments shown in the following chapters.



## 4 Two-Color Pump-Probe Measurement of Photonic Quantum Correlations Mediated by a Single Phonon

Raman scattering can be used to modify and read the state of a mechanical vibration. The detection of a Stokes photon, scattered by a first laser pulse, heralds the successful preparation of the state, while the detection of an anti-Stokes photon, scattered from a second pulse, provides information about the vibration's temporal evolution. The first experiments in diamond relied on polarization in order to distinguish between the signals generated by the two laser pulses, but this greatly limits the types of samples that can be studied (14; 15).

In this chapter, we demonstrate a new experimental methodology to measure the temporal dynamics of a phonon mode without relying on the material's polarization selection rules. We use two laser pulses of different wavelength, and use the frequency information in order to distinguish the signals. We measure non-classical correlations between the Stokes and anti-Stokes fields scattered by diamond, and use them to measure a phonon lifetime of  $3.9 \pm 0.7$  ps. The purpose of this experiment is to prove the validity of the methodology, which will be the starting point for the rest of the experiments in this thesis.

I built the experiment and performed the experiments together with Dr. Mitchell Anderson, and analyzed the data. The manuscript was prepared in collaboration with all the authors.

The content of this chapter is reproduced from:

Anderson, Mitchell D.\*, **Santiago Tarrago Velez\***, Kilian Seibold, Hugo Flayac, Vincenzo Savona, Nicolas Sangouard, and Christophe Galland. "Two-color pump-probe measurement of photonic quantum correlations mediated by a single phonon." *Physical review letters* 120, no. 23 (2018): 233601.

\*Equal contribution authorship

Further information about the code used to perform the data analysis can be found in Appendix 9

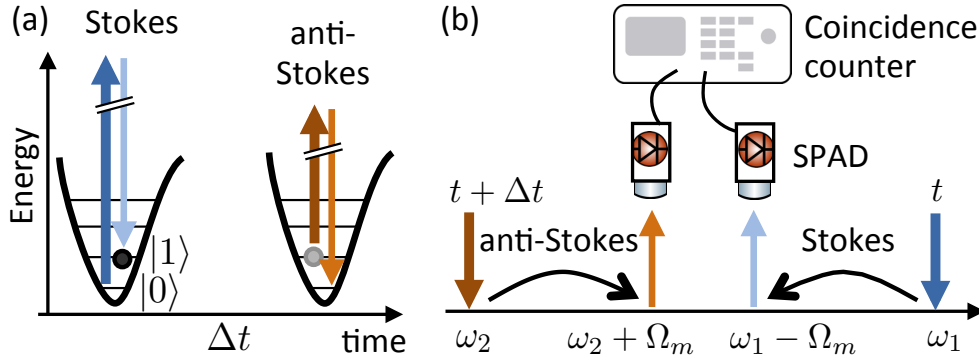


Figure 4.1: (a) Concept of the experiment: The first (write) laser pulse probabilistically prepares the phonon in state  $|n = 1\rangle$  upon detection of a Stokes photon. The second (read) pulse, after a time delay  $\Delta t$ , converts this phonon into an anti-Stokes photon. (b) Schematics of the photon counting in the frequency domain (SPAD: single-photon avalanche photodiode). The choice of  $\omega_1$  and  $\omega_2$  is completely free, as long as the Stokes and anti-Stokes photons can be efficiently isolated by spectral filtering.

## 4.1 Main Text

Phonons, the quantized excitations of internal vibrational modes in crystals and molecules, span a broad frequency range up to  $\sim 100$  THz. At these high frequencies, thermal occupancy at room temperature is much less than one, so that quantum effects are readily observable. For example, creation and annihilation of a single phonon within one short laser pulse produces non-classically correlated Stokes–anti-Stokes (SaS) photon pairs (11; 36; 37), as observed in pulsed Raman scattering from a diamond crystal (12), liquid water (13) and other molecular species (38). With the advent of quantum optomechanics, the quantisation of lower frequency (MHz to GHz) mechanical oscillations was also evidenced in several experiments using phase sensitive detection (39; 40) and photon counting (41; 42). Finally, in a series of recent experiments, Raman-active phonon modes in pure diamond (14; 15; 16; 43; 19; 17) and gaseous hydrogen (44; 18; 45) have been used to store and process classical and quantum information on picoseconds time scales at room-temperature. Developing versatile schemes and techniques to address non-classical phonon states in bulk and nanoscale systems is thus a promising research direction to improve our understanding of quantum effects occurring at ambient conditions and leverage them for quantum technologies.

In this Letter, we present a new scheme to measure the creation and annihilation of a single phonon Fock state with sub-picosecond time resolution (Fig. 4.1), which can be applied on any Raman-active high frequency mode, such as ubiquitously found in organic materials. Our scheme is conceptually similar to the one recently applied to an optomechanical cavity with a GHz mechanical oscillator (41), although we don't use any optical cavity and measure the dynamics on time scales that are 5 to 6 orders of magnitude shorter. We use diamond in a proof-of-principle experiment (phonon frequency  $\Omega_m/2\pi = 39.9$  THz), but in contrast to Refs. (14; 15; 16; 43; 19; 17; 44; 18; 45), our scheme does not rely on the polarization selection rule of

Raman scattering to temporally distinguish between photons. It is therefore not restricted to diamond and can be applied to low-dimensional structures and molecules as well, in the solid, liquid or gaseous phase. Indeed, we use two-color excitation and spectral multiplexing to distinguish the photons from the *write* and *read* steps. In the *write* step, a laser pulse centered at frequency  $\omega_1$  leads to Stokes scattering with low probability  $p_S \ll 1$  (two-phonon generation occurs with probability  $\propto p_S^2 \ll p_S$ ). Detection of a Stokes (S) photon at frequency  $\omega_1 - \Omega_m$  projects the phonon onto the Fock state  $|n = 1\rangle$ . In the *read* step, after a controllable time delay  $\Delta t$ , a second synchronised pulse centered at a different frequency  $\omega_2$  is used to probe the population of the conditional phonon Fock state by detection of an anti-Stokes (aS) photon at frequency  $\omega_2 + \Omega_m$ . The value of the second-order cross-correlation  $g_{S,aS}^{(2)}(\Delta t)$  between the S and aS photons witnesses the non-classical nature of the two-photon state produced by the exchange of a single phonon (46). The dynamics of this non-classical SaS correlation can be tracked by scanning  $\Delta t$ , revealing the single-phonon lifetime.

**Experimental Setup**—Our experimental setup is depicted in Fig. 5.2. The two synchronized femtosecond pulse trains are generated by a Ti:Sapph oscillator (Tsunami, Spectra Physics, 80 MHz repetition rate) and a frequency-doubled optical parametric oscillator (OPO-X fs, APE Berlin). We can independently tune the Ti:Sapph wavelength between 740 and 860 nm and the OPO wavelength between 505 and 740 nm. The OPO generates the write pulse, while the Ti:Sapph is sent through a delay line to provide the read pulse. The read and write pulses are combined at a dichroic mirror before being focused on a synthetic diamond crystal ( $\sim 300 \mu\text{m}$  thick) cut along the 1-0-0 crystal axis. We use tunable interference filters (highlighted in green in Fig. 5.2) to block the spectral components of the excitation pulses that overlap with the detection window. The sample is studied in transmission with a pair of objective lenses in order to fulfill momentum conservation in the exchange of the same phonon in the read and write scattering processes. After the sample, we block most of the laser light with a combination of tunable short and long pass filters, and send the signal either to a spectrometer equipped with a cooled CCD array or to a single mode fiber, which selects a single spatial mode of the photons. Since momentum is conserved during Raman scattering, this allows us to probe a well-defined phonon spatial mode in the bulk crystal. After the fiber, light is collimated and sent to a tunable dichroic mirror (TuneCube, AHF analysentechnik AG), which allows us to separate the S and aS photons, depending on their wavelengths, by rotating a tunable filter (here a long-pass). The separated signals are further spectrally filtered before impinging on fiber-coupled single photon avalanche photodiodes (SPADs) connected to a coincidence counter.

**Results**—In each experiment, we begin by tuning the Ti:Sapph and OPO to center frequencies  $\tilde{\omega}_2$  and  $\tilde{\omega}_1$  so that  $\tilde{\omega}_1 - \tilde{\omega}_2 = \Omega_m$ . When the two pulses overlap, both spatially and temporally, strong coherent anti-Stokes Raman scattering (CARS) at frequency  $\tilde{\omega}_1 + \Omega_m$  is generated. We use this signal to find the zero time delay and optimize the spatial overlap of the two excitation beams.

## Chapter 4. Two-Color Pump-Probe Measurement of Photonic Quantum Correlations Mediated by a Single Phonon

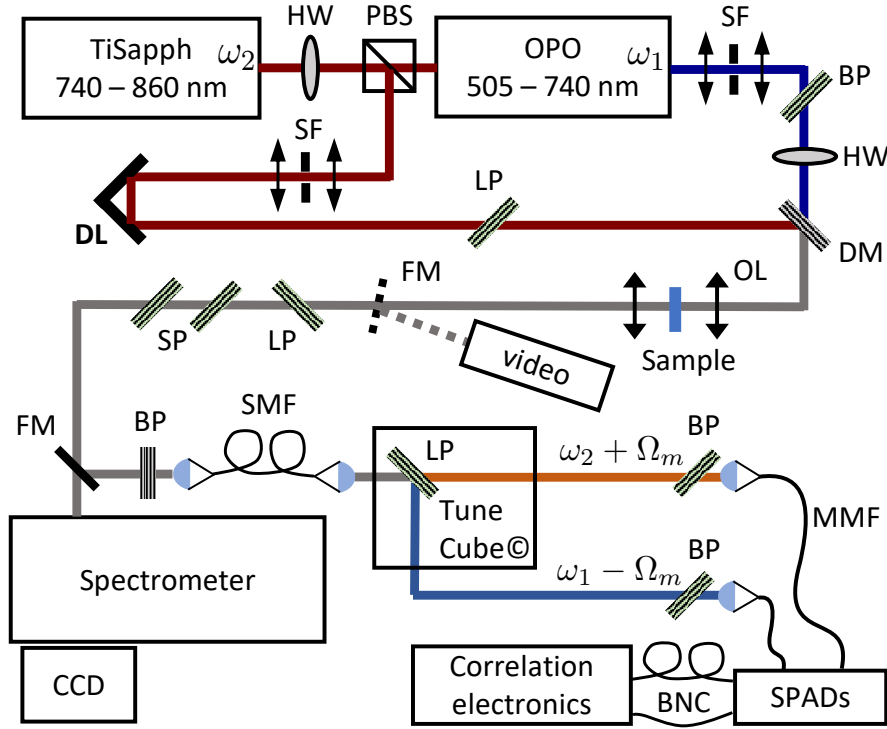


Figure 4.2: Schematic drawing of the experimental setup. HW: half-wave plate; PBS: polarizing beam-splitter; SF: spatial filter; SP/LP/BP: short/long/band-pass filters (tunable filters are highlighted in green); DL: delay line; DM: Dichroic mirror; OL: objective lens (numerical aperture = 0.8); SMF: single-mode fiber (HP780, Thorlabs); MMF: graded index multimode fiber (100  $\mu\text{m}$  core, NA 0.29, OZ Optics); FM: flip mirror. A video camera is used to overlap the beams.

The center frequency of the write pulse is then tuned so that the S and aS peaks are spectrally separated from the read and write pulses. As a first demonstration, the central wavelengths of the write and read pulses are set to 696 nm and 810 nm, respectively. This results in S photons at 767 nm (1.619 eV) and aS photons at 732 nm (1.695 eV), as seen on the Raman spectrum of Fig. 4.3a, inset. Figure 4.3a presents the coincidence histogram obtained at zero write-read delay in this configuration. The  $t = 0$  ns peak corresponds to events where one photon is detected in each channel within the same write-read pulse sequence. Since the delay between two repetitions (12.5 ns) is three to four orders of magnitude longer than the phonon lifetime, the side peaks are due to uncorrelated photons ("accidental" coincidences). The number of coincidences in the central peak, divided by the average number of coincidences in the side peaks, is a measure of  $g_{S,aS}^{(2)}(0)$ , the normalized second-order cross-correlation function between the S photons produced in the write pulse and the aS photons produced in the read pulse (41; 47).

The Cauchy-Schwartz inequality sets an upper bound on the possible value of the cross-correlation for classical fields  $g_{S,aS}^{(2)}(0) \leq \left( g_{S,S}^{(2)}(0) g_{aS,aS}^{(2)}(0) \right)^{1/2}$ , where the terms on the RHS are

the second-order auto-correlation functions of the S and aS fields (25; 48). We expect that  $g_{S,S}^{(2)}(0) = 2$  since the spontaneously emitted S photons follow the same (thermal) statistics as in parametric down-conversion below threshold. However, this is true only in the single-mode situation, as the Stokes auto-correlation function falls as  $1 + 1/N$  with  $N$  the number of phonon and photon modes. We therefore used a 50/50 beam splitting fiber to measure the auto-correlation of the S channel and found  $g_{S,S}^{(2)}(0) = 2 \pm 0.1$  (see Fig. S1), confirming that our experiment measures the state of a single phonon mode. Although the count rate on the aS detector was not sufficient to measure precisely  $g_{aS,aS}^{(2)}(0)$ , we cannot think of any reason why it should be larger than 2 since the aS photons should carry the thermal statistics of the phonon mode. In summary, the classical bound to our measurement is  $g_{S,aS}^{(2)}(0) \leq 2$ . The measured value  $g_{S,aS}^{(2)}(0) = 63.4 \pm 9.7$  in Fig. 4.3a,b thus violates the Cauchy-Schwartz inequality by 6 standard deviations and is a proof of quantum correlations between the S and aS photons, mediated by the exchange of a single phonon.

We then repeat the coincidence measurement for many different positions of the delay line and obtain the time dependent correlation function  $g_{S,aS}^{(2)}(\Delta t)$  (Fig. 4.3b). The correlations decay with a  $1/e$  time constant of  $3.9 \pm 0.7$  ps (bounds for 95% confidence), in agreement with the literature values of the optical phonon lifetime in diamond (14; 49). This demonstrates that we are able to measure the lifetime of a phonon Fock state by following the decay of non-classical S–aS correlations.

In order to understand what determines the precise value of  $g_{S,aS}^{(2)}$  and what limits the achievable degree of non-classical correlations, we study the dependence of the zero-delay correlation  $g_{S,aS}^{(2)}(0)$  on the powers in the write ( $P_w$ ) and read ( $P_r$ ) beams (Fig. 4.3c) and compare the results to an analytically soluble quantum model of parametrically coupled photon-phonon modes at zero temperature. In direct analogy with the physics of photon pairs produced by parametric down-conversion (24), we find that  $g_{S,aS}^{(2)}(0)$  decreases as  $1/n_S \propto 1/P_w$  where  $n_S$  is the average S photon number produced by the write pulse. This can be understood as the consequence of the growing probability of exciting the  $|n=2\rangle$  phonon Fock state at higher power compounded with the fact that our detectors cannot resolve the photon number.

Interestingly, at low  $P_w$  the correlation saturates at a value that depends on the power in the read pulse  $P_r$ . We can explain this behavior by the noise generated in the read pulse, which has three components. (i) The thermal phonons (thermal occupancy  $n_{th} < 2 \cdot 10^{-3}$ ) are responsible for uncorrelated aS emission. If this were the only source of noise, then  $g_{S,aS}^{(2)}(0) \rightarrow 1/n_{th}$  at low write powers  $P_w$ , irrespective of the read power  $P_r$ . (ii) Yet, another intrinsic noise source related to the Raman process is SaS pair emission in the read pulse (36), which scales quadratically with  $P_r$ . (iii) Finally, we identified spontaneous four-wave mixing as another source of uncorrelated counts on the aS detector in the read pulse.

The simplified model used to fit the data in Fig. 4.3c can also be used to compute the expected second-order auto-correlation of the aS photons  $g_{aS,aS}^{(2,cond)}(0)$  conditional on the detection of a S photon in the write pulse, as would be measured to characterize heralded single-photons

## Chapter 4. Two-Color Pump-Probe Measurement of Photonic Quantum Correlations Mediated by a Single Phonon

---

(47). We find values of  $g_{aS,aS}^{(2,cond)}(0)$  well below 0.1 for the parameters corresponding to most data points of Fig. 4.3c, demonstrating that our experiment indeed probes the dynamics of the  $|n = 1\rangle$  phonon Fock state, with negligible contribution of  $n \geq 2$  eigenstates.

A route to increase the measured quantum correlation toward the  $1/n_{th}$  thermal limit is the use of a cavity in the resolved sideband regime to select only S and aS processes in the write and read pulses, respectively (47). This is where the broad tunability of our setup would become particularly relevant.

Indeed, we show in Fig. 4.4 that we can perform this measurement using different configurations of the excitation/detection wavelengths accessible with our instruments. For example, the write and read pulses were also set at 650 nm and 821 nm, respectively, yielding S and aS photons at 712 nm (1.74 eV) and 740 nm (1.67 eV) (see Fig. 4.4, inset). Although the absolute value of  $g_{S,aS}^{(2)}(0)$  depends on the laser powers, on the quality of alignment and beams' overlap, on the amount of cross-talk between the S and aS channel and on the amount of background emission, after normalization both data sets accurately track the phonon dynamics. This demonstrates the broad tunability of our setup (limited here by the available filters) and the robustness of our technique.

**Conclusion** —Our scheme constitutes a broadly applicable technique for the time-resolved measurement of quantum correlations mediated by high frequency vibrational modes, which can be observed even at room-temperature due to their vanishing thermal occupancy. As we verified by rotating the linear polarization of the write beam, our scheme is polarization insensitive, so that it can be applied to any Raman-active mode. It is well suited to study quantum dynamics in individual nanosystems – in principle down to a single molecule (50). As shown in Ref. (14; 15; 16; 43; 19; 17; 44; 18; 45), Raman-active phonons are potential candidates for room-temperature quantum information processing. Our scheme extends the feasibility of this approach to a much broader range of material systems, which can be optimized for coupling efficiency and longer phonon lifetime.

The wide tunability of our setup will allow to leverage the resonant enhancement provided by electronic transitions or nanocavities, while spectral multiplexing and photon counting make it possible to measure cross-correlations between different normal modes (by triggering the start and stop detectors with two different Raman lines), thereby probing inter-mode coupling dynamics. Moreover, by triggering the coincidence counter upon multi-photon detection in the write step (using spatial (51; 52) or temporal (53) multiplexing or a direct photon number resolving detector (54; 55)), our technique would probe the dynamics of higher vibrational Fock states ( $n > 1$ ) (56). The probabilistic nature of the scheme, however, means that the rate of successful events will drop exponentially with  $n$ . Finally, this work constitutes the basis for more advanced measurement schemes where phonon coherences are measured using vibrational two-mode entangled states (57) and photon-phonon entangled states (58). This could lead to new ways of studying quantum phenomena in organic systems, which play essential roles in photochemistry and possibly in some biological reactions (59; 60).



**Acknowledgements** —We thank Pascal Gallo and Niels Quanck for providing diamond crystals; Mark Kasperczyk for helpful discussions regarding the experiment, Philippe Roelli, Nils Kipfer and Tianqi Zhu for assistance in the laboratory and Vivishek Sudhir for insightful discussion of the results. This work was made possible by the Swiss National Science Foundation (SNSF), through the grants number PP00P2-170684 and PP00P2-150579.

<sup>†</sup> M.D.A. and S.T.V. contributed equally to this work.

## Chapter 4. Two-Color Pump-Probe Measurement of Photonic Quantum Correlations Mediated by a Single Phonon

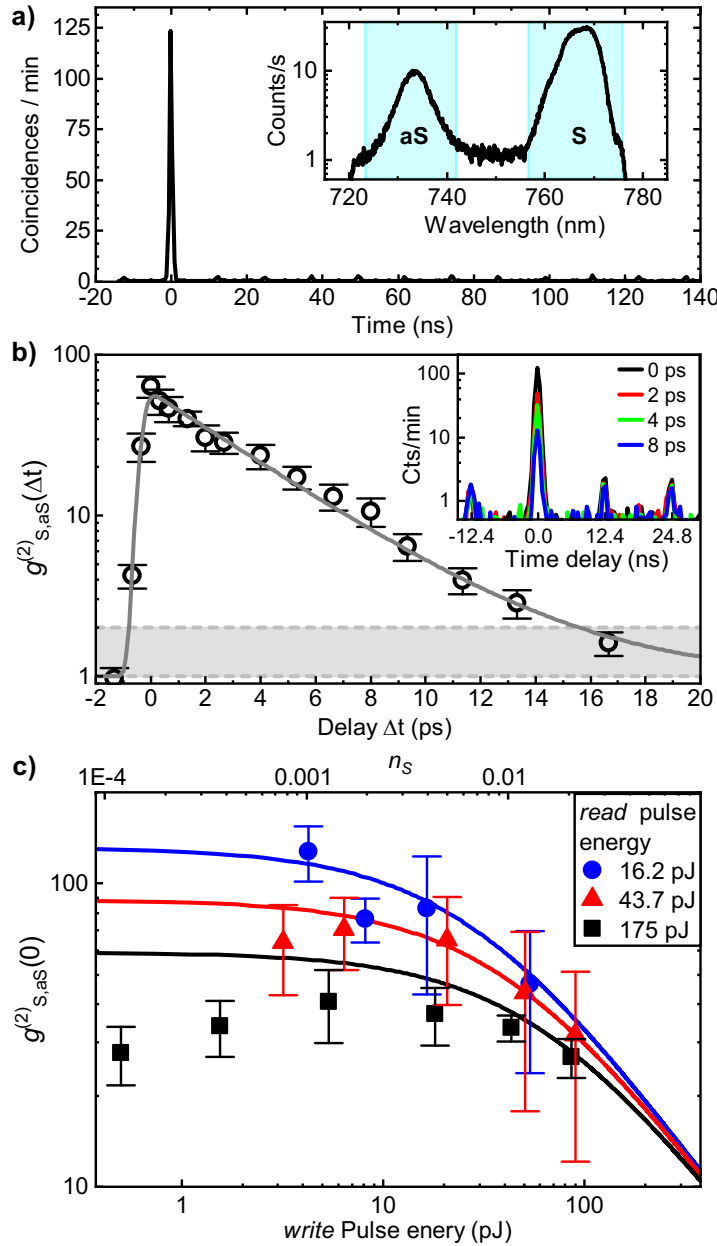


Figure 4.3: (a) S–aS coincidence histogram (20 min integration). The S (resp. aS) count rates were  $< 2.5 \cdot 10^4$  Hz (resp.  $< 8 \cdot 10^2$  Hz), with a dark count rate  $< 5 \cdot 10^2$  Hz. The OPO (resp. TiSapph) powers just after the sample were  $\sim 1.5$  mW (resp.  $\sim 3.5$  mW). Inset: representative Raman spectrum; the pass-bands of the filters placed before the S and aS detectors are overlaid in blue. (b) Write-read delay dependence of the measured S–aS correlation (open circles) and fit (dashed line) using an exponential decay (time constant  $= 3.9 \pm 0.7$  ps) convolved with the instrument response (Gaussian with standard deviation  $\sigma = 223$  fs). The gray area marks the classical bounds. Inset: coincidence histograms at different delays. (c) Measured SaS correlations at zero delay vs. average power in the *write* beam (symbols) for different powers in the *readout* beam.

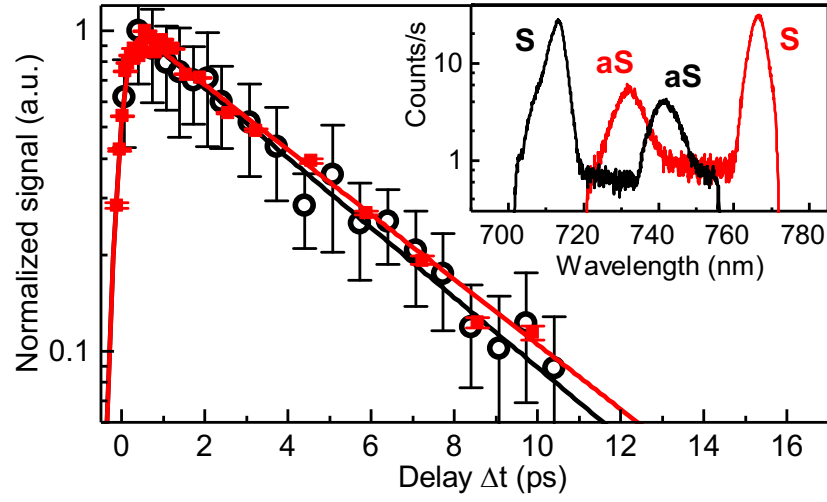


Figure 4.4: a) Decay of the normalized SaS correlation ( $g_{S,aS}^{(2)}(\Delta t) - 1 / (g_{S,aS}^{(2)}(0) - 1)$ ) (symbols) as a function of write-read delay  $\Delta t$  for two configurations of laser wavelengths (red and black colors), yielding S and aS peaks as shown in the inset. The fitted exponential decays (solid lines) have time constants  $4.2 \pm 0.5$  ps (red line) and  $4.0 \pm 0.3$  ps (black line).



## 5 Collective Vibrational Quantum Coherence in Spontaneous Raman Scattering

In this chapter, we use spontaneous Raman scattering to generate a collective vibrational excitation that is shared between two isotopic sub-ensembles. We illustrate the inherent coherence present in the Raman interaction, and use it to obtain a measurement of the lifetime of the two oscillations, as well as observe beating between them. Additionally, we use the model of the experiment to show that there is entanglement present in the quantum state we obtain.

I built the experiment, performed the measurements together with Dr. Anna Pogrebna, analyzed the data, and developed the theoretical model used to explain the results. The manuscript was prepared in collaboration with all the authors.

The content of this chapter is reproduced from:

**Tarrago Velez, Santiago**, Anna Pogrebna, and Christophe Galland. "Collective Vibrational Quantum Coherence in a Molecular Liquid under Spontaneous Raman Scattering." arXiv preprint arXiv:2105.00213 (2021).

which is currently undergoing peer-review.

Further information about the code used to perform the simulations can be found in Appendix 13.

### 5.1 Main text

*Introduction.*— Raman scattering was first reported in 1928 (10) and with the advent of laser sources it has become an essential tool for probing and understanding the vibrational structure of organic and inorganic matter. In a majority of experiments, a semi-classical model of light-matter interaction is sufficient to interpret the results of Raman spectroscopy. For example, the intensity asymmetry between Stokes and anti-Stokes scattering is obtained by quantizing the vibrational modes of each individual molecule. A full quantum theory of Raman scattering

## Chapter 5. Collective Vibrational Quantum Coherence in Spontaneous Raman Scattering

was developed in the 70's and 80's (61; 62; 63; 64; 65; 66), and its predictions were tested, e.g., by measuring intensity fluctuations in stimulated Raman scattering (67; 68).

Following a pioneering work by Walmsley and coworkers in 2011 (69), more recent experiments have used time-correlated single photon counting to evidence non-classical intensity correlations between light fields interacting with the same phonon mode via Raman scattering, with potential applications in ultrafast quantum information processing (70; 15; 16; 43; 71; 17), novel forms of spectroscopy (72; 73), and the generation of non-classical states of light (74). These experimental results have in turn spurred further theoretical developments to understand how the Raman process leads to photonic correlations mediated by a phononic excitation (75; 76), how the experimental geometry impacts the photon statistics of the Stokes field (77), and how the coupling of a Raman-active mode to a nanocavity modifies the dynamics of the system (78; 79; 80).

Despite this recent experimental progress, to our knowledge there has been no direct measurement of the nature of the vibrational quantum state generated in an ensemble of molecules in the liquid phase. Since molecule-molecule interactions in a liquid are in general incoherent and only contribute to vibrational relaxation (81), they cannot generate spatial coherence over mesoscopic length scales. Accordingly, most reference texts assume that coherence among different molecules can only be imposed by external driving, e.g. with the beat note between two strong laser fields as in coherent anti-Stokes Raman scattering (CARS) (82). Quantum coherence among different molecules following spontaneous Raman scattering in a dense molecular liquid has often been neglected (83; 84), implicitly assuming that the resulting collective vibrational state is a statistical mixture of individually excited molecules. We note that when studying an ensemble of identical molecules, the temporal coherence of the Stokes field (73; 85) or the presence of Stokes–anti-Stokes coincidences (18; 13) do not provide direct information about the collective coherence possibly existing among the molecules – which is why the authors from Ref. (13) could describe their experiment in terms of single-molecule scattering events.

In this Letter, we demonstrate that spontaneous Raman scattering naturally generates a collective vibrational excitation whose state is a quantum superposition of a macroscopic number of individually excited molecules in the liquid phase. To this end, we use a liquid of CS<sub>2</sub> that contains two dominant isotopic species (CS<sub>2</sub><sup>32</sup> and CS<sub>2</sub><sup>32</sup>S<sup>34</sup>) with distinct vibrational frequencies for the symmetric stretch mode separated by 8.6 cm<sup>-1</sup> (258 GHz); see Fig. 5.1. We measure time-resolved two-photon Stokes–anti-Stokes correlations mediated by the symmetric stretch mode, and observe long-lived quantum beats that are the signature of exciting a coherent superposition where a single vibrational quantum is shared by the two molecular sub-ensembles. As proposed in the context of cavity optomechanics (57), we also verify that our data is consistent with the emergence of mode entanglement between the two sub-ensembles, persisting for more than 4 ps. Our method constitutes a direct probe of the collective quantum coherence among individual molecules following spontaneous Raman scattering in a highly dissipative environment. When using a projective measurement on the Stokes field, the spatial extent

of vibrational coherence is determined not by the material properties (86; 87; 88) but by the spatial coherence of the incoming and detected optical fields.

*Experimental Results.*—We use the technique introduced in (89), where a first laser pulse generates a two-mode photon-phonon squeezed state via spontaneous Stokes Raman scattering. The power is adjusted to keep the probability of exciting a single phonon below  $\sim 10^{-2}$ , so that two-phonon processes have negligible impact on the measurement. A second laser pulse centered at a different wavelength is used to probe the phonon mode occupancy after a variable time delay  $\Delta t$ . This information is encoded in the Stokes–anti-Stokes correlation function  $g_{S,A}^{(2)}(\Delta t)$  (47; 41). The strength of phonon-mediated correlation is upper-bounded by  $g_{S,A}^{(2)} < 1 + 1/n_{th} \simeq 26$ , where the thermal occupancy of the vibrational mode is  $n_{th} \simeq 0.04$  in our system at room-temperature. A brief description of the experimental setup is provided in Fig. 5.2.

In Fig. 5.3 we show the normalised second order cross correlation function  $g_{S,A}^{(2)}$  measured on liquid  $\text{CS}_2$ , plotted as a function of time delay between Stokes and anti-Stokes processes. When write and read pulses are temporally overlapping, any four-wave mixing (FWM) process can generate photon pairs at any frequencies satisfying energy conservation, causing a rise in  $g_{S,A}^{(2)}$ . We used crossed-polarised laser pulses while filtering Raman photons that are co-polarised with the respective laser fields in order to minimize the relative contribution of FWM to the overall signal.

Information about the coherence and dynamics of the vibrational state is found at longer delays ( $\Delta t > 200$  fs). Assuming that spontaneous Raman scattering generates a statistical mixture of individually excited molecules, the expected decay is bi-exponential (because of the different linewidth of the two Raman peak, Fig. 5.1b), as shown by the dashed red line in Fig. 5.3. Instead, we observe oscillations with a period of around 3.7 ps (i.e. around  $9 \text{ cm}^{-1}$ ).

We note that oscillations resulting from the excitation of vibrational modes in different isotopes of  $\text{CCl}_4$  (90) were observed using ultrafast stimulated Raman scattering in Ref. (91; 92). However such experiments are well accounted for by a semi-classical model, in which the stimulated Stokes and anti-Stokes fields are classical. In the case of stimulated Raman scattering, the beating between the two pump laser fields is tuned resonant with the molecular vibration of interest, thereby driving a coherent collective vibration and resulting in a coherently oscillating Raman polarisation in the sample, all of which behave as classical variables.

In contrast, spontaneous Raman scattering and single photon counting demand a quantum description (detailed in the following section), in which the post-measurement vibrational state naturally appears as a quantum coherent superposition involving all molecules coupled to the light field. This quantum model makes predictions in good agreement with the data, after adjusting the relative contribution of FWM to fit the instantaneous response and taking into account detection noise. Moreover, the relative phase  $\theta$  that appears in the spontaneously generated quantum superposition of the two isotopic sub-ensembles translates into an horizontal shift of the oscillations. We find that taking  $\theta = \pi/6$  reproduces the position of the

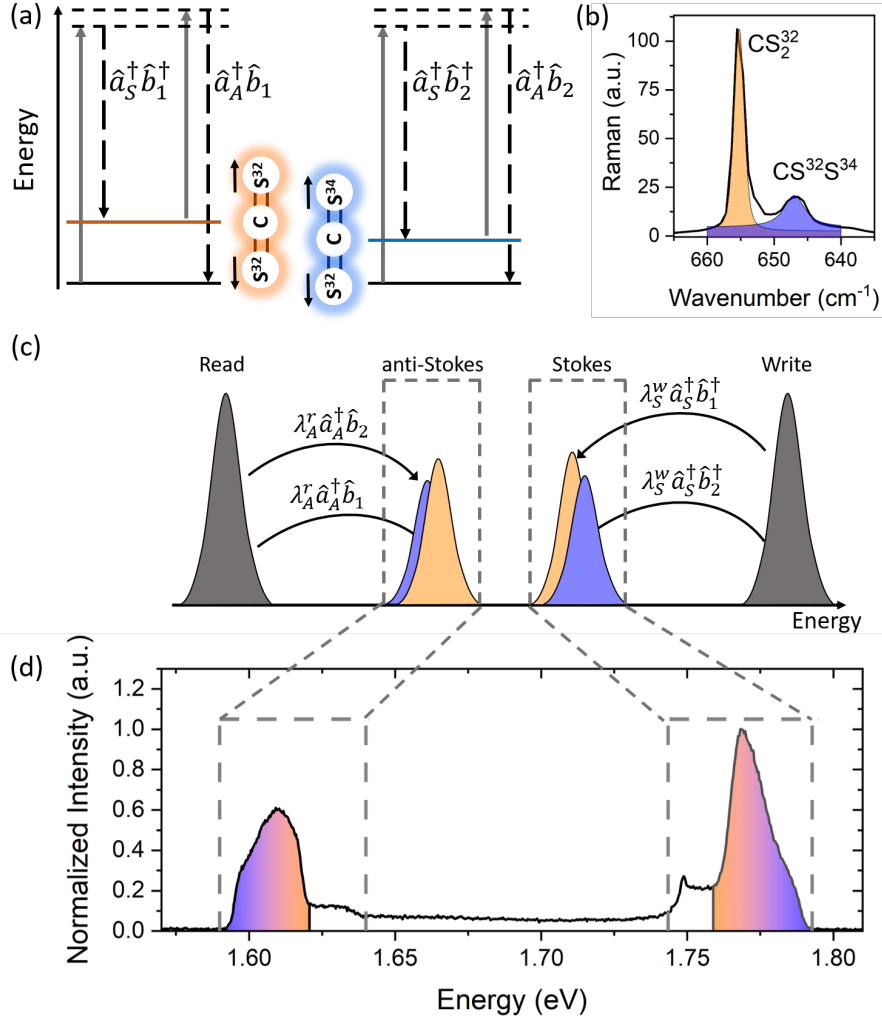


Figure 5.1: Experimental concept. **(a)** Energy levels involved in Raman scattering, where the solid grey arrows represent the incoming radiation, while the dashed black arrows represent the inelastically scattered photons. **(b)** Raman spectrum of  $\text{CS}_2$  measured with a 785 nm cw laser. The Raman peaks around 646  $\text{cm}^{-1}$  (shaded in orange) and 655  $\text{cm}^{-1}$  (shaded in blue) are fitted with Voigt functions with relative area 1.00 and 0.50, respectively. **(c)** Frequency-domain schematic illustration of the signals detected in our experiment. **(d)** Stokes and anti-Stokes Raman spectra of carbon disulfide measured with 200 fs laser pulses with photon energy 1.85 eV and 1.53 eV, respectively. The Stokes signal is observed around 1.77 eV, while anti-Stokes at 1.62 eV. The Raman photons scattered by the two different isotopes are no longer distinguishable (graded shade). The spectral regions selected by filters before the single photon detectors are approximately marked by the dashed boxes.



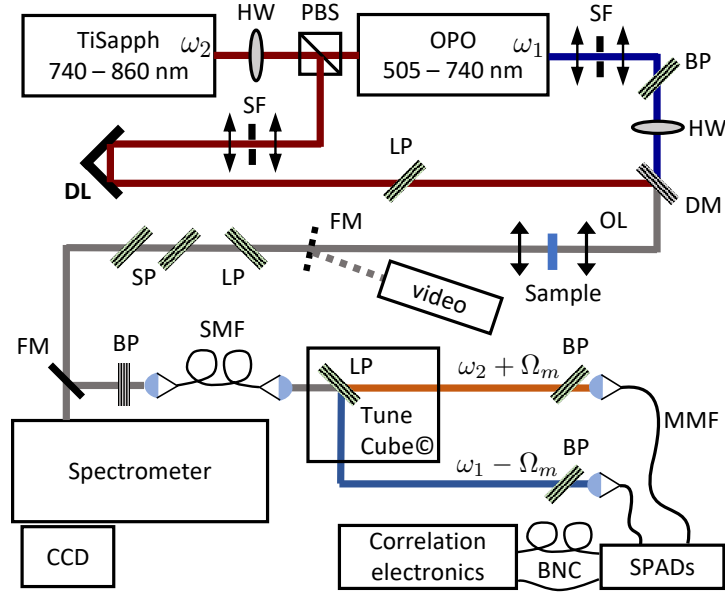


Figure 5.2: Sketch of experimental setup. The liquid  $\text{CS}_2$  (anhydrous,  $\geq 99\%$ , Sigma Aldrich) is held between two objective lenses (numerical aperture: 0.8) in a quartz cuvette sealed with parafilm with 0.2 mm wall thickness and 1 mm optical path. The sample is studied in transmission to fulfill momentum conservation in the Stokes – anti-Stokes process mediated by a collective vibration with vanishing momentum. The Raman signal is collected into a single mode optical fiber (SMF), whose back-propagated image overlaps with the focused laser beams to define a single spatial mode inside the sample. After spatial filtering through the fiber, the Stokes and anti-Stokes photons from the first and second pulses, respectively, are separated based on their non-overlapping spectra (see Fig. 5.1d). Fiber-coupled single photon avalanche photodiodes are connected to a custom coincidence counter to measure  $g_{S,A}^{(2)}$ . SP: shortpass; LP: longpass; BP: bandpass; Di: dichroic.

second oscillation peak. Our technique is therefore not only sensitive to the amplitudes in the quantum superposition but also to the relative phase.

*Theoretical description.*—The Raman interaction probabilistically generates a Stokes (resp. anti-Stokes) photon together with the creation (resp. annihilation) of a quantum of vibration. The two phonon modes of interest in our experiment (for the two isotopic sub-ensembles) are described by the annihilation operators  $\hat{b}_1$ ,  $\hat{b}_2$ . The Raman signals from the two phonon modes can be spectrally distinguished under cw excitation, but become indistinguishable under pulsed excitation, as shown in Fig. 5.1. Therefore, in the pulsed experiment with single spatial mode filtering, both vibrational modes effectively couple to the same Stokes and anti-Stokes photon fields, described by the annihilation operators  $\hat{a}_S^x$ ,  $\hat{a}_A^x$ , where  $x = w, r$  for the write and read pulses, respectively. The Raman interaction is modeled by the Hamiltonian

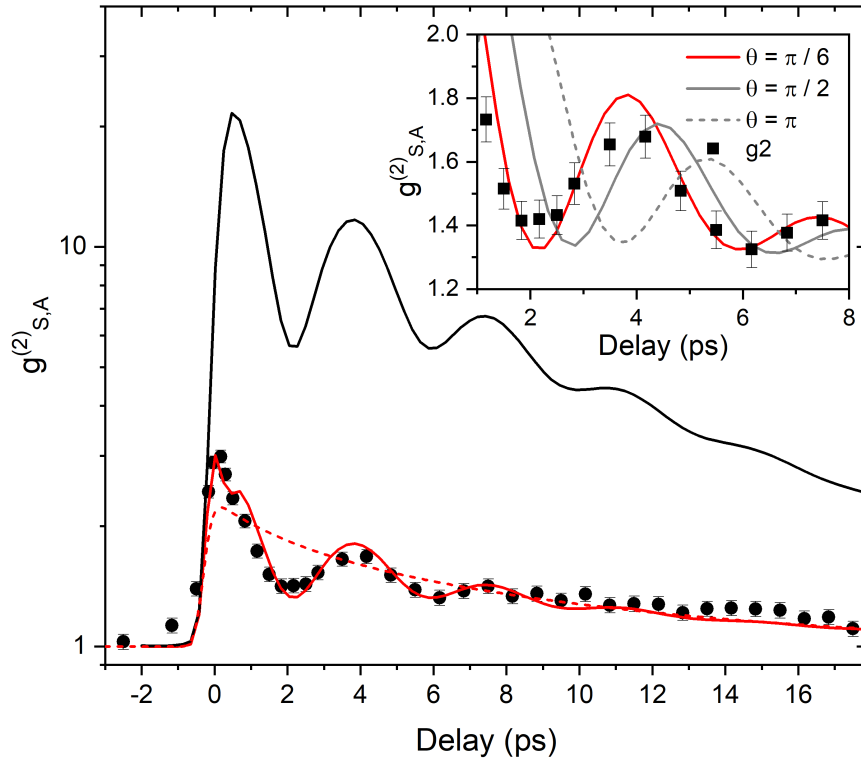


Figure 5.3: Write-read delay dependence of the measured normalised Stokes-anti-Stokes correlations (full circles) and model prediction (solid lines), for  $\theta = \pi/6$ . The red line represents the prediction including noise, while the black line shows the ideal case without any detection noise but with thermal noise (see text). The dotted red line represents the bi-exponential decay that would be expected if the vibrational state were a statistical mixture of individually excited molecules. The inset shows the model predictions for different values of the phase  $\theta$ .

(63)

$$\begin{aligned} \hat{H}_I^x = \hbar \alpha^x & \left[ \lambda_S^x (\hat{a}_S^x)^\dagger (\beta_1 \hat{b}_1^\dagger + e^{-i\theta_S^x} \beta_2 \hat{b}_2^\dagger) \right. \\ & \left. + \lambda_A^x (\hat{a}_A^x)^\dagger (\beta_1 \hat{b}_1 + e^{-i\theta_A^x} \beta_2 \hat{b}_2) \right] + h.c. \end{aligned} \quad (5.1)$$

where the laser is modeled by a coherent field of amplitude  $\alpha_x(t)$  ( $x = w, r$ ) with Gaussian envelope centered at time  $t_{0x}$  of width  $\sigma_x$ ,

$$\alpha^x(t) = A_x \exp\left(\frac{(t - t_{0x})^2}{2\sigma_x^2}\right) \exp(-i\omega_x t). \quad (5.2)$$

In eq. (5.1)  $\lambda_{S,A}^x$  determine the coupling strengths to the Stokes and anti-Stokes modes, and  $\beta_1, \beta_2$  control the relative weights of the two vibrational modes participating in the Raman interaction (experimentally related to the relative abundance and Raman cross-sections of the two main isotopic species), with  $\beta_1^2 + \beta_2^2 = 1$ . Since we use spectral filtering and post-selection to ignore events where an anti-Stokes (resp. Stokes) photon is emitted during the write (resp. read) pulse we can simplify the interaction model to

$$\hat{H}_I^w = \hbar \lambda_S^w \alpha^w (\hat{a}_S^w)^\dagger (\beta_1 \hat{b}_1^\dagger + e^{-i\theta_S^w} \beta_2 \hat{b}_2^\dagger) + h.c. \quad (5.3)$$

$$\hat{H}_I^r = \hbar \lambda_A^r \alpha^r (\hat{a}_A^r)^\dagger (\beta_1 \hat{b}_1 + e^{-i\theta_A^r} \beta_2 \hat{b}_2) + h.c. \quad (5.4)$$

(Note that the ignored terms contribute to uncorrelated noise photons generated via higher order Raman interactions during a single pulse (36).) We have explicitly written the two phase differences  $\theta_S^w$ , resp.  $\theta_A^r$ , appearing between the two vibrational modes during Stokes, resp. anti-Stokes, scattering. Our experiment is however only sensitive to their sum  $\theta = \theta_S^w + \theta_A^r$ . In the following we shorten the notation for the annihilation operators to  $\hat{a}_S^w \equiv \hat{a}_S$  and  $\hat{a}_A^r \equiv \hat{a}_A$ .

We include an additional  $\chi^{(3)}$  nonlinear interaction term that allows for the direct interaction between the write and read pulses, leading to the creation of photon pairs at the frequencies of the Stokes and anti-Stokes emission (FWM process):

$$\hat{H}_I^{(3)} = \hbar \lambda^{(3)} \alpha^w \alpha^r \hat{a}_S \hat{a}_A + h.c. \quad (5.5)$$

In the frame rotating with the central frequency  $\omega_0 = \frac{\omega_W + \omega_R}{2}$  we obtain the effective Hamiltonian

$$\begin{aligned} \hat{H} = \hbar \omega_1 \hat{b}_1^\dagger \hat{b}_1 + \hbar \omega_2 \hat{b}_2^\dagger \hat{b}_2 + \hbar \Delta_S \hat{a}_S^\dagger \hat{a}_S \\ + \hbar \Delta_A \hat{a}_A^\dagger \hat{a}_A + \hat{H}_I^w + \hat{H}_I^r + \hat{H}_I^{(3)} \end{aligned} \quad (5.6)$$

where  $\Delta_{S,A} = \omega_{S,A} - \omega_0$ . To account for dissipation we use the master equation approach, which includes coupling of the phonon modes to a thermal reservoir at room temperature, as

## Chapter 5. Collective Vibrational Quantum Coherence in Spontaneous Raman Scattering

described by the collapse operators

$$\begin{aligned}\hat{C}_{b1-} &= \sqrt{\kappa_1(1+n_{th})}\hat{b}_1 \\ \hat{C}_{b1+} &= \sqrt{\kappa_1 n_{th}}\hat{b}_1^\dagger \\ \hat{C}_{b2-} &= \sqrt{\kappa_2(1+n_{th})}\hat{b}_2 \\ \hat{C}_{b2+} &= \sqrt{\kappa_2 n_{th}}\hat{b}_2^\dagger\end{aligned}\tag{5.7}$$

where  $\kappa_x$  is related to the decay rate of the phonon modes by  $\tau_{ph_x} = 1/\kappa_x$ . The temporal evolution of the density matrix is computed numerically using QuTiP, an open-source library used for simulating quantum systems in Python (93; 94).

*Coincidence counts under non-ideal conditions.*— To account for noise and losses in the experiment we use the operator introduced in (24) to model the photon detection probability

$$\hat{D}_X = 1 - (1 - p_X^{dc})(1 - \eta_X)^{\hat{a}_X^\dagger \hat{a}_X}\tag{5.8}$$

where  $X = S, A$  for the Stokes and anti-Stokes detection channels, respectively. The dark count probability (per detection time window) is  $p_X^{dc}$  while  $\eta_X$  is the detection efficiency. The experimental value of the normalised Stokes – anti-Stokes coincidence rate  $g_{S,A}^{(2)}$  is then calculated (for several values of  $\Delta t = t_{0r} - t_{0w}$ ) as

$$g_{S,A}^{(2)} = \frac{\langle \hat{D}_S \hat{D}_A \rangle}{\langle \hat{D}_S \rangle \langle \hat{D}_A \rangle}\tag{5.9}$$

*Choice of model parameters.*— Most of the model parameters are extracted from the cw Raman spectra and the average single detector count rates during the experiment, leaving only the total phase  $\theta$  and the coupling strength of the FWM process  $\lambda^{(3)}$  as fitting parameters. We find the relation between the count rate in the cw experiment and the parameters  $\beta_1, \beta_2$ , by considering the state  $|\psi\rangle = \beta_1|1\rangle_{b_1} \otimes |0\rangle_{b_2} + \beta_2|0\rangle_{b_1} \otimes |1\rangle_{b_2}$ : Under cw excitation the photons scattered by the two vibrational modes are distinguishable, and their photon number is proportional to  $\beta_1^2$  and  $\beta_2^2$ . From the integrated area under the two main peaks in the cw spectrum shown in Fig. 5.1 we find approximately  $\beta_1 = \sqrt{1/3}, \beta_2 = \sqrt{2/3}$ .

The detection efficiency of our setup is estimated to be  $\eta_S \approx \eta_A \approx 10\%$ . We fix the values of the parameters  $A_x$  and  $\lambda_{S,A}^x$  by considering the Stokes and anti-Stokes detection rates. As the pulse amplitudes  $A_x$  always appear in factor with the coupling rates  $\lambda^x$ , we introduce  $\Lambda_{S,A}^x = A_x \lambda_{S,A}^x$  whose values are chosen to reproduce the measured single-detector count rate when only the write or read pulse is propagating through the sample. We find  $\Lambda_S^w = 0.104$  and  $\Lambda_A^r = 0.136$ , which recover the measured detection probabilities  $p_S \approx 2.7 \times 10^{-4}$ ,  $p_A \approx 1.8 \times 10^{-5}$ . The dark count probabilities are estimated to be  $p_S^{dc} \approx 2 \times 10^{-4}$  and  $p_A^{dc} \approx 1 \times 10^{-5}$ .

The coupling rates of the phonon modes to the thermal bath, which govern their decay times, is calculated from the FWHM  $\Delta\nu$  of each peak as measured by cw Raman spectroscopy. We fit the peaks with a Voigt function, which assumes a Lorentzian line shape for the peaks and

a Gaussian response for the spectrometer, and use the FWHM of the Lorentzian curve to determine the lifetime of each phonon mode. The FWHM is related to the dephasing rate  $\Gamma$  of a phonon mode by  $\Gamma = \pi\Delta\nu$ . In the absence of pure dephasing, the phonon lifetime will be  $\tau_{ph} = 1/2\Gamma$ . We use this assumption to find  $\tau_{ph_1} = 8.4 \pm 1.3$  ps and  $\tau_{ph_2} = 1.7 \pm 0.2$  ps. With these parameters, the model outputs the full red line in Fig. 5.3, while the black line is the inferred signal in the absence of FWM and detection noise.

*Fock State Populations and Entanglement.*—As our model generates the full density matrix we can gain further insights into the dynamics and entanglement of the vibrational modes. We first compute the probabilities of observing different phonon numbers (Fock states) knowing that the Stokes detector registered a photon (95; 96), as a function of time after the Stokes scattering event; Fig. 5.4. Our evaluation includes the experimental noise, as we use the operator  $\hat{D}_S$  to model the detection of one or more Stokes photons; it can therefore be considered as a faithful estimate of the post-selected vibrational state in the experiment. Moreover, we can compute the amount of entanglement existing between the two vibrational modes, which we quantify via the Logarithmic Negativity  $E_N$ , an entanglement monotone defined by  $E_N = \log_2 \|\rho^{T_{b_2}}\|$ , where  $\rho^{T_{b_2}}$  indicates the partial transpose of  $\rho$  with respect to the phonon mode  $b_2$ , and  $\|X\| \equiv \text{tr}(\sqrt{X^\dagger X})$  (97; 98). Fig. 5.4 shows that the two vibrational modes do become entangled ( $E_N > 0$ ), and that the entanglement survives for about 4.5 ps, decaying at a rate similar to that of  $\tau_{ph_2}$ , the faster decaying phonon mode.

*Conclusions.*—To summarize, we presented a measurement of time domain spectrally resolved two-photon Stokes–anti-Stokes correlations on liquid CS<sub>2</sub> at room temperature. We showed that spontaneous Raman scattering can generate a quantum superposition of two collective vibrational excitations of different isotopic sub-ensembles, which leads to quantum beats in the two-photon coincidence counts vs. time delay. Our experimental results are incompatible with the picture according to which spontaneous Raman scattering from a large ensemble is always the incoherent sum (statistical mixture) of single-molecule scattering events. Our experiment nourishes the debate about the relation between optical coherence and quantum coherence (99; 100) and entanglement (101). It questions whether optical coherent states are necessary to explain various forms of coherent Raman spectroscopy, for we do not stimulate the Raman process and yet observe coherent oscillations, as if we did. In the future, our photon counting approach can be adapted to probe inter- or intramolecular vibrational entanglement in more complex systems, as well as excitonic and vibrational polariton dynamics (102). We also envision extensions of our work to probe how Raman scattering is affected by collective excitonic (103; 104; 105; 106) or vibrational (107; 108; 109; 110; 111; 112) strong coupling to a cavity, with implications for polariton chemistry (113).

## Acknowledgements

The authors thank Vivishek Sudhir for insightful discussions and valuable comments. This work has received funding from the Swiss National Science Foundation (SNSF) (project no.

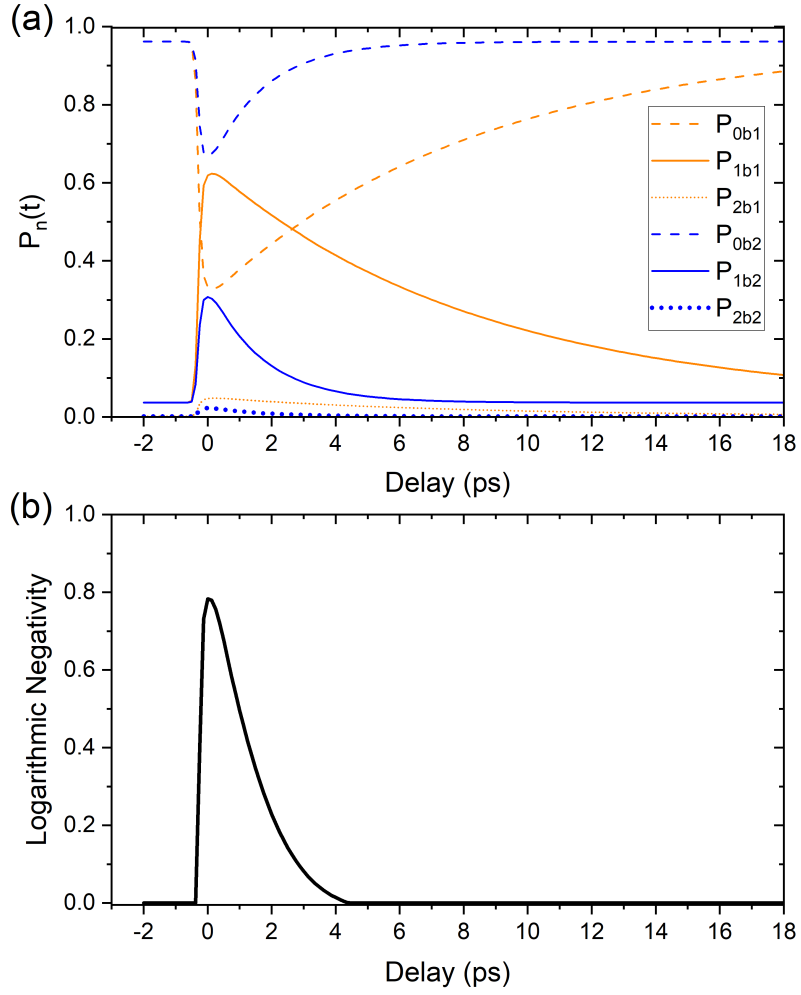


Figure 5.4: **(a)** Populations in the Fock state basis of the two vibrational modes (blue and orange lines) for the conditional state after heralding of a Stokes event, including all types of noises in the detection process (cf. red line in 5.3). **(b)** Entanglement between the two vibrational modes in this heralded state is quantified by the Logarithmic Negativity  $E_N$ , shown as black solid line.

PP00P2-170684) and the European Research Council's (ERC) Horizon 2020 research and innovation programme (grant agreement no. 820196) A. P. acknowledges funding from the European Union's Horizon 2020 research and innovation programme under the Marie Skłodowska-Curie grant agreement N° 754462.





## 6 Preparation and decay of a single quantum of vibration at ambient conditions

In this chapter, we take a closer look at the vibrational state that is created during the Raman interaction. We demonstrate the preparation of the 40 THz vibrational mode of diamond in the  $n=1$  Fock state. We show that, by detecting a Stokes photon that has been scattered from an ultrafast laser pulse, the vibration is prepared in the first Fock state with 98.5% probability. We perform a Hanbury-Brown-Twiss intensity correlation measurement, and show that the statistics of the vibration change from thermal to sub-Poissonian through the interaction with the 'write' laser, and track the change in statistics as the phonon decays.

I performed the experiments and analyzed the data. The manuscript was prepared in collaboration with all the authors.

The content of this chapter is reproduced from:

**Tarrago Velez, Santiago**, Kilian Seibold, Nils Kipfer, Mitchell D. Anderson, Vivishek Sudhir, and Christophe Galland. "Preparation and decay of a single quantum of vibration at ambient conditions." *Physical Review X* 9, no. 4 (2019): 041007.

Further information about the code used for instrument control and data analysis can be found in Appendix 10

### 6.1 Main Text

The observation of inelastic scattering of photons from ensembles of atomic-scale particles was an early triumph of quantum theory. Within a few years, experiments by Compton (114) and Raman (10) showed that photons can exchange energy and momentum with material particles in the manner described by quantum mechanics. At optical frequencies, Raman scattering, the dominant effect, is an expression of the universal idea that a mechanical vibration phase-modulates the outgoing light, resulting in two scattered sidebands (Fig. 6.1a,b). In a quantum description, the upper ("anti-Stokes") sideband arises from the annihilation of a

## Chapter 6. Preparation and decay of a single quantum of vibration at ambient conditions

quantum of vibration, while the lower (“Stokes”) arises from its creation (Fig. 6.1c).

Leveraging the Raman interaction, a variety of pump-probe measurements have been implemented to study vibrational dynamics in crystals and molecules. For example, incoherent phonons generated by the decay of electron-hole pairs can be probed by time-resolved anti-Stokes scattering (115; 116; 117; 118). Several techniques have also been developed to study coherent states of the vibrational modes. The most popular is time-resolved coherent anti-Stokes Raman scattering, where a large coherent phonon population is excited by a pair of laser pulses, and its classical decay is probed by a delayed pulse (119). Another technique – transient coherent ultrafast phonon spectroscopy – uses the interference of the Stokes photons from the spontaneous Raman scattering of two coherent pumps to determine the decoherence of the vibrational mode (72; 120). While these techniques reveal the time scales over which the vibration decays or loses its phase coherence, observing single quanta of the vibration itself has proved far more elusive.

To illustrate the difficulty, consider that on the one hand, internal vibrational modes of crystals and molecules with oscillation frequencies in the 10-100 THz range ubiquitously and naturally exist in their quantum ground state at room temperature. But unless they are individually addressed and resolved within their coherence time, the ensemble average over unresolved vibrational modes precludes the observation of individual quanta. Despite this challenge, a Raman-active vibration featuring a specific form of internal nonlinearity was prepared in a squeezed state by optical excitation (121), while polarization-selective Raman interactions were used to observe two-photon interferences mediated by a vibrational mode (122). On the other hand, nano-fabricated mechanical oscillators can be susceptible to a universal radiation pressure interaction with light, especially with the intense fields stored in an optical cavity (123). However, their relatively low frequency (MHz-GHz) means that thermal energy at room temperature is larger than the energy of a single vibrational quantum, making quantum state manipulation difficult or impossible under ambient conditions. Precise measurements of mechanical motion at room temperature have recently revealed quantum characteristics of the underlying radiation pressure interaction (39; 40; 124). But it is only through deep cryogenic operation that quantum states of motion of nano-scale oscillators have been prepared in the last years (125; 42; 126; 127; 128). Thus, the quest to prepare quantum states of commonly available mechanical oscillators at ambient conditions remains largely open.

Here we prepare a non-classical state of an internal vibration of a diamond crystal at room temperature. In a scheme inspired by the DLCZ protocol (129; 47), a femtosecond laser pulse (the “write” pulse hereafter) first creates an excitation from the ambient motional ground state with a probability  $p \ll 1$  (see Fig. 6.1c). Detection of the emitted Stokes photon heralds the success of this step, while choice of the spectral window for detection fixes the specific vibrational mode of the system under study. To verify that only a single quantum of vibration was excited, a second laser pulse (the “read” pulse) retrieves it as an anti-Stokes photon. The probability of having two or more anti-Stokes photons, and therefore two or more quanta of vibrations, is obtained by performing a Hanbury-Brown-Twiss (HBT) intensity correlation

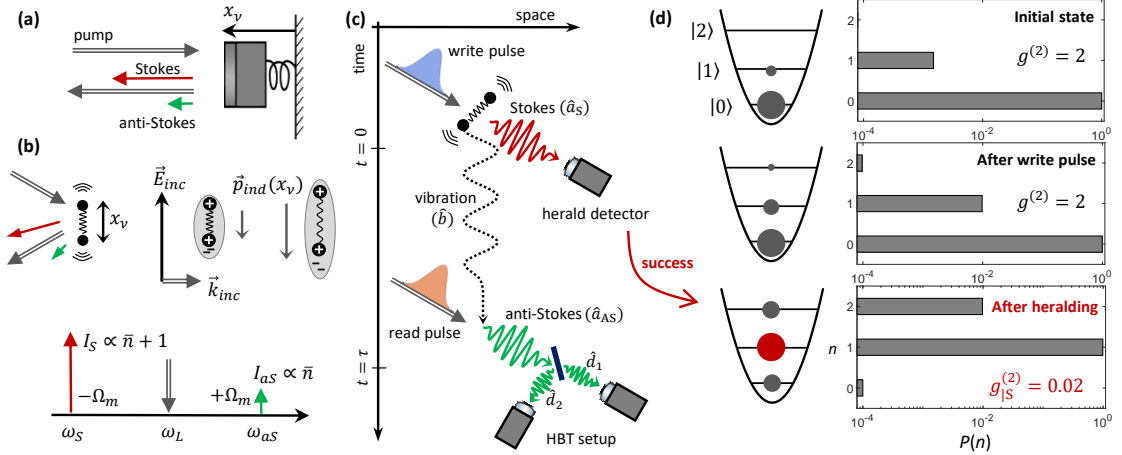


**Figure 6.1: Concept of the experiment.** (a) When monochromatic light reflects from an oscillating mirror, it acquires two Raman sidebands due to phase modulation (to first order in interaction strength). (b) When light interacts with a polarizable oscillator, whose induced polarization  $\vec{p}_{ind}$  depends on its internal coordinate  $x_v$ , it undergoes a phase modulation at the oscillator frequency, leading to the appearance of Stokes and anti-Stokes Raman sidebands in the scattered light. The anti-Stokes/Stokes intensity ratio is proportional to  $\frac{\bar{n}}{\bar{n}+1}$  where  $\bar{n}$  is the mean excitation number (or occupancy) of the vibrational mode. (c) Time evolution of a single repetition of the experiment showing the interaction of the write pulse, the subsequent detection of Stokes photons for heralding, and the final read pulse followed by measurement of two-photon correlation in the emitted anti-Stokes light. (d) Evolution of the probability  $P(n)$  of finding the vibrational mode in the  $n^{\text{th}}$  energy eigenstate during the different steps. The system is initially in a thermal state with  $\bar{n} = 1.5 \cdot 10^{-3}$  (for a mode frequency of 40 THz at 295 K). After the write pulse, the marginal state of the vibration is also thermal with  $\bar{n} = \frac{p}{1-p} = 10^{-2}$  in this example (here  $p$  is the interaction probability). Finally, after heralding, the distribution becomes peaked at  $n = 1$ . The residual vacuum component is due to detection noise. For each distribution, we give the corresponding value of the vibrational mode's intensity correlation function  $g^{(2)}$ .

measurement on the anti-Stokes photons conditioned on the heralding signal (130; 131). We observe sub-Poissonian statistics of the heralded vibrational state, a result consistent with having prepared the Fock state  $|1\rangle$  of the vibrational mode (the first excited energy eigenstate). Finally by changing the delay between the write and read pulses we probe the decay of the single vibrational quantum, with  $\approx 200$  fs resolution.

In contrast to previous quantum optics experiments on Raman-active vibrational modes that were restricted to molecular or crystal structures exhibiting particular polarization rules (122; 14; 15; 16; 43; 19; 17) or vibrational nonlinearities (121), our technique is agnostic to these details, and can be employed on any Raman-active subject. It opens a plethora of opportunities to study vibrational quantum states and dynamics in other crystals and in molecules, and can readily be extended to create vibrational two-mode entangled states (57) and test the violation of Bell inequalities (58; 132) at room-temperature in a number of widely available systems.

## 6.2 Theoretical description

The Raman interaction between a single vibrational mode and an optical field leads to the creation of an anti-Stokes (Stokes) photon commensurate with the destruction (creation) of a vibrational quantum. In our experiment the Raman interaction is driven by an optical field that may either be a “write” (superscript w) or “read” (superscript r) pulse defined by the spatial and temporal mode of a mode-locked laser whose beam is focused onto the sample. These two incident fields are described by the annihilation operators  $\hat{a}^{w,r}$ . The interaction leads to the generation of Stokes and anti-Stokes photons whose spatial mode is post-selected by projecting the focal spot onto the core of a single-mode optical fiber. The Stokes (anti-Stokes) fields are modeled by annihilation operators  $\hat{a}_S^{w,r}$  ( $\hat{a}_{AS}^{w,r}$ ). Due to conservation of energy and momentum in the Raman scattering process, the detection of these scattered fields as described above defines a single spatio-temporal mode of the vibration that is the subject of the experiment, and which we describe by its annihilation operator  $\hat{b}$ . The Raman interaction is modeled by the Hamiltonian (133),

$$\hat{H}_{\text{int}}^w = i\hbar \left[ G_S^w \hat{a}^w \hat{b}^\dagger (\hat{a}_S^w)^\dagger + G_{AS}^w \hat{a}^w \hat{b} (\hat{a}_{AS}^w)^\dagger \right] + \text{h.c.} \quad (6.1a)$$

$$\hat{H}_{\text{int}}^r = i\hbar \left[ G_S^r \hat{a}^r \hat{b}^\dagger (\hat{a}_S^r)^\dagger + G_{AS}^r \hat{a}^r \hat{b} (\hat{a}_{AS}^r)^\dagger \right] + \text{h.c.}, \quad (6.1b)$$

where the coupling rates  $G_S^{w,r}$  and  $G_{AS}^{w,r}$  relate to the Raman activity of the vibrational mode.

None of the four processes described by eq. (6.1) is resonant since we work at photon energies well below the band gap of diamond (5.47 eV). However, because we spectrally filter and detect only the two modes  $\hat{a}_S^w$  and  $\hat{a}_{AS}^r$  all essential results of our measurements can be described by the Hamiltonian

$$\hat{H}_{\text{int}}^w = i\hbar g_S^w \hat{b}^\dagger \hat{a}_S^\dagger + \text{h.c.} \quad (6.2a)$$

$$\hat{H}_{\text{int}}^r = i\hbar g_{AS}^r \hat{b} \hat{a}_{AS}^\dagger + \text{h.c.}, \quad (6.2b)$$

where we defined the effective coupling rate,  $g_{S,AS}^{w,r} \equiv G_{S,AS}^{w,r} \sqrt{n_p^{w,r}}$ , corresponding to a classical excitation for the write/read pulses with  $n_p^{w,r}$  photons per pulses, and used the shorter notation  $\hat{a}_S \equiv \hat{a}_S^w$ ,  $\hat{a}_{AS} \equiv \hat{a}_{AS}^r$ . In fact, this scenario is equivalent to the linearized radiation-pressure interaction (123), or Raman processes in atomic ensembles (129), where an optical cavity (in the former instance) or electronic resonance (in the latter) suppresses non-resonant terms.

Note that the Hamiltonian in eq. (6.2) neglects higher order interactions, in particular the creation of correlated Stokes/anti-Stokes pairs during a single pulse (write or read) via phonon-assisted four-wave mixing (134; 12; 36; 37; 12; 13; 38). In our experiment, the photon flux due

to this higher-order interaction constitutes an effective background noise (135). Other extraneous sources of photons, such as from residual  $\chi^{(3)}$  nonlinearities, or fluorescence, also lead to an excess background noise. The spontaneous Stokes signal scales linearly with laser power since it is proportional to  $n_p^w(\bar{n} + 1) \approx n_p^w$ , where  $\bar{n} \ll 1$  is the average occupation of the vibrational mode. In our experiment, the spontaneous Raman signal is much stronger than any of the parasitic processes described above, so that the fidelity of the heralded state is only marginally affected by noise. However, the anti-Stokes signal, being proportional to  $n_p^r \bar{n}$ , is significantly weaker, so that noise cannot be neglected in this case. The measured normalized probability of detecting two anti-Stokes photon should therefore be considered as an upper-bound for the corresponding probability of having two vibrational quanta. In the calculations presented below, the noise terms are accounted for in order to faithfully describe the experiment.

### 6.2.1 Write operation

The first step in an iteration of the experiment is the excitation of the vibrational mode by a write pulse. The resulting dynamics of the vibrational and Stokes modes is governed by  $H_{\text{int}}^w = i\hbar g_S^w \hat{b}^\dagger \hat{a}_S^\dagger + \text{h.c.}$ , which has the form of a two-mode squeezing interaction, and leads to the creation of maximally correlated pairs of vibrational and Stokes excitations. When both modes are initially in the vacuum state  $|\text{vac}\rangle$ , the final state after the write pulse is (131),

$$|\Psi\rangle_{S,b} = \sqrt{1-p} \sum_{n=0}^{\infty} \sqrt{p^n} |n, n\rangle_{S,b} \quad (6.3)$$

where  $|n, n\rangle_{S,b} \equiv \frac{(\hat{b}^\dagger \hat{a}_S^\dagger)^n}{n!} |\text{vac}\rangle$ . For the simple situation of a constant interaction switched on for a duration  $T_w$ , the probability of exciting the state  $|1, 1\rangle$  is given by,  $p = \tanh^2(g_S^w T_w)$ . For realistic laser pulse shapes, in the linear regime,  $T_w$  is the effective interaction time defined by the equivalent square pulse that carries the same pulse energy. Ideally, when at least one Stokes photon is detected, the (conditional) state of the vibrational mode becomes (see Supplementary information),  $\rho_{b|S} \approx |1\rangle\langle 1| + p|2\rangle\langle 2|$ , in the limit where  $p \ll 1$ ; crucially, the vacuum component in  $|\Psi\rangle_{S,b}$  has been eliminated based on the presence of a Stokes photon. Dark noise in real photodetectors (modeled as a probability  $\pi_0$  per pulse) prevents unambiguous discrimination of the vacuum contribution. However, when the total Stokes signal is larger than the dark noise, it can be shown (see Supplementary information) that the resulting conditional state,

$$\hat{\rho}_{b|S} \approx \frac{\pi_0}{2\eta p} |0\rangle\langle 0| + |1\rangle\langle 1| + p|2\rangle\langle 2|, \quad (6.4)$$

is dominated by the contribution from the pure Fock state  $|1\rangle$ . Here  $\eta$  is the detection efficiency of the Stokes field, and  $\eta p$  is the Stokes detection probability. The signal-to-noise ratio in the Stokes photodetector  $\eta p / \pi_0$  is larger than  $10^4$  in our experiment.

### 6.2.2 Read operation

Once the Stokes photon is detected, a second pulse – the read pulse – is used to retrieve the (conditional) state of the vibrational mode. The dynamics of the anti-Stokes field induced by the read pulse is described by the Hamiltonian  $H_{\text{int}}^r = i\hbar g_{\text{AS}}^r \hat{b} \hat{a}_{\text{AS}}^\dagger + \text{h.c.}$ , which represents a beam splitter interaction between the anti-Stokes and vibrational modes. For an effective interaction time  $T_r$ , the state of the emitted anti-Stokes field is governed by the input-output relation,

$$\hat{a}_{\text{AS,out}}(T_r) = \cos(\theta) \hat{a}_{\text{AS,in}} + \sin(\theta) \hat{b}, \quad (6.5)$$

where,  $\theta \equiv g_{\text{AS}}^r T_r$ . The mode  $\hat{a}_{\text{AS,in}}$  describes the input anti-Stokes mode (before the read pulse), which is in the vacuum state.

The crucial aspect of the read operation is that the emitted anti-Stokes field faithfully reflects the number statistics of the vibrational mode. In fact, from eq. (6.5), we find that  $\langle : (\hat{a}_{\text{AS}}^\dagger \hat{a}_{\text{AS}})^n : \rangle = \sin^{2n}(\theta) \langle : (\hat{b}^\dagger \hat{b})^n : \rangle$ , for any integer  $n \geq 1$  (here  $::$  denotes normal ordering). This relation expresses the fact that photon counting is insensitive to vacuum noise (in stark contrast to linear detection of the field (136)), so that normalized moments of the photon number of the anti-Stokes field faithfully represent the statistics of the vibrational mode excitation number.

Note that although the interaction between the optical pulses and the vibrational mode is linear (eq. (6.2)), the nonlinearity provided by the single-photon detection following the write and read pulses renders the full measurement process effectively nonlinear (137). It is this single-photon nonlinearity that lies at the conceptual heart of our protocol.

### 6.2.3 Statistics of the heralded intensity correlation

Performing the two operations presented above enables the preparation and unambiguous characterization of a vibrational Fock state. Consider the joint state  $|\Psi\rangle_{\text{S,b,AS}}$  for the Stokes field, the vibration, and the anti-Stokes field. A heralded coincidence event occurs when a Stokes photon is detected at time  $t = 0$ , followed, after a time  $t$ , by coincident detection of a pair of anti-Stokes photons. This heralded coincidence event is represented by the measurement map,

$$|\Psi\rangle_{\text{S,b,AS}} \mapsto \hat{d}_2(t) \hat{d}_1(t) \hat{a}_{\text{S}}(0) |\Psi\rangle_{\text{S,b,AS}},$$

where  $\hat{d}_{1,2}$  are the operators denoting the anti-Stokes field at the two output of a 50/50 beam-splitter (see fig. 6.1c). The probability of this triple coincidence defines the conditional intensity correlation, and is thus proportional to  $\langle \hat{a}_{\text{S}}^\dagger(0) \hat{d}_1^\dagger(t) \hat{d}_2^\dagger(t) \hat{d}_2(t) \hat{d}_1(t) \hat{a}_{\text{S}}(0) \rangle$ ; here we have used the linearity of quantum mechanics to extend the definition to mixed states as well. Suitably normalizing the expression (46) allows us to define the conditional intensity

correlation,

$$g_{\text{AS|S}}^{(2)}(t) \equiv \frac{\langle \hat{a}_S^\dagger(0) \hat{d}_1^\dagger(t) \hat{d}_2^\dagger(t) \hat{d}_2(t) \hat{d}_1(t) \hat{a}_S(0) \rangle}{\prod_i \left[ \langle \hat{a}_S^\dagger(0) \hat{d}_i^\dagger(t) \hat{d}_i(t) \hat{a}_S(0) \rangle \langle \hat{a}_S^\dagger(0) \hat{a}_S(0) \rangle^{-1/2} \right]}.$$

The fields  $\hat{d}_{1,2}$  whose intensity cross-correlation is measured can be expressed in terms of the anti-Stokes field  $\hat{a}_{\text{AS}}$ , which in turn can be expressed in terms of the vibration (via eq. (6.5)); since intensity correlations do not respond to the vacuum, the open port of the beam-splitter used in the intensity correlation measurement plays no role, and the conditional correlation above can be written as,

$$g_{\text{AS|S}}^{(2)}(t) = \frac{\langle \hat{a}_S^\dagger(0) \hat{b}^\dagger(t) \hat{b}^\dagger(t) \hat{b}(t) \hat{b}(t) \hat{a}_S(0) \rangle}{\langle \hat{a}_S^\dagger(0) \hat{a}_S(0) \rangle^{-1} \langle \hat{a}_S^\dagger(0) \hat{b}^\dagger(t) \hat{b}(t) \hat{a}_S(0) \rangle^2}. \quad (6.6)$$

After the detection of a Stokes photon (i.e. for  $t > 0$ ), the state of the vibrational mode (eq. (6.4)) has disentangled from that of the Stokes mode, so that expectation values of products of operators in their joint state factorize into products of expectation values; thus,

$$g_{\text{AS|S}}^{(2)}(t > 0) = \frac{\langle \hat{b}^\dagger(t) \hat{b}^\dagger(t) \hat{b}(t) \hat{b}(t) \rangle_{\text{S}}}{\langle \hat{b}^\dagger(t) \hat{b}(t) \rangle_{\text{S}}^2} = g_{b|\text{S}}^{(2)}. \quad (6.7)$$

That is, the conditional intensity correlation of the anti-Stokes field gives the intensity correlation of the vibrational mode. Immediately after the write pulse, i.e. at  $t = 0$ , and in the limit of a small probability  $p$  of exciting a vibrational Fock state, explicit evaluation of eq. (6.6) on the state  $|\Psi\rangle_{\text{S,b}}$  of eq. (6.3) yields

$$g_{\text{AS|S}}^{(2)}(0) \approx \frac{4P(2,2)}{P(1,1)} = 4p \quad (6.8)$$

where  $P(n, n) = \langle n, n | (|\Psi\rangle_{\text{S,b}} \langle \Psi|) | n, n \rangle = p^n$  is the probability of finding  $n$  pairs of excitations in the vibrational mode and Stokes field upon a projective measurement on state (6.3) in the Fock state basis.

In our experiment we measure the number of events  $N_{d_1, d_2, a_S}$  where photons were detected simultaneously in modes  $d_1, d_2$ , and  $a_S$  (i.e. triple coincidence), and normalize it to the product of the number of events  $N_{d_i, a_S}$  ( $i = 1, 2$ ) where photons are detected simultaneously in the Stokes mode and one of the anti-Stokes detectors (i.e. a two-fold coincidence); we thus measure (130),

$$\alpha \equiv \frac{N_{d_1, d_2, a_S} N_{a_S}}{N_{d_1, a_S} N_{d_2, a_S}}. \quad (6.9)$$

It is important to note that, in general,  $\alpha$  is not equivalent to  $g_{\text{AS|S}}^{(2)}$  in eq. (6.8). More precisely, if the detection efficiency of the herald mode  $a_S$  is  $0 < \eta \leq 1$  (which we model as a beam splitter with transmittance  $\eta$  placed before the detector) we find (see Supplementary information)

$$\alpha \approx (4 - 2\eta) \frac{P(2,2)}{P(1,1)} = (4 - 2\eta) p. \quad (6.10)$$

Thus, in the limit of low detection efficiency of Stokes photons (i.e.  $\eta \ll 1$ ) we have that  $\alpha = g_{\text{AS|S}}^{(2)}$ . In the experiment,  $\eta \approx 10\%$ , so that  $\alpha \approx g_{\text{AS|S}}^{(2)}$  (to within 5 %).

### 6.3 Experimental Realization

#### 6.3.1 Setup and measurement procedure

Our experimental setup is an upgraded version of that presented in ref. (135). Two synchronized laser pulse trains at 810 nm and 695 nm of duration  $\Delta t \approx 100$  fs are produced by a Ti:Sa oscillator (Tsunami, Spectra Physics, 80 MHz repetition rate) and a synchronously pumped frequency-doubled optical parametric oscillator (OPO-X fs, APE Berlin), respectively. The write pulses are provided by the OPO, while the Ti:Sa provides the read pulses, which are passed through a delay line before being overlapped with the OPO output on a dichroic mirror. The sample is a synthetic diamond crystal ( $\sim 300$   $\mu\text{m}$  thick, from LakeDiamond) cut along the (100) crystal axis and is probed in transmission using two microscope objectives (numerical aperture 0.8 and 0.9). The laser light is blocked using long-pass and short-pass tunable interference filters (Semrock), leaving only a spectral window of transmission for the Stokes signal from the write pulse (mode  $a_{\text{S}}$ ) and the anti-Stokes signal from the read pulse (mode  $a_{\text{AS}}$ ). The transmission is collected in a single mode fiber (for spatial mode filtering) and then the two signals are separated with a tunable long-pass filter used as a dichroic mirror. After an additional band-pass filter (see Supplementary Information, Section VI) each signal is coupled into a multi-mode fiber; subsequently, the Stokes field is sent to a single photon counting module (SPCM, Excelitas), while the anti-Stokes field is split at a 50:50 fiber beam-splitter and directed onto two SPCM's. The three SPCM's are then connected to a coincidence counter (PicoQuant TimeHarp 260).

We only record the coincidence events where a click in one of the anti-Stokes channels was preceded by a click in the Stokes channel. This allows us to find heralded coincidence events (within the same laser repetition), as well as to build a delay histogram using the Stokes channel as the start and either of the anti-Stokes channels as the stop. These start-stop histograms are used to compute the Stokes – anti-Stokes intensity cross-correlation as explained in (135). Therefore all relevant coincidences required to estimate  $\alpha$  are available.

#### 6.3.2 Ambient thermal state

We start by verifying that following the write pulse the Stokes field is well described by the state of eq. (6.3): when marginalized over the state of the vibrational mode, the Stokes field is thermal. Indeed, we find in Fig. 6.2 (red bars) that the intensity correlation function of the Stokes field at zero time delay is  $g_{\text{S}}^{(2)}(0) = 2$ , as expected for a single mode thermal state.



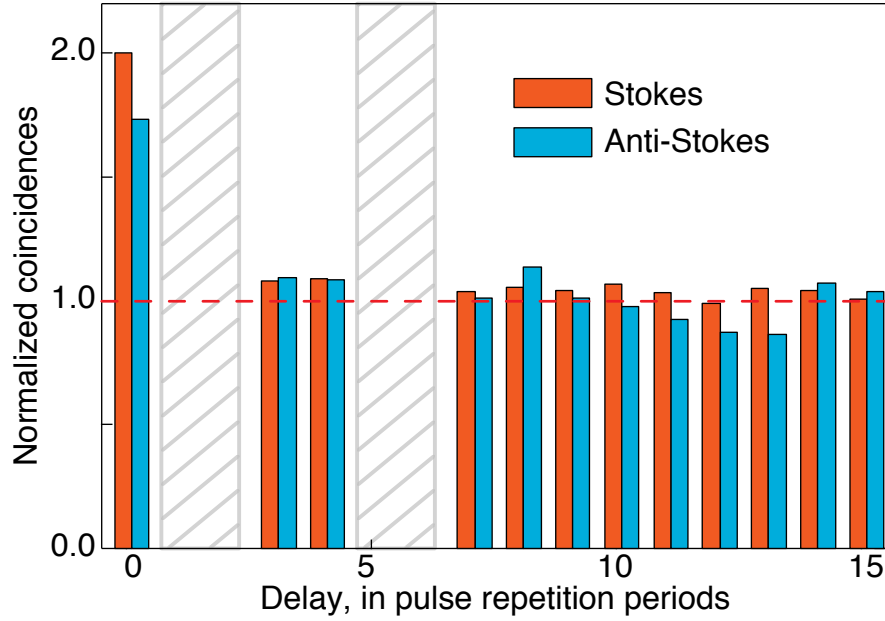


Figure 6.2: **Unconditional Stokes and anti-Stokes correlations.** Two-photon coincidence histograms of the Stokes field  $\hat{a}_S$  (write pulse energy 60 pJ, acquisition time 10 min) and anti-Stokes field  $\hat{a}_{AS}$  (read pulse energy 372 pJ, acquisition time 60 min). For the anti-Stokes field the coincidences are recorded between the detectors measuring  $\hat{d}_1$  and  $\hat{d}_2$  as in Fig. 6.1b, while the write pulse is blocked. For the measurement of the Stokes field, a beam splitter is added in the path of mode  $\hat{a}_S$ . The start-stop delay (horizontal axis) is scaled in multiples of the repetition period  $\approx 12.5$  ns. After normalizing by the average number of accidental coincidences (the peaks non-zero start-stop) the value at zero time delay represents the intensity correlation of the Stokes and anti-Stokes fields, namely  $g_S^{(2)}(0) = 2.0 \pm 0.1$  and  $g_{AS}^{(2)}(0) = 1.73 \pm 0.11$ . The hatched region in gray, omitted in the analysis, are affected by spurious coincidences due to cross-talk between the two detectors, which arise when hot-carrier-induced light emission from one detector (138) is received by the other detector.

Similarly, in the absence of the write operation, the anti-Stokes signal should reflect the thermal statistics of the vibrational mode. To check this, we measure the (unconditional) intensity correlation of the anti-Stokes mode, shown in Fig. 6.2 (blue bars). The value of  $g_{AS}^{(2)}(0) = 1.73 \pm 0.11$ , is slightly lower than the expected value of 2 for a single mode thermal state, but higher than the value  $1 + \frac{1}{N}$  for a thermal state of  $N > 1$  modes (24). We attribute this discrepancy to noise in the anti-Stokes channel coming from degenerate four-wave mixing in the sample (which includes the second-order Stokes–anti-Stokes process (36) discussed earlier). We thus confirm a single vibrational mode in an ambient thermal state, and that the result of the write operation is well described by the two-mode squeezed state of eq. (6.3).

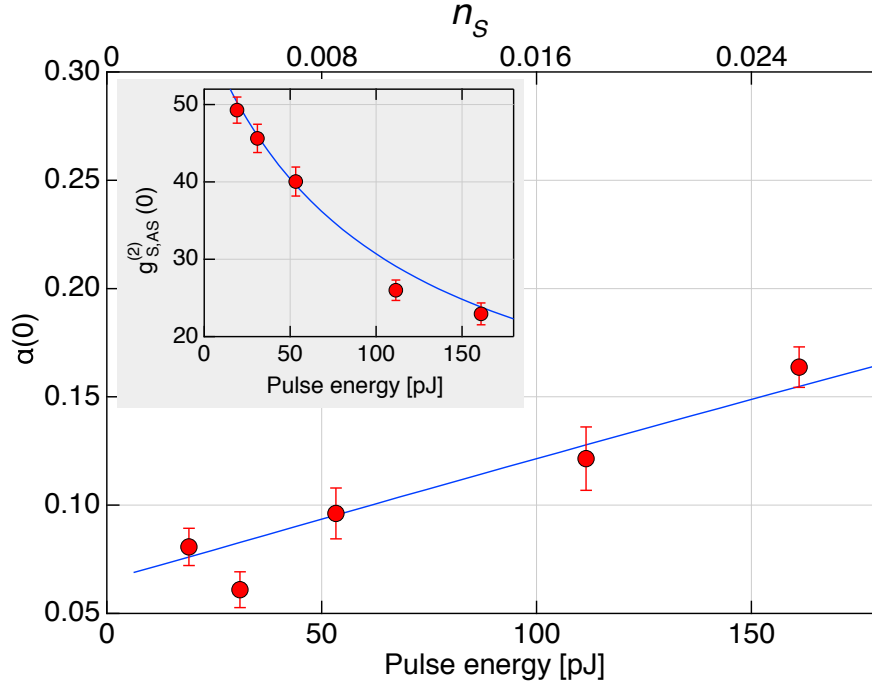


Figure 6.3: **Sub-Poissonian anti-Stokes statistics.** Dependence of the heralded vibrational statistics on the write pulse energy and on the corresponding estimated probability of creating at least one Stokes photon per pulse,  $n_S = \frac{p}{1-p}$ . The normalized Stokes–anti-Stokes correlations are shown as an inset. The write–read pulse delay is fixed at zero and the read pulse energy at 322 pJ. Statistical error bars are obtained from the square root of the total number of events. Blue lines are models (see Supplementary Information), using the estimated detection efficiency (10 %) and a relative efficiency of the read process (relative to the Stokes emission cross-section) of 30 % as the only two adjustable parameters (common to both panels).

### 6.3.3 Fock state preparation

In order to prepare the vibrational mode in a Fock state, we send a write pulse and herald the success of this operation by detecting a Stokes photon. When a subsequent read pulse retrieves the vibrational state, and is subjected to intensity correlation measurements, we find that  $\alpha(0) \approx g_{AS|S}^{(2)}(0) < 1$ , as shown in fig. 6.3 (main panel). Thus, the conditional anti-Stokes field exhibits sub-Poissonian statistics. But since we know that the anti-Stokes field is faithful to the vibrational state, and specifically that  $g_{AS|S}^{(2)} = g_{b|S}^{(2)}$ , we are able to conclude that the vibrational mode exhibits sub-Poissonian number statistics. From the value of  $\alpha(0) \approx 0.06$  at the lowest powers of the write pulse and the known detection efficiency of the Stokes field  $\eta \approx 10\%$ , our theoretical model allows us to estimate the probability of having excited the Fock state  $|1\rangle$  to be (eq. (6.10)),  $1 - p \approx 98.5\%$ .

With increasing power of the write pulse, mixtures of states higher up in the Fock ladder are excited. As shown in Fig. 6.3, the sub-Poissonian character of  $\alpha$  decreases with increasing pump power, as expected from the simple model  $\alpha(t=0) \propto p = \tanh^2(g_S^w T_w) \approx (g_S^w T_w)^2 \propto n_p^w$ ,

where  $n_p^w$  is the number of photons per write pulse. in tandem, the Stokes–anti-Stokes correlation reduces as  $1/n_p^w$  (Fig. 6.3 inset). These trends are consistent with increasing probability of exciting two or more vibrational quanta (139; 24) (see Supplementary Information).

### 6.3.4 Fock state dynamics

The decay of the excited vibrational Fock state can be probed by allowing it to evolve freely after the write pulse. In the experiment, we do this by employing a variable optical path length to impose a time delay  $t$  between the write and read pulses. Figure 6.4 summarizes the observed time-dependence of the excited Fock state. When the write and read pulses overlap ( $t = 0$ ), we observe strong Stokes–anti-Stokes number correlation  $g_{S,AS}^{(2)}(0) \approx 30$ , consistent with the generation of a Stokes-vibration two-mode squeezed state (eq. (6.3)).

Simultaneously,  $\alpha$ , which reflects the intensity correlation of the conditioned vibrational state (eq. (6.4)), indicates sub-Poissonian statistics of the vibrational mode, with  $\alpha(t = 0) \approx 0.11 < 1$ . Conditional on the detection of a Stokes photon, the vibrational mode is thus faithfully prepared in the Fock state  $|1\rangle$ .

Subsequent iterations of the experiment probe the vibrational state after a controlled time delay. Figure 6.4a shows the decay of the Stokes–anti-Stokes correlation. The initial value  $g_{S,AS}^{(2)}(0)$  quantifies the degree to which the Stokes field and vibrational mode are correlated by the write operation; at later times  $t > 0$ , after the Stokes field is detected,  $g_{S,AS}^{(2)}(t) \propto \langle \hat{b}^\dagger(t) \hat{b}(t) \rangle_S$ , so that the data in Fig. 6.4a, in conjunction with a model (shown in blue, consisting of the ideal prediction convolved with the known instrument response), allows us to infer the decay rate  $\tau_m = 3.9 \pm 0.3$  ps (bounds for 95% confidence). This value is consistent with the previously reported vibrational lifetime of 3.6 ps (14).

In parallel, as shown in fig. 6.4b,  $\alpha(t)$  mirrors this evolution, starting at  $\alpha(t < 0) = 1.9 \pm 0.6$  (thermal state), dropping to  $\alpha(0) = 0.11 \pm 0.01$  at zero delay (Fock state  $|1\rangle$ ), and then returning toward its equilibrium value as the prepared vibrational Fock state thermalizes with its environment. (The larger uncertainty in the data at long and at negative delays is due to the reduced rate of coincidences, because of the small thermal occupancy,  $\bar{n} \approx 1.5 \cdot 10^{-3}$ , of the vibrational mode.) This behaviour is captured by a simple model (shown as a blue line in Fig. 6.4b), based on the fact that  $\alpha(t)$  is the intensity correlation of the vibrational mode (eq. (6.7)) – which can be calculated using an open quantum system model for the vibrational mode – together with a contribution from background noise in the anti-Stokes field (see Supplementary Information),

$$\alpha(t) \approx \frac{2}{P_1(0)} \left[ 1 - \frac{1}{(1 + \bar{n}(e^{t/\tau_m} - 1))^2} \right] + \alpha_0, \quad (6.11)$$

where  $P_1(0) \approx 0.985$  is the probability of having created the vibrational Fock state  $|1\rangle$  conditioned upon the detection of a Stokes photon, and  $\alpha_0 = 2 \times 0.04$  corresponds to twice the anti-Stokes noise-to-signal ratio conditioned on Stokes detection (i.e.,  $\alpha_0/2 \approx 1/g_{S,AS}^{(2)}(0)$ ), see

## Chapter 6. Preparation and decay of a single quantum of vibration at ambient conditions

Supplementary Information). The decay of sub-Poissonian statistics of the vibrational mode is consistent with the decay of the Fock state  $|1\rangle$  to the ground state  $|0\rangle$ .

The measured decay of the conditional intensity correlation, in conjunction with a decoherence model, can be used to extract the number distribution  $P_n(t)$  of the conditional vibrational state (see Supplementary Information) – the probability to find the vibrational mode in the Fock state  $|n\rangle$  at time  $t$  after a click on the Stokes detector. This projection is plotted in Fig. 6.4c. Noteworthy is the high purity of the conditional vibrational state with respect to the Fock state  $|n = 1\rangle$ , since its normalized second order correlation is  $\frac{2P_2}{P_1^2} \approx 0.02$ . This is much lower than the measured parameter  $\alpha \approx 0.1$  (because the background noise impinging on the anti-Stokes detectors affects  $\alpha$ ) and highlights the potential of the technique to produce high-purity single phonons.

### 6.4 Conclusion

We have demonstrated for the first time that a high-frequency Raman-active vibrational mode can be prepared in its  $n = 1$  Fock state at room temperature. Heralded intensity correlation measurements confirm the sub-Poissonian statistics of the conditional vibrational state. We further probed the decay of the vibrational Fock state, akin to similar measurements on microwave photons (56; 140).

This research opens a door to the study of quantum effects in the vibrational dynamics of Raman-active modes in immobilized molecules (50), liquids, gases (44; 18; 45) and solid-state systems. Vibrational states in Raman-active solid-state systems at room temperature may even be viable candidates for quantum technology if the coherence time and readout efficiency can be improved. Coherence of the longitudinal optical phonon modes of diamond is known to be limited by decay through the so-called Klemens channel (141; 142; 49). Proposals to close this pathway include the creation of a phononic band gap at the atomic scale obtained by growing  $^{12}\text{C} - ^{13}\text{C}$  super lattices (14). Readout efficiency and heralding rate could be improved by coupling the Raman-active system to small-mode volume optical or plasmonic cavities (78; 143; 144), or by employing resonant Raman scattering (145; 118). Molecular systems are particularly promising for extending the vibrational lifetime (146). With these improvements, vibrational modes may be used as a source of high-purity on-demand (anti-Stokes) photons, or as a buffer memory to produce heralded single photons with an arbitrary choice of the herald and signal wavelengths and/or bandwidths, or even heralded frequency conversion at the single photon level.

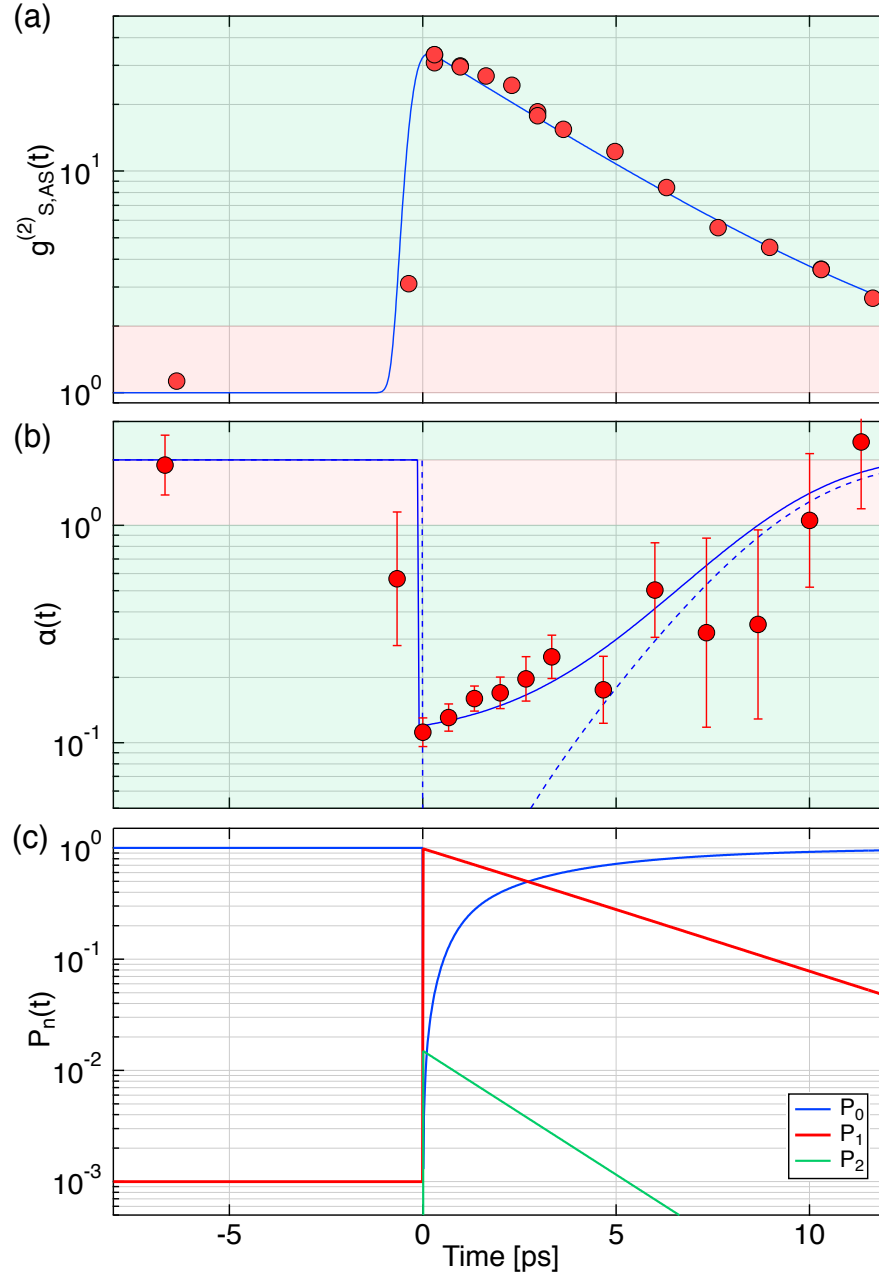


Figure 6.4: **Decay of vibrational Fock state.** Measured Stokes–anti-Stokes correlations (a), and heralded vibrational mode intensity correlation (b) as a function of write–read delay. The measurements (full circles) are taken with a pulse energy of 62 pJ in the write pulse and 409 pJ in the read pulse, with an acquisition time of 60 min for all points except the one at  $-6.3$  ps, which was acquired over 8 hours. Statistical error bars are obtained from the square root of the total number of events detected in each case. Full circles are measured data and blue lines are from the model, see main text and eq. (6.11). The prediction from the model without the added noise on the anti-Stokes detectors is shown with a dashed line in (b). Green bands in panels (a,b) show the region where a non-classical model is required to explain the observations; red bands indicate where a classical model suffices. (c) Fock state distribution of the conditional vibrational mode inferred from the data via our model.



## 7 Bell correlations between light and vibration

In this chapter we demonstrate Bell correlations between light and a collective vibration in diamond. We experimentally demonstrate a violation of the CHSH inequality that persists for  $\sim 5$  ps, and which has a maximum value of  $S = 2.360 \pm 0.025$ . We provide a detailed description of the experimental implementation, and provide a thorough model predicting our results and accounting for experimental imperfections.

I designed the experiment in collaboration Prof. Christophe Galland and Prof. Nicolas Sangouard. I made the necessary modifications to the experimental setup, performed the experiment, and analyzed the data. The manuscript was prepared in collaboration with all the authors.

The content of this chapter is reproduced from:

**Tarrago Velez, Santiago**, Vivishek Sudhir, Nicolas Sangouard, and Christophe Galland. "Bell correlations between light and vibration at ambient conditions." *Science Advances* 6, no. 51 (2020): eabb0260.

Further information about the code used for instrument control and data analysis can be found in Appendix 12.

Additionally, we show an alternative way of modeling the experiment in Appendix 11, where we use the Jones matrix formalism to explore the potential sources of error present in the experiment. The approach is not as rigorous as the one presented in this chapter, but the intuition it provides was invaluable when building and troubleshooting the experiment.

### 7.1 Main Text

In the hierarchy of non-classical states, the Bell correlated states represent an extreme. When two parties share such a state, information can be encoded exclusively in the quantum correlations of the random outcomes of measurements between them (30; 147). The strength of

## Chapter 7. Bell correlations between light and vibration

---

such correlations is quantified by Bell inequalities, whose violation demarcates Bell correlated states from less entangled ones (34).

Experimental realizations of Bell correlated states — whether between polarization states of light (148; 31), individual atomic systems(149; 150; 151), in atomic ensembles (152; 153; 154), superconducting circuits (155; 156), or solid-state spins (157; 158) — call for isolated systems that strongly interact with a well-characterized probe. Even mesoscopic acoustic resonators have been engineered to exhibit Bell correlations (132) thanks to long coherence times (achieved at milli-Kelvin temperatures) and strong interaction with light (by integration with an optical micro-cavity).

Intriguingly, recent experiments have shown that high-frequency vibrations of bulk crystals (69; 159; 12; 160; 43; 135) or molecular ensembles (18; 13; 38) can mediate non-classical intensity correlations between inelastically scattered photons under ambient conditions (i.e. at room temperature and atmospheric pressure). In the pioneering work of Lee et al. (69), two phonon modes in spatially separated bulk diamonds had been entangled with each other by performing coincidence measurements and post-selection on the Raman-scattered photons. Recently, leveraging a new two-tone pump-probe method (135), it became possible to follow the birth and death of an individual quantum of vibrational energy (i.e. Fock state) excited in a single spatio-temporal mode of vibration in a bulk crystal (161).

Remarkably, these experiments did not necessitate specially engineered subjects; they reveal fundamental quantum properties of naturally occurring materials. Taken together, these developments raise new questions: Are the correlations spontaneously created between light and vibration during Raman scattering strong enough to violate Bell inequalities? How is the vibrational coherence time reflected in the dynamics of the hybrid light-vibration quantum correlations?

In this Letter, we demonstrate for the first time Bell correlations arising from the Raman interaction between light and mechanical vibration at ambient conditions, and use them to resolve the decoherence of the vibrational mode mediating these correlations. While this proof-of-principle experiment is realized on a vibrational mode in a bulk diamond crystal, the effect that is revealed should be universally observable in Raman-active molecules and solids. Indeed, our scheme for producing hybrid photon-phonon entanglement is agnostic to sample details and is passively phase-stabilized, while our two-color pump-probe technique can address Raman-active vibrations irrespective of any polarization selection rules – all of which differ from earlier work (69). Our results demonstrate the strongest form of quantum correlations and is thus a powerful generalization of techniques deployed in atomic physics to study the decoherence of entanglement (162).



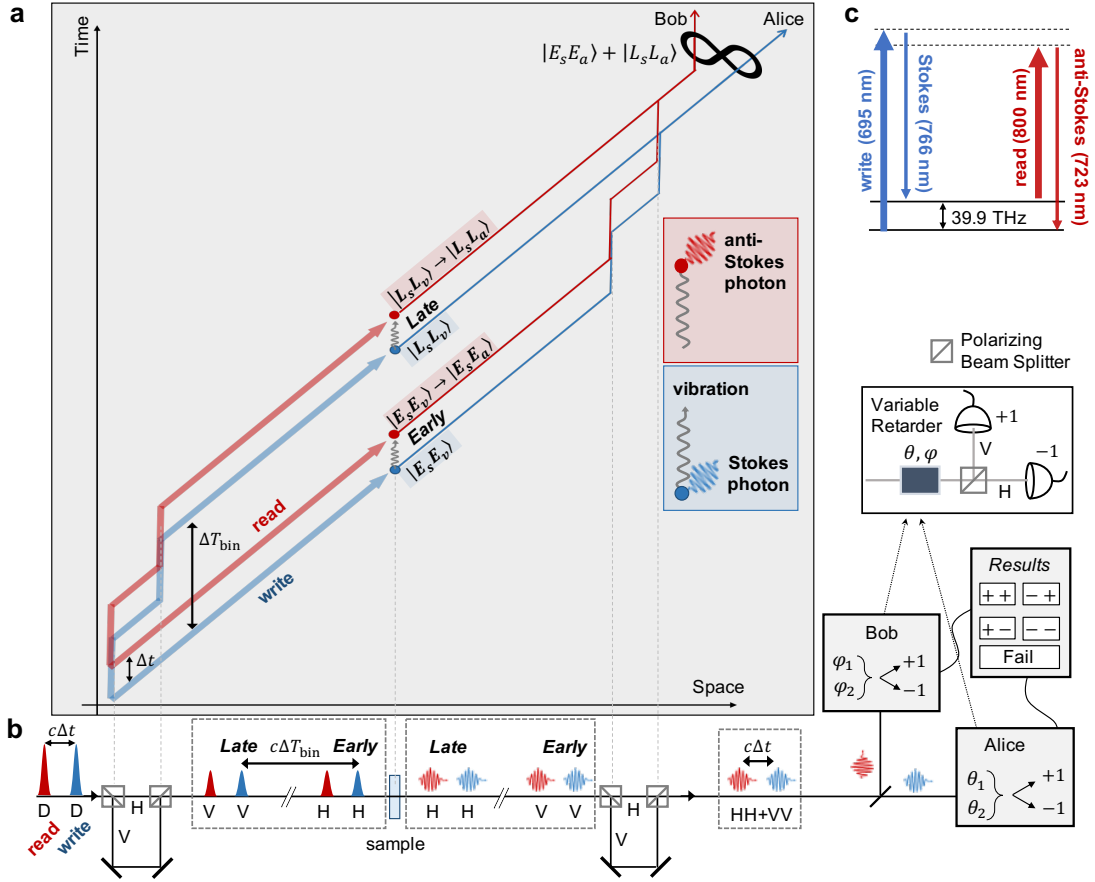


Figure 7.1: **Conceptual scheme and simplified experimental layout.** **a**, Space-time diagram representation of the time-bin entanglement procedure. **b**, Corresponding experimental implementation unfolded in space along the horizontal axis (see Suppl. Material, Section 1 for details). Contents of the dashed boxes illustrate the time sequence and polarization of the excitation pulses (Gaussian wavepackets) and Raman-scattered photons (wavy arrows), during a single repetition of the experiment. The polarization states are denoted by D (diagonal), H (horizontal) and V (vertical). Note that in our geometry the polarization of Raman scattered photons is orthogonal to that of the incoming pulses. The vertical dashed lines in panel **a** correspond to different points in space along the setup. **c**, Energy diagram of the relevant Raman interactions, showing the center wavelengths used in the experiment.

## Materials and Methods

The inelastic scattering of light off an internal vibrational mode — vibrational Raman scattering — is analogous to the radiation-pressure interaction between light and a mechanically compliant mirror (78). Specifically, the Raman interaction consists of two processes. In the Stokes process, a quantum of vibrational energy  $\hbar\Omega_v$  (a phonon) is created together with a quantum of electromagnetic energy  $\hbar\omega_s$  (a Stokes photon); in the anti-Stokes process a phonon is annihilated while an anti-Stokes photon is created at angular frequency  $\omega_a$ . Energy conservation demands that  $\omega_{s,a} \pm \Omega_v = \omega_{\text{in}}$  respectively, where  $\omega_{\text{in}}$  is the frequency of the

incoming photon.

In our experiment, a diamond sample — grown along the [100] direction by high-pressure high-temperature method, about  $300\ \mu\text{m}$  thick and polished on both faces along the (100) crystallographic plane — is excited with femtosecond pulses from a mode-locked laser through a pair of high numerical aperture objectives (NA=0.8). (The effective length over which the Raman interaction takes place is of the order of  $2\ \mu\text{m}$ .) Since the pulses are shorter than the coherence time of the Raman-active vibration, but longer than its oscillation period, there exists perfect time correlation between the generation (resp. annihilation) of a vibrational excitation and the production of a Stokes (resp. anti-Stokes) photon. In the following, we show how to leverage this time correlation to generate time-bin entanglement (163) between two effective photonic qubits that reveal properties of the mediating phonon mode, and quantify the strength of the quantum correlations using the CHSH form of the Bell inequality (148).

The scheme (Fig. 7.1) starts when a pair of laser pulses, labeled “write” and “read” impinging on the sample. Each is a classical wavepacket with  $\sim 10^8$  photons per pulse. Their central frequencies are independently tunable, which allows spectral filtering of the Stokes field generated by the write pulse and the anti-Stokes field generated by the read pulse, which are sent to separate detection apparatuses. The delay between them,  $\Delta t$ , is adjustable to probe the decoherence of the vibrational mode. Each pulse passes through an unbalanced Mach-Zehnder interferometer and is split in two temporal modes separated by  $\Delta T_{\text{bin}} \gg \Delta t$ , which we label the “early” and “late” time bins.  $\Delta T_{\text{bin}} \simeq 3\ \text{ns}$  is chosen to be much longer than the expected vibrational coherence time, which ensures that there can be no quantum-coherent interaction between the two time bins mediated by the vibrational mode.

At room temperature, the thermal state of the vibrational mode (161) (at 39.9 THz) as a mean occupancy  $1.5 \times 10^{-3}$ . The initial state of the vibration in the two time bins is therefore very well approximated by the ground state  $|0_v\rangle \equiv |0_{v,E}\rangle \otimes |0_{v,L}\rangle$ , where the subscripts  $E$  and  $L$  stand for the early and late time bins, respectively. The Stokes ( $s$ ) and anti-Stokes ( $a$ ) fields are also in the vacuum state at the start of the experiment, denoted by  $|0_s\rangle \equiv |0_{s,E}\rangle \otimes |0_{s,L}\rangle$  and  $|0_a\rangle \equiv |0_{a,E}\rangle \otimes |0_{a,L}\rangle$ .

The interaction of the write pulse (split into the two time bins) with the vibrational mode generates a two-mode squeezed state of the Stokes and vibrational fields (161) in each time bin. A read pulse delayed by  $\Delta t$  (also split into the two time bins) maps the vibrational state in the respective time bins onto its anti-Stokes sideband.

Since we perform the experiment in the regime of very low Stokes scattering probability and post-select the outcomes where exactly one Stokes photon and one anti-Stokes photon were detected (see SM for the treatment of triple coincidence), our scheme can be described in a subspace of the full Hilbert space that contains one vibrational excitation only, shared by the early and late time bin. We therefore introduce the shortened notation  $|E_v\rangle \equiv \hat{v}_E^\dagger |0_v\rangle$ ;  $|L_v\rangle \equiv \hat{v}_L^\dagger |0_v\rangle$  for the single phonon states (here  $\hat{v}^\dagger$  is the phonon creation operator), and  $|E_s\rangle \equiv \hat{s}_E^\dagger |0_s\rangle$ ;  $|L_s\rangle \equiv \hat{s}_L^\dagger |0_s\rangle$  for the Stokes single photon states (here  $\hat{s}^\dagger$  is the Stokes photon creation operator).

Conditioned on the detection of a single Stokes photon, the hybrid light–vibrational state can be written in the basis  $\{|E_s\rangle, |L_s\rangle\} \otimes \{|E_v\rangle, |L_v\rangle\} = \{|E_s\rangle \otimes |E_v\rangle, |E_s\rangle \otimes |L_v\rangle, |L_s\rangle \otimes |E_v\rangle, |L_s\rangle \otimes |L_v\rangle\}$ . In this sense, we can speak of vibrational and photonic qubits encoded in the time bin basis.

Within each time bin, the read pulse implements (with a small probability  $\sim 0.1\%$ ) the map  $|E_s, E_v\rangle \rightarrow |E_s, E_a\rangle$  and  $|L_s, L_v\rangle \rightarrow |L_s, L_a\rangle$ , where we have defined  $|E_a\rangle \equiv \hat{a}_E^\dagger |0_a\rangle$  and  $|L_a\rangle \equiv \hat{a}_L^\dagger |0_a\rangle$  (here  $\hat{a}_{E,L}^\dagger$  are the creation operators for the anti-Stokes photon in each time bin). Detection of an anti-Stokes photon in coincidence with a Stokes photon from the write pulse heralds that the time bin qubit was successfully mapped onto an anti-Stokes photonic qubit.

By passing the Stokes and anti-Stokes photons through an unbalanced interferometer identical to the one used on the excitation path (Fig. 7.1b, and SM), “which-time” information is erased. Moreover, the use of polarizing beam splitters in the interferometer maps the time-bin-encoded Stokes and anti-Stokes photonic qubits onto polarization-encoded qubits after they are temporally overlapped,  $|E_s, E_a\rangle \rightarrow |V_s, V_a\rangle$  and  $|L_s, L_a\rangle \rightarrow |H_s, H_a\rangle$  where  $H$  and  $V$  refer to two orthogonal polarizations of the same temporal mode. We thus prepare the heralded Bell correlated state

$$|\psi_{s,a}\rangle = \frac{1}{\sqrt{2}} \left( |V_s, V_a\rangle - e^{i\phi} |H_s, H_a\rangle \right) \quad (7.1)$$

where the phase  $\phi$  is the sum of the phases acquired by the Stokes and anti-Stokes photons coming from the late time bin, with respect to the early time bin (the apparatus is set to realize  $\phi = 0$ ). As detailed in Fig. S1, the experiment is passively phase-stable by design.

In order to prove Bell correlations mediated by the room-temperature macroscopic vibration, we send the Stokes and anti-Stokes signals to two independent measurement apparatus labelled Alice and Bob, respectively, who perform local rotations of the Stokes and anti-Stokes states before making a projective measurement in the two-dimensional basis  $\{|V_s\rangle, |H_s\rangle\}$  and  $\{|V_a\rangle, |H_a\rangle\}$ , respectively. Each party will obtain one of two outcomes, which we label “+” or “−”. The number of coincident events where Alice obtains the outcome  $x \in \{+, -\}$  and Bob obtains the outcome  $y \in \{+, -\}$  is denoted  $n_{xy}$ . We then define the normalized correlation parameter

$$E_{\theta,\varphi} = \frac{n_{++} + n_{--} - n_{+-} - n_{-+}}{n_{++} + n_{--} + n_{+-} + n_{-+}} \quad (7.2)$$

where the angles  $\theta$  and  $\varphi$  label the rotations that Alice and Bob respectively perform on their qubits before the measurement. It is defined in such a way that fully correlated events for a given pair of rotation angles  $\{\theta, \varphi\}$  yield  $E_{\theta,\varphi} = 1$  while perfectly anti-correlated events yield  $E_{\theta,\varphi} = -1$ . In fact the CHSH parameter (147),

$$S = E_{\theta_1, \varphi_1} + E_{\theta_2, \varphi_2} + E_{\theta_1, \varphi_2} - E_{\theta_2, \varphi_1} \quad (7.3)$$

certifies Bell correlations when  $|S| > 2$ . In particular, for our scenario, where we target the Bell correlated state eq. (7.1), a maximal violation is expected for  $\{\theta_1, \theta_2\} = \{0, \frac{\pi}{2}\}$  and  $\{\varphi_1, \varphi_2\} = \{-\frac{\pi}{4}, \frac{\pi}{4}\}$ .

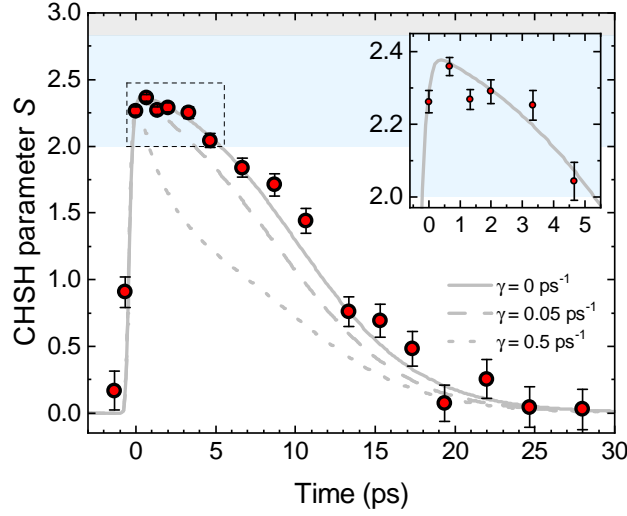


Figure 7.2: **Time-resolved photon-phonon Bell correlations.** The CHSH parameter  $S$  (eq. (7.3)) as a function of write – read delay  $\Delta t$ , with a zoom near  $\Delta t = 0$  as an inset. Full circles are experimental data, while error bars are computed from a Monte Carlo simulation (see SM, Section 2 for details). The solid gray line is obtained from the model with zero pure dephasing and no other free parameters, while dashed lines illustrate the impact of two different non-zero values. The blue region, demarcated by  $2 < |S| \leq 2\sqrt{2}$ , certifies Bell correlations, while the gray region above it is forbidden for non-superluminal theories.

## Results

### Observation of Bell correlations

Figure 7.2 shows the CHSH parameter (eq. (7.3)) measured for a varying write–read delay. Our data demonstrates a clear violation of the Bell inequality (whose classical bound is marked as the white region) which persists for more than 5 ps, about 50 times longer than the write and read pulse duration. While this timescale is consistent with the phonon lifetime in diamond, the dynamics of Bell correlations in fact strongly depends on experimental noise and non-idealities, as explained in SM, Sections 4-6.

At a time delay of 0.66 ps, for which there is vanishing temporal overlap of the write and read pulses within the sample and correlations are only mediated by the vibration, we measure  $S = 2.360 \pm 0.025$ . This confirms Bell correlations mediated by the vibration that acts as a room-temperature quantum memory (15; 16; 19; 20; 17).

A detailed analysis of the event statistics (see SM, Section 6) enables us to make a more precise claim concerning the violation of the Bell inequality (164), without assuming that our data is independent and identically distributed. From this analysis, we can claim with a confidence level of  $1 - 6 \times 10^{-7}$  that the post-selected Stokes – anti-Stokes state features Bell correlations

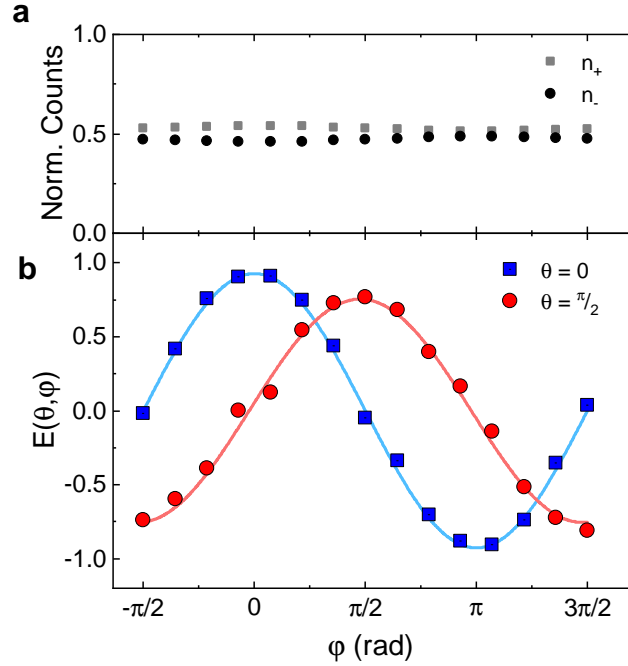


Figure 7.3: **Phonon-mediated two-photon interference.** **a**, Normalized single-photon count rates on the two anti-Stokes detectors as a function of Bob's rotation angle  $\varphi$ . The ideal marginal state is the statistical mixture  $p|E_a\rangle\langle E_a| + (1-p)|L_a\rangle\langle L_a|$ , with  $p = \frac{1}{2}$ ; data is consistent with  $|p - \frac{1}{2}| = 0.027$ . Error bars are several times smaller than symbol size. **b**, Two-photon interferences in the Stokes – anti-Stokes coincidence rate as a function of Bob's rotation angle  $\varphi$ . The normalized correlation parameter  $E(\theta, \varphi)$  (eq. 7.2) is plotted for two fixed angles  $\theta = 0$  (blue squares) and  $\theta = \pi/2$  (red circles) for Alice's rotation on the Stokes state, at a fixed write – read delay of  $\Delta t = 0.66$  ps. Experimental data are represented by full symbols (error bars are smaller than symbol size); solid lines are fitting curves to extract the visibility (see SM for details).

with a minimum value of the CHSH parameter  $S_{\min} = 2.23$ .

Note that we rely on the fair sampling assumption (165) since the overall detection efficiency in our experiment is not high enough to test a Bell inequality without post-selection of events where at least one detector clicks on each side (Alice and Bob). However, it can be shown (166) that when all detectors are equally efficient – a condition well approximated in our experiment – the post-selected data is faithful to that from an ideal experiment where lossless devices measure a state obtained by quantum filtering the actual Stokes – anti-Stokes state. By reporting a CHSH value higher than 2, we show that this filtered state is Bell-correlated.

To gain further insight into the nature of the Bell correlated state prepared in the experiment, and the reasons why the quantum bound ( $|S| = 2\sqrt{2}$ ) is not saturated, we perform further measurements. Figure 7.3a shows the one-photon counts as Bob's analysis angle is rotated. For an ideal Bell state, the marginal is maximally mixed, and should lead to no dependence of

the one-photon counts on the analysis angle. The observed data is consistent with a deviation from a maximal mixture by 2.7%.

Figure 7.3b shows two-photon interference for various settings of Bob's measurement angle for two fixed values of Alice's measurement angle,  $\theta = 0, \pi/2$ , and a fixed write-read delay of 0.66 ps. The interference is consistent with a model (see SM, Section 3) where the Stokes interaction creates a two-mode light-vibration squeezed state, and that anti-Stokes scattering implements a beam-splitter interaction (161).

The curve for the setting  $\theta = 0$  (Fig. 7.3b blue trace) reveals how accurately we can prepare and distinguish the two states  $|E_s, E_a\rangle$  and  $|L_s, L_a\rangle$ . At a given delay, the visibility has an upper limit related to the strength of Stokes – anti-Stokes photon number correlations,  $V_{\max} = \frac{g_{s,a}^{(2)} - 1}{g_{s,a}^{(2)} + 1}$  (162), where  $g_{s,a}^{(2)}$  is the normalized second-order cross-correlation (135) (see SM). The value extracted from the fit is  $V_{\theta=0} = 93 \pm 1\%$ , in agreement with the independently measured value of  $g_{s,a}^{(2)}(0) = 25$ , showing that the signal-to-noise ratio in the cross-correlation is indeed the limiting factor for the visibility in this setting. This visibility could be improved by reducing the power of the write beam (to decrease the probability of creating multiple Stokes-phonon pairs in one pulse) and that of the read beam (to reduce the noise from degenerate four-wave mixing). Note that due to the small interaction length ( $\sim 2 \mu\text{m}$ ), phase matching is not a relevant concern.

The coincidence curve for  $\theta = \frac{\pi}{2}$  (Fig. 7.3b red trace) corresponds to a rotated measurement basis for Alice and is sensitive to the fluctuations of the phase  $\phi$  in the superposition of eq. (7.1). To accomodate this possibility, we model the relative phase  $\phi$  in eq. (7.1) to be distributed as a zero-mean Gaussian random variable with variance  $\sigma$  (see SM). We extract a visibility  $V_{\theta=\pi/2} = 76\%$  from the fit to the experimental data, which is reproduced by the model for a standard deviation  $\sigma = 0.31$  rad (equivalent to a  $\pm 0.18$  fs timing uncertainty maintained over  $\sim 4$  minutes).

Ultimately, we are able to predict all measured quantities from independently characterised parameters, namely the Raman scattering probability, the overall Raman signal detection efficiency, and the dark count rate of the detectors (see SM, Section 4).

### Decoherence dynamics of the phonon mode

From the temporal behavior of the CHSH parameter we can extract the rate of pure dephasing of the vibrational mode mediating the Bell correlations. In the absence of pure dephasing, the CHSH parameter decays with the collective vibrational mode. Pure dephasing, in contrast, scrambles the phase  $\phi$  of the superposition in state (7.1). We model it as a random-walk of the phase at the characteristic time scale  $\gamma^{-1}$ , so that the standard deviation of the phase  $\phi$  increases with the write-read delay (in addition to technical fluctuations) as  $\sigma = \sqrt{\gamma \Delta t}$  (see SM, Section 3.6). The model is plotted against the data of Fig. 7.2 (solid line), and the best agreement with the data is obtained with a pure dephasing rate identically null (other pure

dephasing rates are plotted for comparison), consistent with previous measurements of the coherence time of a single vibrational mode in diamond using transient coherent ultrafast phonon spectroscopy (72).

## Discussion

For the first time, we have produced Bell correlations between two photons through their interaction with a common Raman-active phonon at room temperature, and probed their decay with sub-picosecond resolution. Remarkably, our data show that Bell correlations are preserved for more than 200 oscillation periods at room temperature, evidencing a mechanical coherence time in par with the state-of-the-art for microfabricated resonators under high vacuum (167). Optical phonons in diamond indeed exhibit a room temperature “Q-frequency product” of  $\sim 4 \times 10^{16}$  Hz, making them attractive resonators for ultrafast quantum technologies.

Such highly coherent vibrational modes, together with the toolset of time-resolved single photon Raman spectroscopy that we have demonstrated here, should allow to entangle two vibrational qubits via entanglement swapping (168), or to perform optomechanical conversion between photonic qubits at different frequencies (169), among other possible applications. Much longer vibrational coherence times could be achieved with ensembles of molecules that are decoupled from the phonon bath by surface engineering (170) or optical trapping and cooling (171). Besides, molecules in the gas phase exhibit more complex mechanical degrees of freedom, including rotational and rovibrational modes (172), with increased coherence time and rich opportunities for quantum information processing (173). In the future, our scheme could be applied to individual molecules free of heterogeneous broadening using the enhancement of light-vibration coupling offered by electronic resonances (174), plasmonic nanocavities (50) or optical microcavities (175)."

In addition to being a benchmark for the robust generation of optomechanical Bell correlations at room temperature, our work suggests a new class of techniques able to probe the role of phonon-mediated entanglement in quantum technologies (123), chemistry (176), or even biology (177).

## 7.2 Supplementary Information

### 7.2.1 Experimental Methods

#### Description of setup and experimental parameters

The full schematic of the experimental setup is shown in Fig. 7.4. We summarize the key experimental parameters in Table 7.1.

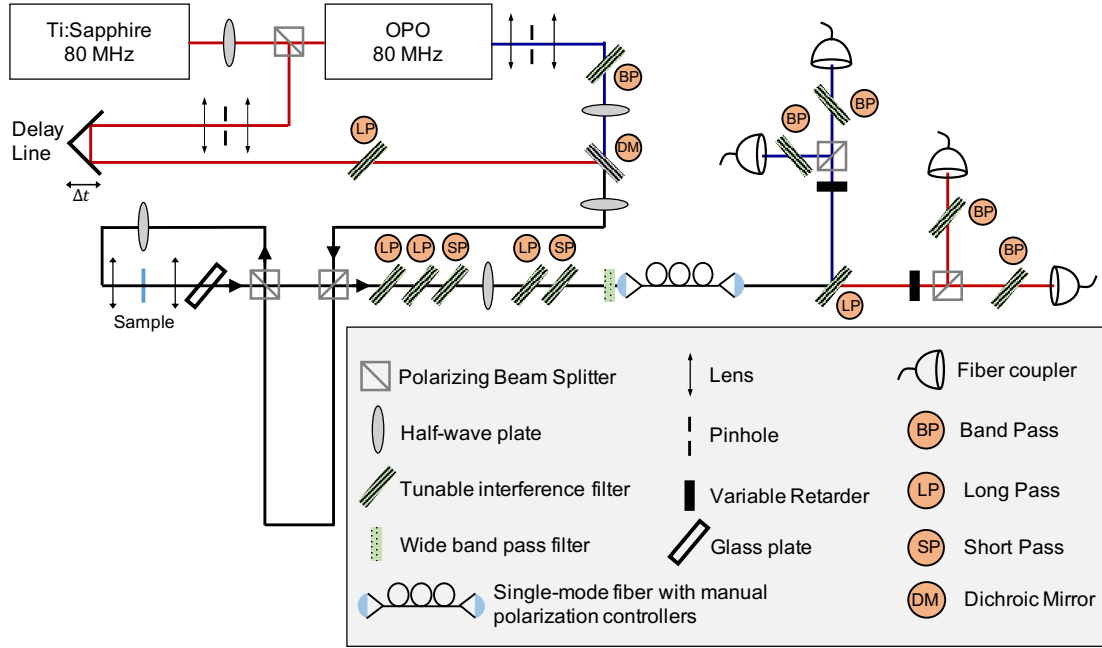


Figure 7.4: **Experimental Setup**

Parameter	Value
Repetition Rate	80.7 MHz
Write pulse wavelength	695 nm
Stokes wavelength	766 nm
Read pulse wavelength	800 nm
Anti-Stokes wavelength	723 nm
Write pulse energy	25 pJ
Read pulse energy	248 pJ
Total acquisition time per setting	4 min
Average Stokes countrate*	35700 s <sup>-1</sup>
Average anti-Stokes countrate*	1750 s <sup>-1</sup>
Stokes - anti-Stokes coincidence rate**	17 s <sup>-1</sup>

Table 7.1: Summary of relevant experimental parameters.

\* Calculated using the total countrate of + and – detectors in each detection arm.

• For a delay  $\Delta t = 0.66$  ps.

**Excitation pulses** A mode-locked Ti:Sapph laser and a synchronously pumped optical parametric oscillator are used to generate the read and write pulses, respectively. The pulse durations are about 100 fs and 200 fs for the Ti:Sapph and OPO, respectively. The experiment is repeated every 12.5 ns, set by the 80 MHz repetition rate of the laser system. The linear polarisation of the write and read pulses are first rotated by 45 degrees so that half of their intensity is directed toward the two arms of the unbalanced interferometer, which is constructed with polarising beam splitters. Light that is vertically polarized travels through the short path,



while horizontally polarized light travels through the long path. A half-wave plate rotates the polarisation of all pulses by 90 degrees after the interferometer, yielding the pulse distribution shown in Fig. 1b of the main text, where the layout was unfolded and modified for clarity. The delay between the two arms of the unbalanced interferometer is about 3 ns (approximately 1 m in free space), orders-of-magnitude longer than the phonon lifetime in the sample ( $\approx 4$  ps).

**Which-time information erasing** The time-bin entangled state is prepared by erasing temporal information about the Raman scattering processes. To do so, after the sample the Raman scattered photons are collected in transmission and passed through the same polarisation-selective unbalanced interferometer as the one used to create the two time bins in excitation, but they enter from another input port.

By suitably rotating the polarisation of the incoming pulses and of the Raman scattered photons, which are related by the symmetry of the vibrational mode under study, we can optimise the likelihood for the Raman photons to temporally overlap after the second interferometer. This is achieved when Raman scattered photons from the early time-bin are routed in the long arm, and vice-versa. Due to the linear polarisation of the Raman scattered fields in our geometry, this likelihood is close to unity (note that for diamond excited along the [100] crystal axis the Raman scattered photons are orthogonally polarised with respect to the pump).

In the worst-case scenario where Raman photons are unpolarised, half of them would take the wrong path and remain distinguishable in time. Accordingly, the likelihood to erase which-time information would drop to one fourth (25%); but the fidelity of the post-selected entangled state would not be affected. Indeed, as long as the time-bin separation is larger than the detector jitter, temporal filtering can be performed to exclude the distinguishable events from analysis. It is worth mentioning here that crystals and molecules with different symmetries may allow for the storage of polarisation-encoded vibrational qubits, therefore opening new experimental possibilities to probe photon-phonon entanglement [52].

Additionally, using the same physical interferometer twice - first to define the time bins in excitation and then to erase the temporal information carried by the Raman scattered photons - renders our entire setup passively phase-stable, as any fluctuation of the optical path between two arms occurring on a time scale longer than the travel time for light through the setup (which is a few tens of nanoseconds) is cancelled by construction (see detailed layout in SI). In this way, we are insensitive to all types of noise causing path fluctuations in a bandwidth of at least 10 MHz, which encompasses almost all mechanical and thermal instability.

**Impact of birefringence** Special care must be taken to avoid birefringence in the setup, as it would result in a temporal shift between the horizontal (H) and vertical (V) polarisations. Imperfect temporal overlap translates into a mixed state component as opposed to a pure entangled state (see Sec. 7.2.3). The short duration of the laser pulses means that the overlap must be preserved to well below 100 fs, and this must be the case for a relatively broad

wavelength range of several tens of nm.

Dichroic mirrors and tunable interference filters in particular have a strong birefringence when the incident angle is non zero. We mitigate the birefringence induced delay caused by the dichroic mirror that serves to overlap the write and read pulses on the same spatial mode by preparing both beams in the vertical polarisation, and then using an achromatic half wave plate to rotate the polarisation by 45 degrees before the imbalanced polarised interferometer.

Also, we must mitigate the deleterious effect of birefringence in the interference filters used to reject the write and read laser beams. For this, we use two identical sets (consisting each of a long pass filter to block the write pulse and a short filter to block the read pulse) and place an achromatic half wave plate between them. In this way, the Raman scattered light goes through the second sets of filters after its polarisation was rotated by 90 degrees, so that we ensure that both polarisations are equally delayed even in the presence of birefringence, and thus the temporal and spatial overlap is perfectly maintained.

**Time-bin to polarisation qubit mapping** Since we use polarising beam splitters to route the photons in the short and long path of the unbalanced interferometer, the polarisation is the only degree of freedom that distinguishes between the early and late time bin after the Stokes and anti-Stokes photons are temporally overlapped. More specifically, Raman photons originating from the early time are vertically polarised, and those from the late time bin are horizontally polarised.

**Detection** After the laser rejection filters, the Raman signal is spatially filtered by coupling it into a S630-HP single mode fiber (Thorlabs, FC/PC). Polarisation control paddles are used to maintain the same linear polarisation before and after the fiber. The signal is collimated after the fiber and sent onto a tunable long pass filter, where the Stokes field is transmitted and the anti-Stokes field is reflected, after which the two fields enter the two detection apparatuses labelled 'Alice' and 'Bob', respectively. The birefringence introduced by this filter - especially for the reflected beam, which has a very strong wavelength and angle dependence - cannot be easily compensated, and we attribute the main loss of visibility to this element.

At each locations we first use a variable retarder (VR), whose fast axis is rotated by 45 degrees with respect to the vertical, in order to perform the state rotation (see Sec. 7.2.3 for the mathematical formalism). Subsequently, a polarising beam splitter (PBS) directs the horizontal (H) and vertical (V) components of the incoming light onto two distinct single photon detectors, implementing thereby a projective measurement in the H/V basis, equivalent to the early/late basis for the time bin qubits. After these last PBS, birefringence no longer affects the experiment, and we send the output of each PBS through a tunable bandpass filter centered on the Stokes or anti-Stokes wavelengths, respectively. Finally, we couple each of the four output beams into a multi-mode fiber connected to an avalanche photo diode (APD) operated in Geiger mode, featuring about 50% detection efficiency and 500 ps timing jitter.

**Optimisation** Before running the experiment we check the two-photon correlations in the  $\{\theta = 0, \varphi = 0\}$  and  $\{\theta = \frac{\pi}{2}, \varphi = \frac{\pi}{2}\}$  configurations, where  $\theta$  (resp.  $\varphi$ ) is the state rotation angle (given by the retardation of the variable retarder) chosen by Alice (resp. Bob). Under ideal conditions we would expect  $E(0, 0) = E(\frac{\pi}{2}, \frac{\pi}{2})$ , but we always measure  $E(0, 0) > E(\frac{\pi}{2}, \frac{\pi}{2})$  due to either imperfect alignment or birefringence that was not properly compensated for (see mathematical explanation in Sec. 7.2.3). As a final step we slightly change the angle of the first long pass filter after the interferometer to maximize the value of  $E(\frac{\pi}{2}, \frac{\pi}{2})$ .

### Calibration of the Variable Retarders

The liquid crystal variable retarders (VR) (from ARCoOptix) allow us to apply a voltage-dependent delay along one polarisation axis. This axis is set to 45 deg, allowing us to rotate the polarisation state of each photon in a plane containing the vertical and horizontal states (see Sec. 7.2.3).

To avoid any artefact due to the wavelength dependence of the retardation, the calibration of the VRs at Alice and Bob's locations is done with the Stokes or anti-Stokes signals, respectively, by sending vertically polarised light through the VR and measuring the amount of vertically and horizontally polarised light afterwards using a PBS and two detectors. The phase shift is then  $\delta = \arccos(2T - 1)$ , where  $T$  is the normalized count rate in the vertical polarisation detector. Results of this procedure are shown in Fig. 7.5.

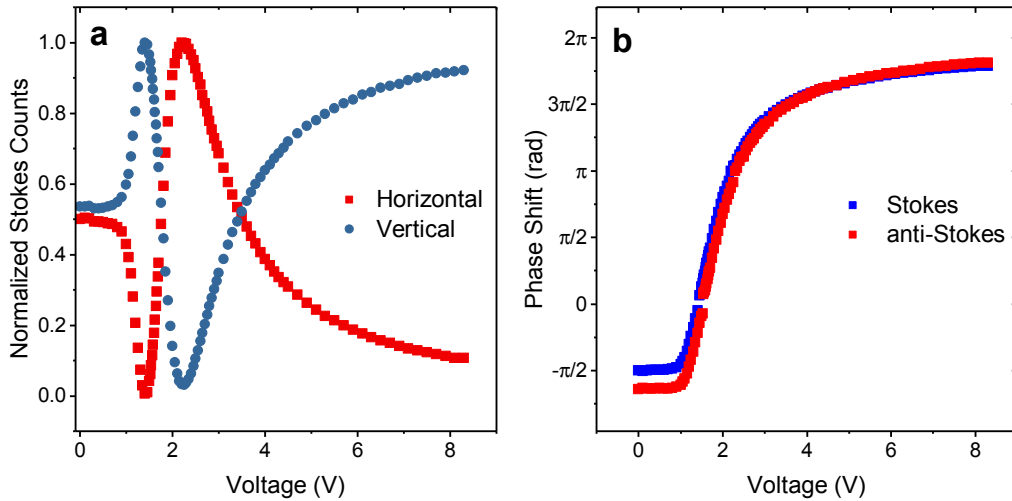


Figure 7.5: **Calibration of variable retarders** **a**, Normalized count rates on the detectors measuring the vertical and horizontal components of the light after the VR, when vertically polarised light is sent into the VR. Data for the Stokes channel only are shown. **b**, Extracted voltage-dependent phase shifts for the Stokes and anti-Stokes wavelengths.

### 7.2.2 Data Acquisition Methods

#### Data Acquisition

We record the detection events using a custom time-tagging card developed by the Digital Electronics Laboratory at Politecnico di Milano (Prof. Angelo Geraci) with four input channels plus a sync channel. Using the sync signal from the mode-locked laser oscillator as a time reference, we define a detection time window that only records photons originating from the early time bin and taking the long path in the second interferometer, or vice versa (from late time bin taking the short path). We discard all other events. Over the acquisition time, we record the number of single detection events from each detector occurring in the detection window, as well as the number of times multiple detectors clicked during the same window. The number of coincidences between the detectors of Alice and Bob correspond to the  $n_{\pm,\pm}$  terms used to calculate  $E$ . We obtain the two-photon interference curves of Fig. 2 (main text) at a fixed write-read delay by setting  $\theta = 0$  or  $(\theta = \frac{\pi}{2})$  and sweeping  $\varphi$ .

We ran the Bell tests with the phase setting  $\{\theta, \varphi\}$  in the following order:  $\{0, \frac{\pi}{4}\}, \{0, -\frac{\pi}{4}\}, \{\frac{\pi}{2}, \frac{\pi}{4}\}, \{\frac{\pi}{2}, -\frac{\pi}{4}\}$ . We measure for 1 minute at each phase setting before changing the delay between write and read pulses, which is moved from negative to positive delay. In order to mitigate systematic errors (drifts in alignment, for example), we repeat the whole measurement sequence four times, for a total of four minutes per measurement setting at each delay setting. For the analysis all the counts of the four measurements with the same setting are added together, and used to compute  $E$  and  $S$  as explained in the main text.

The value of  $g_{s,a}^{(2)}(\Delta t)$  is calculated as

$$g_{s,a}^{(2)} = \frac{P(s \cap a)}{P(s)P(a)} = \frac{n_{s \cap a} \cdot R}{n_s \cdot n_a} \quad (7.4)$$

where  $R$  is the number of times the experiment was run (the repetition rate of the laser system times the acquisition time),  $n_s$  is the total number of Stokes photons detected (in the appropriate time window),  $n_a$  is the total number of anti-Stokes photons detected, and  $n_{s \cap a}$  is the total number of coincidences between Stokes and anti-Stokes photons, i.e.  $n_{(s \cap a)} = n_{++} + n_{+-} + n_{-+} + n_{--}$ .

#### Error Bars

The error bars displayed on all experimental plots for the normalised correlation parameter  $E$  and CHSH parameter  $S$  are calculated using a Monte Carlo approach. For each measurement we model the probability of each coincidence count  $n_{xx}$  as a Poissonian distribution centered on  $n_{xx}$ . We then pick a random number from each distribution using the Python library NumPy, and use it to calculate  $S$  (resp.  $E$ ) for the Bell measurement (resp. visibility measurement). We repeat this process many times in order to obtain a collection of values for  $S$  (resp.  $E$ ), and we take the standard deviation of this distribution to be a faithful estimate for

the statistical uncertainty of the measurement.

To ensure convergence of the procedure, after each iteration described above, we compare the average and standard deviation of the accumulated values to the results from the previous step. We keep repeating this process until the relative difference between two successive steps is below  $10^{-5}$  for both the average and standard deviation.

### 7.2.3 Theoretical Methods

In this section we explain how we model the experiment in order to obtain the fitting function for the CHSH parameter plotted in Fig. 2 of the main text. We start from the assumptions that i) the photon-phonon state is described by a two-mode squeezed state with phase noise and ii) measurements are done with noisy, non-unit efficiency, non-photon number resolving detectors. We use independent measurements of the squeezing parameter, dark count rates and efficiencies to show that both the result of the cross-correlation measurement and the non-local interference pattern for  $\theta = 0$  are consistent with these assumptions. We then use the phase sensitive non-local interference pattern obtained for  $\theta = \pi/2$  to evaluate the amount of phase noise. The assumption on the state and the measurements together with the knowledge of the phase noise allows us to predict the time dependence of the CHSH parameter and the effect of pure dephasing on its decay.

### 7.2.4 Modelling of the source and detection devices

#### Source

We consider a source generating Stokes–anti-Stokes photon pairs according to

$$|\psi_t\rangle = (1 - \text{Th}_g^2)^{\frac{1}{2}} (1 - \text{Th}_{\bar{g}}^2)^{\frac{1}{2}} e^{\text{Th}_g s^\dagger a^\dagger - \text{Th}_{\bar{g}} s_\perp^\dagger a_\perp^\dagger} |0\rangle \quad (7.5)$$

where  $|0\rangle$  denotes the vacuum for all modes;  $s$  and  $s_\perp$  are bosonic operators corresponding to the two orthogonal modes received by Alice and similarly for Bob. In our experiment, these orthogonal modes correspond to the two time bins, which are subsequently converted into orthogonal photon polarisations. We have used the short notation  $\text{Th}_g = \tanh(g)$  where  $g$  is the squeezing parameter, is related to the mean photon number in mode  $s$  by  $\langle\psi_t|s^\dagger s|\psi_t\rangle = (\sinh g)^2 = (\text{Sh}_g)^2$ . In the rest of the text, we also use  $\text{Ch}_g = \cosh g$ . We specifically consider the symmetric case where  $g = \bar{g}$ .

#### Detector

We consider photon detectors which do not resolve the photon number. They have an efficiency  $\eta$  (overall detection efficiency including all losses from the source to the detector) and a dark count probability  $p_{dc}$ . A “click” event (electric pulse generated by the detector) is then

modelled by the POVM [53]

$$\hat{D}_s(\eta_s) = 1 - (1 - p_{dc})(1 - \eta_s)^{s^\dagger s} \quad (7.6)$$

The subscript (here  $s$ ) specifies the mode which is detected. The dark count probability  $p_{dc}$  is the same for all modes and detectors. To illustrate the validity of the model, consider the Fock state  $|n\rangle$ . The probability to get a click is  $\langle n | \hat{D}_s(\eta_s) | n \rangle = 1 - (1 - p_{dc})(1 - \eta_s)^n$  which equals one minus the probability to lose all the  $n$  photons and to get no dark count.

### Choice of measurement settings

Rotations are possibly performed during detection so that the photons can be measured in several basis. The detected modes are called  $A$  and  $A_\perp$  for Alice ( $B$  and  $B_\perp$  for Bob) and are related to the emission modes by

$$s = C_\alpha A + S_\alpha e^{i\phi_s} A_\perp \quad (7.7)$$

$$s_\perp = S_\alpha e^{-i\phi_s} A + C_\alpha A_\perp \quad (7.8)$$

with  $C_\alpha = \cos(\alpha)$  and  $S_\alpha = \sin(\alpha)$  and similarly for Bob.

Note that the angles  $\alpha, \beta$  are related to the optical phases introduced by the variable retarders in the experiment by  $\theta = 2\alpha$  and  $\varphi = 2\beta$ . To see why, consider for example the rotation of polarisation by  $90^\circ$  from vertical to horizontal. In this formalism, this corresponds to a rotation angle  $\alpha = \pi/2$ . Experimentally, however, this requires introducing a  $\theta = \pi$  phase shift in the variable retarder (whose axis, we recall, is oriented at  $45^\circ$  w.r.t horizontal and vertical).

### Phase noise

Consider a mechanism adding a phase which is different for each SPDC process, that is, at a given run the state can be written as

$$|\psi_t^\phi\rangle = (1 - \text{Th}_g^2) e^{\text{Th}_g(e^{-i\phi/2} s^\dagger a^\dagger - e^{i\phi/2} s_\perp^\dagger a_\perp^\dagger)} |0\rangle \quad (7.9)$$

where  $\phi$  changes from run to run according to a Gaussian probability distribution  $p(\phi) = \frac{1}{\sigma\sqrt{2\pi}} e^{-\frac{\phi^2}{2\sigma^2}}$ . This state can be written as a unitary operation on  $|\psi_t\rangle$ ; i.e.  $|\psi_t^\phi\rangle = e^{i\phi/2(s^\dagger s - s_\perp^\dagger s_\perp)} |\psi_t\rangle$ . The unitary  $e^{i\phi/2(s^\dagger s - s_\perp^\dagger s_\perp)}$  shifts the azimuthal angle of a qubit state of the form  $(C_\alpha s^\dagger + e^{i\phi_s} S_\alpha s_\perp^\dagger) |0\rangle$  by  $\phi$ . When combining the unitary defining the setting choice and  $e^{i\phi/2(s^\dagger s - s_\perp^\dagger s_\perp)}$ , we get the following expression for the emission modes as a function of the detected modes

$$s = C_\alpha A + S_\alpha e^{i\phi_s + \phi} A_\perp \quad (7.10)$$

$$s_{\perp} = S_{\alpha} e^{-i\phi_s + \phi} A + C_{\alpha} A_{\perp} \quad (7.11)$$

and similarly for Bob.

### Summary

The state which is effectively measured can be written as

$$|\psi_{\alpha, \phi_s, \beta, \phi_a, \phi}\rangle = (1 - \tan(g)^2) e^{(A^{\dagger}, A_{\perp}^{\dagger}) M \begin{pmatrix} B^{\dagger} \\ B_{\perp}^{\dagger} \end{pmatrix}} |\underline{0}\rangle \quad (7.12)$$

with

$$M = \tan(g) \begin{pmatrix} C_{\alpha} S_{\beta} e^{-i(\phi_a - \phi)} - S_{\alpha} e^{-i(\phi_s + \phi)} C_{\beta} & -C_{\alpha} C_{\beta} - S_{\alpha} e^{i(\phi_s + \phi)} S_{\beta} e^{i(\phi_a - \phi)} \\ S_{\alpha} e^{i(\phi_s + \phi)} S_{\beta} e^{-i(\phi_a - \phi)} + C_{\alpha} C_{\beta} & -S_{\alpha} e^{i(\phi_s + \phi)} C_{\beta} + C_{\alpha} S_{\beta} e^{i(\phi_a - \phi)} \end{pmatrix} \quad (7.13)$$

It is measured according to a model where the POVM element associated to a click in detector A is given by

$$\hat{D}_A(\eta_A) = 1 - (1 - p_{dc})(1 - \eta_A)^{A^{\dagger} A} \quad (7.14)$$

and similarly for  $A_{\perp}$ ,  $B$ , and  $B_{\perp}$ . Given that  $\phi$  is random and changes from run to run, we derive the probabilities of various measurement outcomes that we then average according to  $p(\phi)$ .

### 7.2.5 Cross-Correlation Measurement

We consider the cross-correlation measurement where Alice and Bob choose the settings  $\alpha = \phi_s = 0$  and  $\beta = \phi_a = 0$  and measure

$$g_{s,a}^{(2)} = \frac{\langle \psi_0 | \hat{D}_A(\eta_A) \hat{D}_B(\eta_B) | \psi_0 \rangle}{\langle \psi_0 | \hat{D}_A(\eta_A) | \psi_0 \rangle \langle \psi_0 | \hat{D}_B(\eta_B) | \psi_0 \rangle} \quad (7.15)$$

where  $|\psi_0\rangle = |\psi_{0,0,0,0,\phi}\rangle$ . A straightforward calculation (along the same lines as [53] gives the following explicit expression

$$g_{s,a}^{(2)} = \frac{1 - (1 - p_{dc}) \frac{1 - \text{Th}_g^2}{1 - \text{Th}_g^2(1 - \eta_A)} - (1 - p_{dc}) \frac{1 - \text{Th}_g^2}{1 - \text{Th}_g^2(1 - \eta_B)} + (1 - p_{dc})^2 \frac{1 - \text{Th}_g^2}{1 - \text{Th}_g^2(1 - \eta_A)(1 - \eta_B)}}{\left(1 - (1 - p_{dc}) \frac{1 - \text{Th}_g^2}{1 - \text{Th}_g^2(1 - \eta_A)}\right) \left(1 - (1 - p_{dc}) \frac{1 - \text{Th}_g^2}{1 - \text{Th}_g^2(1 - \eta_B)}\right)} \quad (7.16)$$

From our experimental data, we can extract the following approximate values, as explained in Sec. 7.2.10,  $\text{Th}_g^2 = 0.0022$  i.e.  $g = 0.047$ ,  $\eta_A = 0.1$ ,  $\eta_B = 2.54 \times 10^{-4}$  (this includes the readout efficiency, i.e. anti-Stokes scattering probability knowing that a phonon was created) and

$p_{dc} = 9 \times 10^{-6}$  (probability of dark counts per detection window), with which we get  $g_{s,a}^{(2)} = 26.5$ , in good agreement with the measured normalised coincidence. In this model, the decoherence of the collective molecular vibration within one mode at rate  $\gamma_1$  manifests as an exponential decay of the vibration  $\rightarrow$  anti-Stokes conversion efficiency contained in  $\eta_B$ .

### 7.2.6 The Interference Pattern for $\alpha = 0$

#### Twofold coincidence probability

We consider the interference experiment in which the twofold coincidences on  $A$  and  $B$  are recorded when Alice fixes her measurement setting in the  $s/s_\perp$  basis ( $\alpha = \phi_s = 0$ ) while Bob rotates it in the  $x$ - $z$  plane ( $\phi_a = 0$ ). This situation corresponds to the blue curve of Fig. 3b in the main text. We can find an explicit expression for these twofold coincidence probabilities

$$\langle \psi_{0,\beta} | \hat{D}_A(\eta_A) \hat{D}_B(\eta_B) | \psi_{0,\beta} \rangle = \frac{1}{N} \left( 1 - (1 - p_{dc}) \frac{1 - T_g^2}{1 - T_g^2(1 - \eta_A)} - (1 - p_{dc}) \frac{1 - T_g^2}{1 - T_g^2(1 - \eta_B)} \right. \\ \left. + (1 - p_{dc})^2 \frac{2}{Ch_g^4} \frac{1}{2 - (2 - \eta_A)(2 - \eta_B)Th_g^2 - \eta_A\eta_B C_{2\beta}Th_g^2 + 2(1 - \eta_A)(1 - \eta_B)Th_g^4} \right) \quad (7.17)$$

The normalization coefficient  $N$  accounts for the post-selection of events giving at least one click at each side, i.e.

$$N = 1 - p(nc_A \& nc_{A_\perp} | \alpha = \pi/4, \phi_s = 0, \phi) - p(nc_B \& nc_{B_\perp} | \beta, \phi_a = 0, \phi) \\ + p(nc_A \& nc_{A_\perp} \& nc_B \& nc_{B_\perp} | \alpha = \pi/4, \phi_s = 0, \phi_a = 0, \phi) \quad (7.18)$$

where

$$p(nc_A \& nc_{A_\perp} | \alpha, \phi_s, \phi) = (1 - p_{dc})^2 \left( \frac{1 - T_g^2}{1 - T_g^2(1 - \eta_A)} \right)^2 \quad (7.19)$$

$$p(nc_B \& nc_{B_\perp} | \beta, \phi_a, \phi) = (1 - p_{dc})^2 \left( \frac{1 - T_g^2}{1 - T_g^2(1 - \eta_B)} \right)^2 \quad (7.20)$$

$$p(nc_A \& nc_{A_\perp} \& nc_B \& nc_{B_\perp} | \alpha, \phi_s, \beta, \phi_a, \phi) = (1 - p_{dc})^4 \left( \frac{1 - T_g^2}{1 - T_g^2(1 - \eta_A)(1 - \eta_B)} \right)^2 \quad (7.21)$$

and the notation  $nc_A$  means “no click in mode  $A$ ”, etc.



### Visibility of the Interference Pattern for $\alpha = 0$

The visibility of the interference pattern is given by

$$V_0 = \frac{\max_{\beta} \langle \psi_{0,\beta} | \hat{D}_A(\eta_A) \hat{D}_B(\eta_B) | \psi_{0,\beta} \rangle - \min_{\beta} \langle \psi_{0,\beta} | \hat{D}_A(\eta_A) \hat{D}_B(\eta_B) | \psi_{0,\beta} \rangle}{\max_{\beta} \langle \psi_{0,\beta} | \hat{D}_A(\eta_A) \hat{D}_B(\eta_B) | \psi_{0,\beta} \rangle + \min_{\beta} \langle \psi_{0,\beta} | \hat{D}_A(\eta_A) \hat{D}_B(\eta_B) | \psi_{0,\beta} \rangle} \quad (7.22)$$

Given the structure of (7.12), it is clear that  $\langle \psi_{0,\beta} | \hat{D}_A(\eta_A) \hat{D}_B(\eta_B) | \psi_{0,\beta} \rangle$  is maximized for  $\beta = 0$  and minimized for  $\beta = \pi/2$ . Using the same experimental parameters as above, i.e.  $\text{Th}_g^2 = 0.0022$  i.e.  $g = 0.047$ ,  $\eta_A = 0.1$ ,  $\eta_B = 2.54 \times 10^{-4}$  and  $p_{dc} = 9 \times 10^{-6}$ , we get  $V_0 \approx 0.92$ , in good agreement with the data of Fig. 3b (blue curve) in the main text.

### Visibility of the Interference Pattern for $\alpha = 0$ and Cross-Correlation Measurement

Note that

$$|\psi_{0,\pi/2}\rangle = (1 - \text{Th}_g^2) e^{\text{Th}_g^2(A^\dagger B^\dagger e^{-i\phi/2} - A_\perp^\dagger B_\perp^\dagger e^{i\phi/2})} |0\rangle = \underbrace{(1 - \text{Th}_g^2)^{1/2} e^{\text{Th}_g^2(A^\dagger B^\dagger e^{-i\phi/2})} |0\rangle}_{|\psi_{AB}^{-\phi}\rangle} \otimes \underbrace{(1 - \text{Th}_g^2)^{1/2} e^{-\text{Th}_g^2(A_\perp^\dagger B_\perp^\dagger e^{i\phi/2})} |0\rangle}_{|\bar{\psi}_{A_\perp B_\perp}^{+\phi}\rangle} \quad (7.23)$$

implying

$$\langle \psi_{0,\pi/2} | \hat{D}_A(\eta_A) \hat{D}_{B_\perp}(\eta_{B_\perp}) | \psi_{0,\pi/2} \rangle = \langle \psi_{AB}^{-\phi} | \hat{D}_A(\eta_A) | \psi_{AB}^{-\phi} \rangle \langle \bar{\psi}_{A_\perp B_\perp}^{+\phi} | \hat{D}_{B_\perp}(\eta_{B_\perp}) | \bar{\psi}_{A_\perp B_\perp}^{+\phi} \rangle \quad (7.24)$$

Similarly, we have

$$|\psi_0\rangle = |\bar{\psi}_{AB_\perp}^{-\phi}\rangle \otimes |\psi_{A_\perp B}^{+\phi}\rangle \quad (7.25)$$

We thus have

$$\begin{aligned} \langle \psi_{AB}^{-\phi} | \hat{D}_A(\eta_A) | \psi_{AB}^{-\phi} \rangle &= \text{Tr}_{AB}(D_A(\eta_A) | \psi_{AB}^{-\phi} \rangle \langle \psi_{AB}^{-\phi} |) \\ &= \text{Tr}_A(D_A(\eta_A) \text{Tr}_B(| \psi_{AB}^{-\phi} \rangle \langle \psi_{AB}^{-\phi} |)) \\ &= \text{Tr}_A(D_A(\eta_A) \text{Tr}_B(| \bar{\psi}_{AB_\perp}^{-\phi} \rangle \langle \bar{\psi}_{AB_\perp}^{-\phi} |)) \\ &= \langle \bar{\psi}_{AB_\perp}^{-\phi} | \hat{D}_A(\eta_A) | \bar{\psi}_{AB_\perp}^{-\phi} \rangle \\ &= \langle \psi_0 | \hat{D}_A(\eta_A) | \psi_0 \rangle \end{aligned} \quad (7.26)$$

and similarly

$$\langle \bar{\psi}_{AB}^{+\phi} | \hat{D}_{B_\perp}(\eta_{B_\perp}) | \bar{\psi}_{AB}^{+\phi} \rangle = \langle \psi_0 | \hat{D}_{B_\perp}(\eta_{B_\perp}) | \psi_0 \rangle \quad (7.27)$$

From the previous equalities, we deduce

$$\langle \psi_{0,\pi/2} | \hat{D}_A(\eta_A) \hat{D}_{B_\perp}(\eta_{B_\perp}) | \psi_{0,\pi/2} \rangle = \langle \psi_0 | \hat{D}_A(\eta_A) | \psi_0 \rangle \langle \psi_0 | \hat{D}_{B_\perp}(\eta_{B_\perp}) | \psi_0 \rangle \quad (7.28)$$

and consequently

$$V_0 = \frac{g_{s,a}^{(2)} - 1}{g_{s,a}^{(2)} + 1} \quad (7.29)$$

The previous formula holds for any efficiency. In particular, the temporal evolution of the visibility can be predicted from the evolution of  $g_{s,a}^{(2)}$  and is thus ultimately limited by the decay of each single collective vibrational mode.

### 7.2.7 Interference Pattern for $\alpha = \pi/4$

We now consider the interference experiment in which the twofold coincidences on  $A$  and  $B_\perp$  are recorded when Alice fixes her setting to  $(\alpha = \pi/4, \phi_s = 0)$  while Bob rotates it in the  $x$ - $z$  plane ( $\phi_a = 0$ ), which corresponds to the red curve in Fig. 3b of the main text. This interference is sensitive to fluctuations in the phase of the superposition  $\phi$  and thus allows to estimate its uncertainty. For fixed  $\phi$ , we have

$$\begin{aligned} \langle \psi_{\pi/4,0,\beta} | \hat{D}_A(\eta_A) \hat{D}_B(\eta_B) | \psi_{\pi/4,0,\beta} \rangle &= \frac{1}{N} \left( 1 - (1 - p_{dc}) \frac{1 - T_g^2}{1 - T_g^2(1 - \eta_A)} - (1 - p_{dc}) \frac{1 - T_g^2}{1 - T_g^2(1 - \eta_B)} \right. \\ &\quad \left. + (1 - p_{dc})^2 \frac{2}{\text{Ch}_g^4} \frac{1}{2 - (2 - \eta_A)(2 - \eta_B)\text{Th}_g^2 - \eta_A \eta_B C_{2\phi} S_{2\beta} \text{Th}_g^2 + 2(1 - \eta_A)(1 - \eta_B)\text{Th}_g^4} \right) \end{aligned} \quad (7.30)$$

where the normalisation coefficient is given before. To take into account the uncertainty in  $\phi$ , we can first use a Taylor expansion of the term in Eq. 7.30

$$\int d\phi p(\phi) (1 - p_{dc})^2 \frac{2}{\text{Ch}_g^4} \times \frac{1}{\zeta - \xi(C_{2\phi-1})} \approx (1 - p_{dc})^2 \frac{2}{\text{Ch}_g^4} \times \left( \frac{1}{\zeta} - \frac{2\xi}{\zeta^2} \sigma^2 + O(\sigma^3) \right) \quad (7.31)$$

where we introduced  $\zeta = 2 - (2 - \eta_A)(2 - \eta_B)\text{Th}_g^2 - \eta_A \eta_B S_{2\beta} \text{Th}_g^2 + 2(1 - \eta_A)(1 - \eta_B)\text{Th}_g^4$  and  $\xi = \eta_A \eta_B S_{2\beta} \text{Th}_g^2$ . The visibility of the interference pattern is given by

$$V_{\pi/4} = \frac{\max_{\beta} \langle \psi_{\pi/4,0,\beta} | \hat{D}_A(\eta_A) \hat{D}_{B\perp}(\eta_{B\perp}) | \psi_{\pi/4,0,\beta} \rangle - \min_{\beta} \langle \psi_{\pi/4,0,\beta} | \hat{D}_A(\eta_A) \hat{D}_{B\perp}(\eta_{B\perp}) | \psi_{\pi/4,0,\beta} \rangle}{\max_{\beta} \langle \psi_{\pi/4,0,\beta} | \hat{D}_A(\eta_A) \hat{D}_{B\perp}(\eta_{B\perp}) | \psi_{\pi/4,0,\beta} \rangle + \min_{\beta} \langle \psi_{\pi/4,0,\beta} | \hat{D}_A(\eta_A) \hat{D}_{B\perp}(\eta_{B\perp}) | \psi_{\pi/4,0,\beta} \rangle} \quad (7.32)$$

Given the structure of the state 7.12, it is clear that  $\langle \psi_{\pi/4,0,\beta} | \hat{D}_A(\eta_A) \hat{D}_{B\perp}(\eta_{B\perp}) | \psi_{\pi/4,0,\beta} \rangle$  is maximized for  $\beta = \pi/4$  and minimized for  $\beta = 3\pi/4$ . Using again the same experimental parameter, i.e.  $\text{Th}_g^2 = 0.0022$  i.e.  $g = 0.047$ ,  $\eta_A = 0.1$ ,  $\eta_B = 2.54 \times 10^{-4}$  and  $p_{dc} = 9 \times 10^{-6}$ , we can reproduce the visibility  $V_{\pi/4} \approx 0.76$  obtained in Fig. 3b of the main text (red curve) for a width of the phase distribution  $\sigma = 0.31$ .

### 7.2.8 CHSH Value from the Interference Patterns

Note that the correlation functions used to compute the CHSH value are given by

$$E(\alpha, \beta) = p(+1 + 1|\alpha\beta) + p(-1 - 1|\alpha\beta) - p(+1 - 1|\alpha\beta) - p(-1 + 1|\alpha\beta) \quad (7.33)$$

The normalization implies  $p(+1 - 1|\alpha\beta) + p(-1 + 1|\alpha\beta) = 1 - p(+1 + 1|\alpha\beta) - p(-1 - 1|\alpha\beta)$  and since  $p(-1 - 1|\alpha\beta) = 1 - p(+1|\alpha) - p(+1|\beta) + p(+1 + 1|\alpha\beta)$ , we find

$$E(\alpha, \beta) = 1 - 2p(+1|\alpha) - 2p(+1|\beta) + 4p(+1 + 1|\alpha\beta) \quad (7.34)$$

When we record more than 2 clicks in one repetition of the experiment, we choose to bin the results according to the following rule: When detector  $A$  clicks, Alice says that she gets  $+1$  independently of the event on detector  $A_\perp$ . Similarly, when Bob gets a click on detector  $B_\perp$ , he says that he gets  $+1$  independently of the event on detector  $B$ . This means that  $p(+1 + 1|\alpha\beta) = \langle \psi_{\alpha,0,\beta} | \hat{D}_A(\eta_A) \hat{D}_{B\perp}(\eta_{B\perp}) | \psi_{\alpha,0,\beta} \rangle$  while  $p(+1|\alpha) = \langle \psi_{\alpha,0,\beta} | \hat{D}_A(\eta_A) | \psi_{\alpha,0,\beta} \rangle$  and  $p(+1|\beta) = \langle \psi_{\alpha,0,\beta} | \hat{D}_{B\perp}(\eta_{B\perp}) | \psi_{\alpha,0,\beta} \rangle$ . Given that we post-select the cases where at least one click is obtained at each side, we have

$$E(\alpha, \beta) = 1 - \frac{2}{N_A} \langle \psi_{\alpha,0,\beta} | \hat{D}_A(\eta_A) | \psi_{\alpha,0,\beta} \rangle - \frac{2}{N_B} \langle \psi_{\alpha,0,\beta} | \hat{D}_{B\perp}(\eta_{B\perp}) | \psi_{\alpha,0,\beta} \rangle + \frac{4}{N} \langle \psi_{\alpha,0,\beta} | \hat{D}_A(\eta_A) \hat{D}_{B\perp}(\eta_{B\perp}) | \psi_{\alpha,0,\beta} \rangle \quad (7.35)$$

with  $N_A = 1 - p(nc_A \& nc_{A\perp} | \alpha, \phi_s, \phi)$  and  $N_B = 1 - p(nc_B \& nc_{B\perp} | \beta, \phi_a, \phi)$ . Considering the angles maximizing the CHSH value for the singlet, we have

$$\text{CHSH} = E(0, \pi/8) + E(0, -\pi/8) + E(\pi/4, \pi/8) - E(\pi/4, -\pi/8) \quad (7.36)$$

With the experimental parameters  $\text{Th}_g^2 = 0.0022$  i.e.  $g = 0.047$ ,  $\eta_A = 0.1$ ,  $\eta_B = 2.54 \times 10^{-4}$  and  $p_{dc} = 9 \times 10^{-6}$  and the phase uncertainty extracted above  $\sigma = 0.31$ , we find  $\text{CHSH} \approx 2.36$ , in good agreement with the value measured close to zero delay (cf. Fig. 2 in the main text).

### 7.2.9 Inferring Phonon Coherence Time from the CHSH Value

For the parameters of interest and in agreement with the measurement results, we checked that single photons are unpolarised on each side, meaning that the marginal probabilities of single photon detection are uniformly and randomly distributed onto the two detectors, whatever the measurement angle. This is shown in Fig. 3a of the main text. This means that the correlation functions only depends on the twofold coincidence probability

$$E(\alpha, \beta) = \frac{4}{N} \langle \psi_{\alpha,0,\beta} | \hat{D}_A(\eta_A) \hat{D}_{B\perp}(\eta_{B\perp}) | \psi_{\alpha,0,\beta} \rangle - 1 \quad (7.37)$$

Pure dephasing of the phononic qubit introduces a phase term  $\bar{\phi}$  in the state similar to  $\phi$  in Eq. 7.9. This phase is different at each run and is distributed according to

$$p(\bar{\phi}) = \frac{1}{\sqrt{2\pi}} \bar{\sigma} e^{-\bar{\phi}^2/2\bar{\sigma}^2} \quad (7.38)$$

where the standard deviation  $\bar{\sigma} = \sqrt{\gamma \Delta t}$  depends on both the dephasing rate  $\gamma$  and the time duration  $\Delta t$ . From the previous analysis, we know that  $\langle \psi_{0,0,\beta} | \hat{D}_A(\eta_A) \hat{D}_{B\perp}(\eta_{B\perp}) | \psi_{0,0,\beta} \rangle$  is independent of  $\bar{\phi}$  and hence  $E(0, \beta)$  is independent of dephasing effects. From the previous perturbative approach, we also find that  $\langle \psi_{\pi/4,0,\pm\pi/8} | \hat{D}_A(\eta_A) \hat{D}_{B\perp}(\eta_{B\perp}) | \psi_{\pi/4,0,\pm\pi/8} \rangle$  decays like  $e^{-2\bar{\sigma}^2}$ . Given that  $E(0, \pi/8) + E(0, -\pi/8)$  and  $E(\pi/4, \pi/8) + E(\pi/4, -\pi/8)$  equally contribute to the CHSH value in the absence of phase noise, we have

$$CHSH(\Delta t) = \frac{CHSH}{2} (1 + e^{-2\gamma \Delta t}) \quad (7.39)$$

The previous formula allows us to infer the coherence time  $\gamma^{-1}$  for the behavior of the CHSH parameter. Note that the prefactor CHSH is not constant in time since the detection efficiency of mode  $B$  includes the phononic lifetime.

### 7.2.10 Estimating experimental parameters

- **Stokes detection efficiency  $\eta_A$**  The detection efficiency is the product of the avalanche photodiode efficiency, for which we use the value of 50% from the manufacturer's test sheet, and the signal collection efficiency. Since our measurement is sensitive only to the spatial mode coupled into the single mode fiber used as a spatial filter, it is not necessary to consider the full spontaneous emission pattern in free space. Only the image of the single mode fiber into the sample is relevant to estimate the collection efficiency. This collection efficiency is therefore simply measured with the laser beam, which is well mode matched to the collection fiber, by measuring the power first just after the sample and second just before the detector. The additional loss due to internal reflection inside the diamond is estimated separately. This procedure yields  $\eta_A \approx 0.1$  for the Stokes signal.
- **Squeezing parameter  $g$**  This detection efficiency, together with the measured count rate in detector  $A$  of 18000 counts/s, and the repetition rate of 80 MHz, lets us estimate the average photon number  $\langle n_A \rangle = 2.25 \times 10^{-3}$  in the Stokes mode. We then use the expression of  $\langle n_A \rangle$  to find the squeezing parameter  $g = 0.047$ .
- **Dark count probability  $p_{dc}$**  In the model, the dark count probability accounts not only for the intrinsic noise in the detectors (which has negligible impact on our measurements) but also, and foremost, for the anti-Stokes emission due to thermal phonons. Based on the anti-Stokes count rate at negative delays ( $\sim 720c/s$ ) and the detection time window we estimate the dark count rate:  $p_{dc} = 9 \times 10^{-6}$ .

- **Vibration detection efficiency  $\eta_B$**  The detection efficiency of the vibrational mode  $\eta_B$  accounts for both the probability of converting an existing vibration into anti-Stokes photon as well as the collection and detection losses for the anti-Stokes photon. We can extract it directly from our measurement by comparing the probability of detecting a Stokes photon,  $P(A) = \langle n_A \rangle \eta_A$ , to the probability of a coincidence  $P(A \cap B) = \langle n_A \rangle \eta_A \eta_B$ . With our coincidence rate of 4.58 counts/s we obtain  $\eta_B = \frac{P(A \cap B)}{P(A)} = 2.54 \times 10^{-4}$ .

### 7.2.11 Extracting the rate of pure dephasing

We fit the measured  $g_{s,a}^{(2)}(\Delta t)$  using a single exponential decay with time constant  $\tau = 3.78$  ps, convoluted with the instrument response function (Gaussian of width 200 fs).

We then use eq. (7.39) to produce the expected curve for  $S(\Delta t)$ , using the fit of  $g_{s,a}^{(2)}(\Delta t)$  for the temporal behaviour of  $\eta_B$ .

The rate of pure dephasing is an adjustable, a priori unknown parameter. In Fig. 7.6, we compare the measured CHSH parameter with the formula eq. 7.39 for various different dephasing rates ( $\gamma$ ). The best agreement with the experimental data is found for  $\gamma \ll \tau^{-1}$ , consistent with a lifetime-limited coherence time.

### 7.2.12 Evolution of the CHSH parameter under ideal conditions

We would like to address the following questions: if all technical noise could be eliminated from the photo-detection, including all background emission from the sample not related to vibrational Raman scattering, what would be the intrinsic dynamics how Bell parameter? For how long would Bell correlations persist?

To answer these questions, we compute the temporal evolution of the Bell parameter using the theoretical model with idealized measurement, and with the experimentally determined vibrational energy decay rate, assuming the pure dephasing rate is much smaller and can be neglected. More explicitly, we use the following parameters:

- **Stokes detection efficiency  $\eta_A$**  We set the Stokes detection efficiency to unity.
- **Vibration detection efficiency  $\eta_B$**  We set the initial value of the detection efficiency to unity, which then decays with the measured time constant corresponding to the phonon lifetime  $\tau = 3.78$  ps.
- **Dark count probability  $p_{dc}$**  We only include the anti-Stokes emission due to thermal phonons, which in the case of unit detection efficiency will be  $p_{dc} = n_{th} = 1.7 \times 10^{-3}$ .
- **Squeezing parameter  $g$**  We find that the value that maximizes the time for which the CHSH inequality is violated is  $g = 0.172$ , corresponding to a mean photon number of  $\langle n_A \rangle = 0.030$

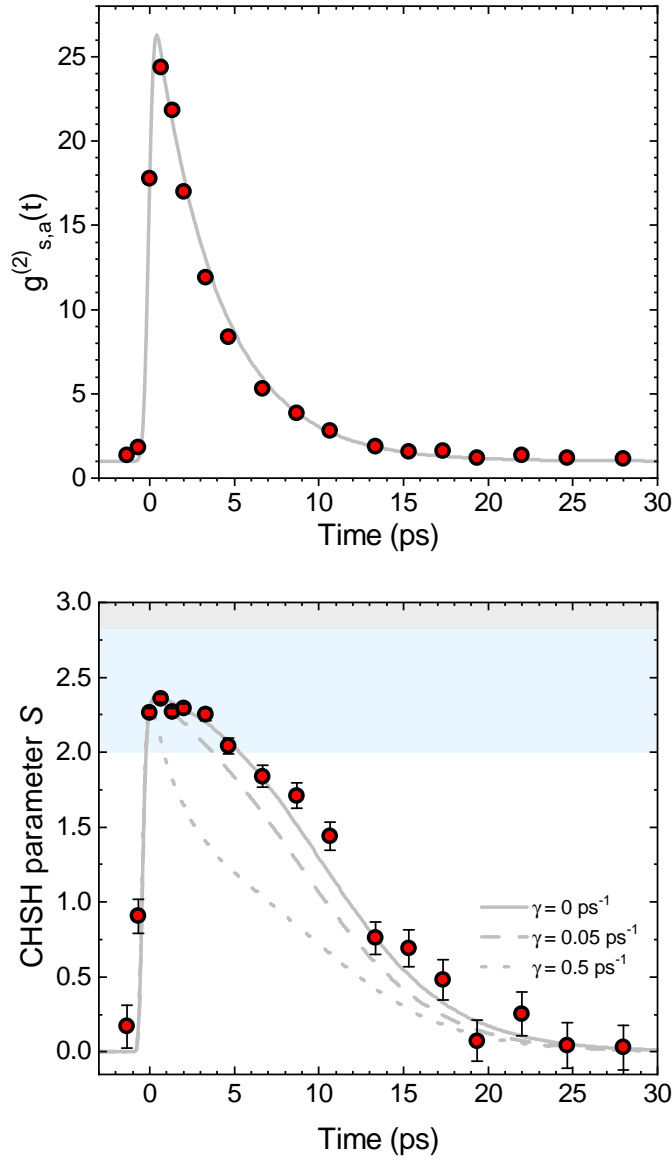


Figure 7.6: **Comparison of the model with experimental data.** **a**, Experimentally measured normalised Stokes–anti-Stokes cross-correlation  $g_{s,a}^{(2)}(\Delta t)$  vs. the write–read time delay  $\Delta t$ , together with an exponential fit with a decay time constant  $\tau = 3.78$  ps, corresponding to the phonon lifetime. **b**, Experimental CHSH parameter (as in main text, Fig. 2) overlaid with the curves computed from eq. (7.39) with the expression for  $g_{s,a}^{(2)}(\Delta t)$  from panel **a**. Different values of the pure dephasing rate are shown, illustrating that our data are consistent with the decoherence of the vibrational qubit being dictated by population decay. The blue region, demarcated by  $2 < |S| \leq 2\sqrt{2}$ , certifies Bell correlations.

In Fig. 7.7 we show the time evolution of the CHSH parameter under ideal measurement. It is

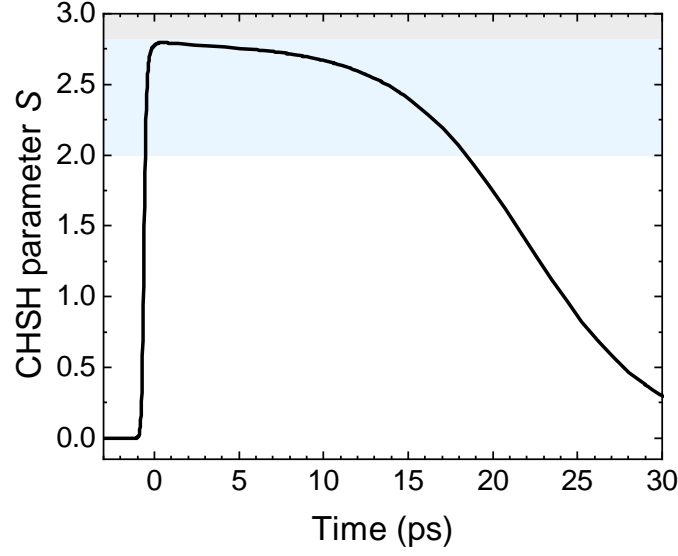


Figure 7.7: **Evolution of the CHSH parameter under ideal experimental conditions.** The ideal conditions assume unit detection efficiency, noise exclusively due to the thermal phonon occupancy, and optimal squeezing parameter.

worth noting that the CHSH inequality is violated for 18.4 ps, almost 5 times longer than the phonon lifetime, and more than twice the coherence time.

This can be understood by noting that the Bell parameter at a given delay  $\Delta t$  is ultimately limited by the value of  $g_{s,a}^{(2)}(\Delta t)$ , which is a measure of the signal-to-noise ratio for the conversion and detection of a heralded single phonon. As long as  $\frac{g_{s,a}^{(2)}-1}{g_{s,a}^{(2)}+1} > \frac{1}{\sqrt{2}}$ , or approximately  $g_{s,a}^{(2)}(\Delta t) \geq 5.85$ , the Bell parameter can exceed 2 (if all experimental imperfections reducing the two-photon interference visibility are mitigated). Therefore, even as  $g_{s,a}^{(2)}(\Delta t)$  falls off exponentially with time, if its initial value is large enough (in the ideal case up to  $1/n_{\text{th}}$ ) then Bell correlation can be observed up to delays several times longer than the exponential coherence time.

Note that this observation raises an interesting prospect. If the technical and background noises are significantly reduced, and the sample temperature lowered, the initial value of  $g_{s,a}^{(2)}$  can be made arbitrarily large. This would allow to put a more stringent bound on the pure dephasing rate  $\gamma$ , and maybe measure its magnitude even if it is much smaller than the exponential decay rate of the phonon. This a general comment that can be applied to other optomechanical systems in the quantum ground state as well.

### 7.2.13 Evaluation of the CHSH value from finite statistics

**CHSH as a game** –In a CHSH test, Alice receives at each run a random bit  $x = \{0, 1\}$  and similarly for Bob  $y = \{0, 1\}$ . When Alice gets  $x$ , she chooses the measurement setting  $A_x$  while Bob chooses  $B_y$ . For each setting choice, they receive a result  $a = \{0, 1\}$  for Alice and  $b = \{0, 1\}$  for Bob. They repeat the experiment many times so that they can evaluate

$$\langle A_x B_y \rangle = p(a = b | A_x B_y) - p(a \neq b | A_x B_y). \quad (7.40)$$

The CHSH value is given by

$$S = \langle A_0 B_0 \rangle + \langle A_0 B_1 \rangle + \langle A_1 B_0 \rangle - \langle A_1 B_1 \rangle. \quad (7.41)$$

Such a test can be phrased as a game in which Alice and Bob receive  $x$  and  $y$ , respectively, as inputs and the winning condition is that their outputs satisfy  $a \oplus b = x \cdot y$  where  $\oplus$  is the sum modulo 2. The winning probability  $q$  relates to the CHSH value  $S$  by

$$q = \frac{4 + S}{8}. \quad (7.42)$$

**Confidence interval on the mean value of winning probability**–Let us see each experimental run as if a random variable  $T_i$  was given. As an estimator of such a random variable  $T_i$ , we choose

$$T_i = \chi(a_i \oplus b_i = x_i \cdot y_i) \quad (7.43)$$

with  $\chi$  the indicator function, i.e.  $\chi(\text{condition}) = 1$  if the condition is satisfied and 0 otherwise. Here  $a_i$  is the result of Alice at run  $i$  and similarly,  $b_i, x_i$  and  $y_i$ . Note that this estimator is unbiased. Indeed

$$\begin{aligned} \mathbf{E}(T_i) &= \sum_{a_i, b_i, x_i, y_i} T_i p(a_i, b_i, x_i, y_i) \\ &= \sum_{a_i, b_i, x_i, y_i} T_i p(a_i, b_i, x_i, y_i) \\ &= \sum_{a_i, b_i, x_i, y_i} T_i p(a_i, b_i | x_i, y_i) p(x_i, y_i) \end{aligned}$$

and since  $p(x_i, y_i) = 1/4$ ,

$$\begin{aligned} \mathbf{E}(T_i) &= \frac{1}{4} \sum_{a_i, b_i, x_i, y_i} T_i p(a_i, b_i | x_i, y_i) \\ &= \frac{1}{4} (p(a_i = b_i = 0 | x_i \neq 1 \text{ and } y_i \neq 1) + p(a_i = b_i = 1 | x_i \neq 1 \text{ and } y_i \neq 1) \\ &\quad + p(a_i = 0, b_i = 1 | x_i = y_i = 1) + p(a_i = 1, b_i = 0 | x_i = y_i = 1)). \end{aligned}$$



Note that

$$\begin{aligned} p(a_i \oplus b_i = 0 | x_i, y_i) &= p(a_i = b_i = 0 | x_i, y_i) + p(a_i = b_i = 1 | x_i, y_i) = \frac{1}{2}(1 + \langle A_{x_i} B_{y_i} \rangle) \\ p(a_i \oplus b_i = 1 | x_i, y_i) &= p(a_i = 0, b_i = 1 | x_i, y_i) + p(a_i = 1, b_i = 0 | x_i, y_i) = \frac{1}{2}(1 - \langle A_{x_i} B_{y_i} \rangle) \end{aligned}$$

Therefore

$$\mathbf{E}(T_i) = \frac{1}{4} \left( \frac{4 + S_i}{2} \right) = q_i \quad (7.44)$$

that is, the expectation of  $T_i$  corresponds to the probability to win the game at run  $i$ . We want to bound the average winning probability  $\bar{q} = \frac{1}{n} \sum_i q_i$ . It was shown in Ref. [35] that  $[q_{\min}, 1]$  is a confidence interval for  $\bar{q}$  with

$$q_{\min} = I_{\alpha}^{-1}(n\bar{T}, n(1 - \bar{T}) + 1) \text{ with } \bar{T} = \frac{1}{n} \sum_i T_i \quad (7.45)$$

where  $0 \leq \alpha \leq 1/2$  is the confidence level (e.g.  $\alpha = 0.01$  corresponds to a confidence level of 99%). Here we defined the inverse regularized incomplete Beta function  $I^{-1}$ , i.e.  $I_y(a, b) = x$  for  $y = I_x^{-1}(a, b)$ .

Given a target confidence level  $\alpha$ , the previous formula can be used to give a lower bound  $S_{\min}$  on the actual value of  $\bar{S}$  using the following steps :

- 1 - Compute  $T_i$  at each run using  $T_i = \chi(a_i + b_i = x_i \cdot y_i)$
- 2 - Deduce  $\bar{T} = 1/n \sum_i T_i$
- 3 - Compute  $q_{\min}$  from the formula eq. (7.45) (for example with  $\alpha = 0.01$  for a confidence level of 99%)
- 4 - Deduce the lower bound  $S_{\min}$  on the mean CHSH value  $\bar{S} = \frac{1}{n} \sum_i S_i$  using  $S_{\min} = 8 * q_{\min} - 4$ .

### Example calculations

We show in detail the calculation for  $\Delta t = 0.66$  ps

We have  $A_x = \{\alpha = 0, \alpha = \pi/2\}$  and  $B_y = \{\varphi = -\pi/4, \pi/4\}$  as the settings for the experiment, and  $a, b = 0$  corresponds to a click in the + detector, while  $a, b = 1$  corresponds to either a click in the - detector or the simultaneous clicking of both + and - detectors on one side (two-photon event).

The coincidence counts observed during the experiment for different settings are summarized in Table 7.2.

Where  $n_{\pm x}$  denotes the events involving two simultaneous coincidences in the Stokes measurement arm. There were no recorded events with simultaneous detections in the anti-Stokes arm.

## Chapter 7. Bell correlations between light and vibration

---

Setting	$n_{++}$	$n_{+-}$	$n_{-+}$	$n_{--}$	$n_{\pm+}$	$n_{\pm-}$
$\theta = 0, \varphi = -\pi/4$	1301	270	458	2034	0	0
$\theta = 0, \varphi = \pi/4$	1338	229	460	2006	1	0
$\theta = \pi/2, \varphi = -\pi/4$	388	1408	1549	694	0	1
$\theta = \pi/2, \varphi = \pi/4$	1468	494	328	1781	1	0

Table 7.2: Coincidence counts

We use this data to calculate  $\bar{T} = 0.785$ . We then compute  $q_{\min}$  for  $\alpha = 0.01$  (99% confidence) and  $\alpha = 5.733 \times 10^{-7}$  ( $5\sigma$  confidence) using (7.45), and obtain  $q_{\min} = 0.788$  and  $q_{\min} = 0.779$ , respectively.

From this we conclude that the lower bound on  $\bar{S}$  with 99% confidence is  $S_{\min} = 2.30$ , and the lower bound with  $5\sigma$  confidence is  $S_{\min} = 2.23$ , which comfortably violates the CHSH inequality.

## 8 Epilogue

One of the big unanswered question in physics is that of when does the transition from the quantum world to the classical world occur. In order to maintain the quantum properties of a system, they typically have to be either at extremely low temperatures, at nanoscopic scales, well isolated from the environment, or all three. In contrast, all our experiments take place at room temperature, atmospheric pressure, and with macroscopic samples. The series of experiments we performed combine spectroscopy with techniques from quantum optics, and reveal progressively more 'quantumness' in their interactions and on the states produced.

The results presented in this thesis started by developing a very general experimental methodology to study Raman-active vibrations using ultrafast optics and time correlated single photon counting. The technique was successfully demonstrated in diamond, and used the Cauchy-Schwarz inequality to prove that the correlations between the Stokes and anti-Stokes fields defy a classical description.

We then used this technique to measure  $\text{CS}_2$ . This allowed us to observe the phonon dynamics of the two dominant isotopic species, as well as prepare them in a quantum superposition. In this case we developed a quantum model for the experiment, and used it to calculate the logarithmic negativity of the states produced, finding that quantum entanglement must be present in the system.

We then focused on the nature of the Raman interaction itself. We demonstrated that the phonon mode initially exists in a thermal state, but the combination of Raman scattering with a measurement of the Stokes scattered photons can yield the  $n=1$  Fock state, which possesses sub-Poissonian statistics, and is perhaps the most characteristic state in quantum optics.

We finished by using this technique to create an entangled photon-phonon state that is capable of violating a Bell-type inequality. Bell-type inequalities are especially significant because of their generality – they provide a limit that cannot be violated by any classical theory, without having to know any specifics about the theory itself – and provide the most stringent test for the non-local nature of an experiment.

These developments are not the end of the story, and in this chapter we explore some of the future research avenues. These include open basic science questions in sections 8.1 and 8.2, as well as advances that could make this field technologically relevant for applications in quantum information and quantum communication in Sec. 8.3.

### 8.1 Position-momentum entanglement in Raman scattering

The original thought experiment proposed by Einstein, Podolsky, and Rosen talked about entanglement between the position and momentum of two particles (29). Later developments simplified the experiment by considering discrete variables, where Bell type inequalities such as the CHSH inequality can be applied, and it was this type of experiment that was first realised (32; 33). It is also this type of experiment which we implemented in Chapter 7.

In more recent years, interest returned to continuous variable entanglement (178), and more practical inequalities were developed in terms of the quadrature operators (179; 180), which were violated experimentally in the early 2000s (181; 182). For SPDC sources, which closely resemble the Raman interaction as explained in Chapters 2 and 3, the first demonstration of EPR entanglement was performed in (183). Beyond the fundamental demonstration, this result has given rise to a growing interest in high-dimensional entanglement, which has potential applications for quantum communication (184).

The conservation of momentum in the SPDC process leads to correlation between the 'signal' and 'idler' photons. Similarly, the conservation laws in Raman scattering will lead to correlations between the Stokes-scattered photon and the generated phonon (77), which will in turn create a correlation with the anti-Stokes photon generated during phonon annihilation. Measuring EPR entanglement involves two sub-measurements, one looking at the far field and one looking at the far field image. In a scenario where the photons scattered from the sample are collimated by a microscope objective, the shape of the far field will provide momentum information, while adding a lens imaging the back-focal plane of the objective will provide position information.

An initial approach to measuring EPR entanglement could be to follow a similar methodology to that of (183), where a slit or pinhole is used before the detectors in order to select a narrow piece of the signals. By moving one of the slits this allows for the measurement of the correlations between different points of the real or  $k$  space image. An advantage of this method is that it requires only one photon counter in each detection arm. A more interesting approach, however, would be to use newly developed photon counting cameras in order to obtain a full measurement without the need to scan (185). This has the added benefit of paving the way for a demonstration of high-dimensional entanglement, for which the only additional requirement would be the structuring of the wavefront of the 'write' and 'read' beams.

## 8.2 Photon correlations away from phonon frequencies

When a laser interacts with a material, a correlated signal is not only obtained when looking at the frequency shifts corresponding to the phonon modes, but also at other frequencies that are symmetrically spaced from the laser (38; 186; 187). In analogy to Cooper pairs in superconductivity, an explanation for the observed correlations has been proposed in terms of virtual phonons (38). The virtual nature of these quasi-particles allows them to take non-resonant energies, and their creation and annihilation within a single laser pulse would lead to the emission of a correlated pair of photons.

An alternative hypothesis, however, is that the creation of correlated photon pairs is simply the result of electronic four wave mixing (FWM), without requiring a phonon-mediated contribution. This process depends on the third order polarizability tensor of a material, and in the case of interest involves the annihilation of two pump photons, accompanied by the creation of two new photons. Energy conservation requires that the sum of the energy of the output photons be equal to twice the pump energy, which allows them to take any pair of energies, provided that they are symmetrically spaced from the pump. In the case of the two-color pump probe measurements, the process can take place by absorbing one photon from the 'write' and one photon from the 'read' pulse, again leading to correlated photons, this time symmetrically spaced around the average laser frequency. FWM is a virtual process, which only takes place when both lasers are temporally overlapped on the sample, which means that when we are measuring the phonon modes we should also see a contribution from this component in the  $g_{S,A}^{(2)}(t)$  measurements. We already see hints of this in the CS<sub>2</sub> measurements, where there is an extra component at  $g_{S,A}^{(2)}(0)$ , as explained in Chapter 5.

Both of these theories offer a qualitative explanation for the correlations observed at frequencies other than the phonon modes. However, the polarization selection rules of the  $\chi^{(3)}$  tensor are also different from the Raman tensor. In CS<sub>2</sub>, for example, the measured components of the  $\chi^{(3)}$  tensor relevant for FWM differ by less than a factor of two for the different polarization configurations (188). The Raman measurement, in contrast, is almost completely polarized, having a depolarization ratio of  $\sim 1/6$  (189), and the selection rules of the proposed virtual phonon process are the same as those for standard Raman scattering (190). The two competing explanations will therefore lead to a different prediction for the relative strength of the correlations measured under different polarization conditions, providing a way to experimentally assess their validity.

## 8.3 Advances for practical applications

One of the key limitation when trying to use the techniques we developed for technological applications is the short phonon lifetime of the materials we have studied.

As we mentioned before, the phonon lifetime in diamond is limited by the decay through the Klemens channel (141; 49), for which there is no expected temperature dependence, but

which could potentially be closed by the creation of a phononic band gap in an atomic scale  $^{12}\text{C}$ - $^{13}\text{C}$  super lattice. In other materials, however, a change in temperature can lead to longer phonon lifetimes. In ZnSe, InN and AlN, for example, it has been shown that, by cooling the sample from room temperature to  $\sim 10^\circ\text{K}$ , the phonon lifetime increases by a factor of  $\sim 5$  (191; 192; 193) A promising alternative platform consists of molecules trapped in an optical lattice, where lifetimes in the range of 10s of ms have been demonstrated (171) in  $\text{Sr}_2$ .

The other key limitation is the efficiency of the memory process. In the experiments shown in this thesis, which have not attempted to optimize the process, the readout efficiency is in the order of  $10^{-4}$ , but similar schemes done with the goal of developing a quantum memory have been able to demonstrate readout efficiencies in the order of  $10^{-1}$  by using much higher pulse energies (17). Improvements are still required in order to reach the near unity efficiency that is desired for practical applications, and one possible approach is to add an optical cavity (194), which can enhance the Raman interaction while suppressing the noise generated by other non-linear effects. In a similar vein, these experiments can be combined with metallic surfaces and nano-particles (195), which increases the probability of Raman scattering by several orders of magnitude (196). This could be used as a way to increase the efficiency of the process, and it also offers the possibility to study the interaction between the plasmonic cavities and molecular vibrations (78; 79).

The correlations in a Raman scattered light field carry a wealth of information, and they can be used to reveal rich physics regarding both the interaction and the phonon field itself. Whether it is for practical applications or fundamental studies, there are plenty of interesting avenues to explore, and studying single-photon correlations offers a promising avenue to expand Raman spectroscopy and molecular sciences into the realm of quantum science and technology.

# 9 Code for "Two-Color Pump-Probe Measurement of Photonic Quantum Correlations Mediated by a Single Phonon"

This appendix shows the code used to process the data shown in Ch. 4.

## 9.1 Code for data analysis

```
1000 """ Example of how to analyze a dataset:
1001     #if there is a background:
1002     bkgData=Data[:,bkgColumn]
1003     bkgPeak=findBkgPeakHeight(bkgData,corrPeakNum,peakIndex)#if there is a background
1004     #otherwise set bkgPeak=0; not sending bkgPeak also works
1005     data=Data[:,dataColumn]
1006     g2,errorBar,avgNonCorrPeak=analyzeCorr(data,corrPeakNum,peakIndex,bkgPeak)
1007 """
1008
1009 import numpy as np
1010 import matplotlib.pyplot as plt
1011 from scipy import signal
1012 import os
1013
1014 def main():
1015     dataFileName="SaS-Data-26-01-2018.txt"
1016     analysisDirName="AnalysisResults"
1017     expectedPeakNum=26 ###
1018     corrPeakNum=1 #starting to count from zero
1019
1020     dataFile=np.genfromtxt(dataFileName,skip_header=1)
1021     postProcessedData=np.zeros(np.shape(dataFile))
1022     postProcessedData[:,0]=dataFile[:,0] #Time
1023     results=np.zeros((len(dataFile[0,:])-1,4))
1024
1025     bkg=np.zeros(dataFile[:,0].shape)
1026
1027     Names=['Time','PosN0.2','PosN0.1','PosN0.05','PosP0','PosP0.05',
1028           'PosP0.1','PosP0.2','PosP0.3','PosP0.4','PosP0.6','PosP0.8',
1029           'PosP1.0','PosP1.2','PosP1.4','PosP1.7','PosP2.0','PosP2.5']
1030     DelayPos=np.array([-0.2,-0.1,-0.05,0,0.05,0.1,0.2,0.3,0.4,0.6,0.8,1,
1031                       1.2,1.4,1.7,2.0,2.5])
1032     #Using the same peak index for all measurements:
```

## Chapter 9. Code for "Two-Color Pump-Probe Measurement of Photonic Quantum Correlations Mediated by a Single Phonon"

```

peakIndex=findPeakIndex( dataFile[:,3], expectedPeakNum)

1034
DelayTimes=(DelayPos*2)/((3*10**8)*(10**3))*(10**12)
1036 results[:,0]=DelayTimes.T
for i in range(len(Names)-1):
1038     ind=i+1
    print("For "+Names[ind])
1040     cdata=dataFile[:,ind]
    bkgPeak=0
1042     g2, avgNonCorrPeak=analyzeCorr(cdata-bkg, corrPeakNum, peakIndex, bkgPeak)
    errorBar=findError(cdata-bkg, corrPeakNum, peakIndex, g2)
1044     print("\tg2={:.2f}, err={:.2f}, avgNonCorrPeak={:.2f}".format(g2, errorBar, avgNonCorrPeak))
    results[i,1:]=[g2, errorBar, avgNonCorrPeak]
1046     postProcessedData[:,ind]=findPostProcessedData(cdata-bkg, corrPeakNum, peakIndex, bkgPeak)
    plotPeakIndPositions(dataFile[:,0], postProcessedData[:,ind], peakIndex, corrPeakNum, title=
Names[ind])
1048     np.savetxt("g2Results.txt", results, newline='\r\n', header='Delay\tg2\terr\tavgUncorrPeak',
    delimiter='\t')
    np.savetxt("PostProcessedData.txt", postProcessedData, newline='\r\n', header='\t'.join(Names),
    delimiter='\t')
1050     plotRelaxation(results, 'Relaxation Time')

1052 def findBkgPeakHeight(bkgData, corrPeakNum, peakIndex):
    bkgData=bkgData-findOffset(bkgData, peakIndex)
1054     bkgPeak=findAvgPeak(bkgData, corrPeakNum, peakIndex, All=True)
    return bkgPeak

1056 def analyzeCorr(data, corrPeakNum, peakIndex, bkgPeak=0):
    data=data-findOffset(data, peakIndex)
1058     avgNonCorrPeak=findAvgPeak(data, corrPeakNum, peakIndex, nonCorr=True)
    g2, errorBar=findg2(data, corrPeakNum, peakIndex, bkgPeak) #errorBar is obsolete
1060     return g2, avgNonCorrPeak

1062 def findPostProcessedData(data, corrPeakNum, peakIndex, bkgPeakArea=0):
    post=data-findOffset(data, peakIndex)
1064     Areas=np.array([post[peak-1]+post[peak]+post[peak+1] for peak in peakIndex])
    Areas=Areas-bkgPeakArea
1066     for i in range(len(peakIndex)):
        post[peakIndex[i]-1]=Areas[i]
        post[peakIndex[i]]=Areas[i]
1070     post[peakIndex[i]+1]=Areas[i]
    return post

1072 def findOffset(data, peakIndex):
    #data is already only the column of interest, i.e. Data[:,i]
1074     total=np.sum(data)
    peaks=np.sum([data[peak-1]+data[peak]+data[peak+1] for peak in peakIndex])
1076     return (total-peaks)/(len(data)-3*len(peakIndex))

1078 def findAvgPeak(data, corrPeakNum, peakIndex, nonCorr=True, All=False):
    peakAreas=[data[peak-1]+data[peak]+data[peak+1] for peak in peakIndex]
1080     if All:
        return np.average(peakAreas)
    if nonCorr:
1084         nonCorrPeakAreas=[peakAreas[i] for i in range(len(peakIndex)) if i!=corrPeakNum]
        return np.average(nonCorrPeakAreas)

1086 def findg2(data, corrPeakNum, peakIndex, bkgPeakArea=0):
    Areas=np.array([data[peak-1]+data[peak]+data[peak+1] for peak in peakIndex])
1088     Areas=Areas-bkgPeakArea

```



```

1090 nonCorrAreas=[Areas[i] for i in range(len(Areas)) if i!=corrPeakNum]
1091 g2=Areas[corrPeakNum]/np.average(nonCorrAreas)
1092 errorBar=np.std(nonCorrAreas)/np.average(nonCorrAreas)
1093 return g2,errorBar
1094
1095 def findError(data,corrPeakNum,peakIndex,g2):
1096     data=data-findOffset(data,peakIndex)
1097     peakAreas=[data[peak-1]+data[peak]+data[peak+1] for peak in peakIndex]
1098     SPAreas=[peakAreas[i] for i in range(len(peakIndex)) if i!=corrPeakNum]
1099     CPArea=peakAreas[corrPeakNum]
1100     avgSPArea=np.average(SPAreas)
1101     stdSPArea=np.std(SPAreas)
1102     Error=g2*np.sqrt((stdSPArea/avgSPArea)**2+(1/CPArea))
1103     return Error
1104
1105 def plotPeakIndPositions(time,counts,peakIndex,corrPeakNum,title='no title'):
1106     Fig,ax=plt.subplots(1,1)
1107     ax.plot(time,counts)
1108     for i in range(len(peakIndex)):
1109         if i!=corrPeakNum:
1110             ax.axvline(time[peakIndex[i]],0,10,color='r',linestyle='--')
1111     ax.axvline(time[peakIndex[corrPeakNum]],0,10,color='g',linestyle='--')
1112     ax.set_xlabel('Time (ns)')
1113     ax.set_ylabel('Counts')
1114     Fig.suptitle(title)
1115     Fig.savefig(str(title)+'.png')
1116     return
1117
1118 def findPeakIndex(data,title='no name',expectedPeakNum=26,minLength=6):
1119     peakIndex=signal.find_peaks_cwt(data,np.arange(0.1,12),min_length=minLength)
1120     if len(peakIndex)!=expectedPeakNum:
1121         print("WARNING: unexpected peak number in"+str(title))
1122         print("{} peaks found when {} were expected".format(len(peakIndex),expectedPeakNum))
1123     return peakIndex
1124
1125 def plotPower(results,title='Title'):
1126     Fig,ax=plt.subplots(1,1)
1127     ax.errorbar(results[:,0],results[:,1],yerr=results[:,2],fmt="o",capsize=3,elinewidth=1)
1128     ax.axhline(1,0,10,color='g',linestyle='--')
1129     ax.grid(True)
1130     ax.set_xlabel('Power (mW)')
1131     ax.set_ylabel(r'$g^2_{(S,aS)}(\tau)$')
1132     Fig.suptitle(title)
1133     Fig.savefig(str(title)+'.png')
1134     return
1135
1136 def plotRelaxation(results,title='Relaxation Time'):
1137     Fig,ax=plt.subplots(1,1)
1138     ax.errorbar(results[:,0],results[:,1],yerr=results[:,2],fmt="o",capsize=3,elinewidth=1)
1139     ax.axhline(1,0,10,color='g',linestyle='--')
1140     ax.grid(True)
1141     ax.set_xlabel(r'$\tau$ (ps)')
1142     ax.set_ylabel(r'$g^2_{(S,aS)}(\tau)$')
1143     Fig.suptitle(title)
1144     Fig.savefig(str(title)+'.png')
1145     return
1146
1147
1148

```

## Chapter 9. Code for "Two-Color Pump-Probe Measurement of Photonic Quantum Correlations Mediated by a Single Phonon"

---

```
1150 if __name__ == "__main__":  
    main()
```

# 10 Code for "Preparation and decay of a single quantum of vibration at ambient conditions"

This appendix shows the code used to acquire and process the data shown in Ch. 6, following the procedure outlined in Sec. 6.3.1.

The large amount of data during this experiments required us to measure in increments of 1 minute, typically for a total of 1 hour, and all the relevant data files are joined in post processing. After  $\sim 1$  minute of measuring under typical conditions, the size of the compressed binary file obtained is  $\sim 1$ MB, which translates into a text file of  $\sim 20$ MB. In order to prevent memory problems, in post processing the files are temporarily decompressed, and the coincidence information is extracted and added to the analysis one by one.

## 10.1 Code for data analysis

```
1000 # By Santiago Tarrago
1001 #
1002 # Analysis set of measurements from delay scan in T3 mode
1003 #
1004 # Provides the histogram for each acquisition, and the summed histogram for each
1005 # position
1006 #
1007 # Provides de counts and g2 value for each aquisition to help identify problems;
1008 # if they exist they have to be dealt with by hand
1009 #
1010 # Calculates the heralded anti-bunching for each delay position
1011
1012 import numpy as np
1013 import matplotlib.pyplot as plt
1014 import os
1015 import re
1016 import subprocess
1017 from scipy import signal
1018
1019 def main():
1020     np.warnings.filterwarnings('ignore')###
1021     baseName = 'Test' #Name before PosX.XX-XXX.out
```

## Chapter 10. Code for "Preparation and decay of a single quantum of vibration at ambient conditions"

```
1022 # Variables for histograms and binning: #
    binSize=0.5 #in nano seconds
1024 maxTime=310#limit of histogram in ns
    convFactor=0.25 #converts saved timediff info into ns
1026 chl_offset=8.7 #in ns
    double_count_timewindow=4 #ns
1028 # Variables for g2 calculation: #
    peakIndex_ch0=np.array([27,52,77,102,127,151,176,201,226,251,275,300,325\
1030                          ,350,375,400,424,449,474,499,524,549,574,598]) #currently ignores the
    left-most peak
    corrPeakNum_ch0=0 #starting to count from zero
1032 peakIndex_ch1=np.array([10,35,59,84,109,134,159,184,209,233,258,283,308,\
                          333,358,382,407,432,457,482,506,531,556,581,606])
1034 corrPeakNum_ch1=0 #starting to count from zero
    numBinsArea = 3 #how many bins each way from the peak to take into account
1036 # Finding folders to analyse: #
    cwd = os.getcwd()
1038 folderNames, delayPositions = findFolders(baseName)
    Results_total=np.zeros((len(delayPositions),10))#heralded antibunching results
1040 Results_total[:,0]=(delayPositions*2)/((3*10**8)*(10**3))*(10**12)#delayTime

1042 for folder in folderNames:
    os.chdir(cwd)
1044 os.chdir(cwd+'\\'+folder)
    fileNames=findFiles(folder)
1046 measInfo=np.zeros((len(fileNames),7))#Stores sync and signal counts,g2 and err for each
    measurement
    binNum=int(maxTime/binSize)
1048 totalHistogram=np.zeros((binNum,4))
    totalHistogram[:,0]=np.arange(binNum)*binSize
1050 for i in range(len(fileNames)):
    info,histogram=analyzeBinnary(fileNames[i],binSize,maxTime,convFactor,chl_offset,
    double_count_timewindow,\
1052                                peakIndex_ch0,corrPeakNum_ch0,peakIndex_ch1,
    corrPeakNum_ch1,numBinsArea)
    measInfo[i]=info
1054 totalHistogram[:,1:]=totalHistogram[:,1:]+histogram[:,1:]
    #Save measurement information (and plt), both in current and analysis folder
1056 indices=np.array([int(file[-7:-4]) for file in fileNames])
    plotStability(indices,measInfo,folder+'_stabilityPlot')
1058 saveStabilityInfo(indices,measInfo,folder+'_stabilityInfo.txt')
    measTime=60*len(fileNames)
1060 total_info=analyzeTotalHist(measInfo,totalHistogram,peakIndex_ch0,corrPeakNum_ch0,\
                                peakIndex_ch1,corrPeakNum_ch1,numBinsArea,measTime)
1062 saveTotalHist(folder+'_total_histogram.txt',totalHistogram,total_info)
    Results_total[folderNames.index(folder),1:]=total_info
1064 os.chdir(cwd)
    saveFinalResult('Analysis_Result.txt',Results_total)
1066 plotFinalResult('DecayCurves',Results_total)
    return
1068

1070 def findFolders(baseName):
    folderRegex=re.compile('('+baseName+r'Pos)([-]?[d+][.]?[d*]')
1072 directoryContent=os.listdir()
    folderNames=[]
1074 delays=[]
    for name in directoryContent:
1076         match=folderRegex.search(name)
        if match!=None:
```

```

1078         folderNames.append(name)
1079         delays.append(float(match.group(2)))
1080     return folderNames,np.array(delays)

1082 def findFiles(folder):
1083     fileRegex=re.compile('('+folder+r'-)(\d\d\d\d).out')
1084     directoryContent=os.listdir()
1085     fileNames=[]
1086     for name in directoryContent:
1087         match=fileRegex.search(name)
1088         if match!=None:
1089             if folder+'-'+match.group(2)+'_info.txt' in directoryContent:#makes sure the info file
1090             exists
1091                 fileNames.append(name)
1092     return np.array(fileNames)

1094 def analyzeBinnary(fileName,binSize,maxTime,convFactor,ch1_offset,double_count_timewindow,\
1095                    peakIndex_ch0,corrPeakNum_ch0,peakIndex_ch1,corrPeakNum_ch1,numBinsArea):
1096     print(fileName)
1097     #Create temporary txt file: #
1098     cwd=os.getcwd()
1099     c_executable_name=r"C:\Users\tarrago\Documents\DataAnalysis\2018-06-11 T3 analysis\
FullAnalysis\ReadT3.exe"
1100     in_file=fileName
1101     out_file=fileName[:-4]+'_tmp_file.txt'
1102     command=c_executable_name+' '+in_file+' '+out_file
1103     subprocess.run(command)
1104     #Make Histograms: #
1105     Data=np.genfromtxt(out_file,invalid_raise=False)
1106     ch0_rawData,ch1_rawData=separateData(Data)
1107     ch0_binnedData=binData(ch0_rawData,binSize,maxTime,convFactor)
1108     ch1_binnedData=binData(ch1_rawData,binSize,maxTime,convFactor)
1109     SaSaS=combinedBinnedData(ch0_rawData,ch1_rawData,ch1_offset,binSize,double_count_timewindow,
maxTime,convFactor)
1110     #print('Total three-fold counts: '+str(np.sum(SaSaS[:,1])))
1111     combinedHist=np.zeros((len(ch0_binnedData),4))
1112     combinedHist[:,2]=ch0_binnedData
1113     combinedHist[:,2]=ch1_binnedData[:,1]
1114     combinedHist[:,3]=SaSaS[:,1]
1115     # Analyze Data: #
1116     if (peakIndex_ch0==-1).all():
1117         peakIndex_ch0=findPeakIndex(ch0_binnedData[:,1],fileName[:-4],24)
1118     if (peakIndex_ch1==-1).all():
1119         peakIndex_ch1=findPeakIndex(ch1_binnedData[:,1],fileName[:-4],25)
1120     ch0_g2,ch0_g2_error=findg2(ch0_binnedData,peakIndex_ch0,corrPeakNum_ch0,numBinsArea)
1121     ch1_g2,ch1_g2_error=findg2(ch1_binnedData,peakIndex_ch1,corrPeakNum_ch1,numBinsArea)
1122     counts_sync,counts_ch0,counts_ch1=findChCounts(fileName[:-4]+'_info.txt')
1123     infoVars=np.array([counts_sync,counts_ch0,counts_ch1,ch0_g2,ch0_g2_error,\
ch1_g2,ch1_g2_error])
1124     os.remove(out_file)
1125     return infoVars,combinedHist

1126 def analyzeTotalHist(measInfo,totalHistogram,peakIndex_ch0,corrPeakNum_ch0,\
1127                    peakIndex_ch1,corrPeakNum_ch1,numBinsArea,measTime):
1128     counts_sync,counts_ch0,counts_ch1=np.average(measInfo[:,3],axis=0)
1129     ch0_g2,ch0_g2_error=findg2(totalHistogram[:,2],peakIndex_ch0,corrPeakNum_ch0,numBinsArea)
1130     ch1_Data=np.append(np.array([totalHistogram[:,0]]).T,np.array([totalHistogram[:,2]]).T,axis=1)
1131     ch1_g2,ch1_g2_error=findg2(ch1_Data,peakIndex_ch1,corrPeakNum_ch1,numBinsArea)
1132     heralded_g2,heralded_g2_error=find_heralded_g2(

```

## Chapter 10. Code for "Preparation and decay of a single quantum of vibration at ambient conditions"

```
counts_sync, totalHistogram, measTime, peakIndex_ch0, peakIndex_ch1, \
1136 corrPeakNum_ch0, corrPeakNum_ch1, numBinsArea)

1138 infoVars=np.array([counts_sync, counts_ch0, counts_ch1, ch0_g2, ch0_g2_error, \
                    ch1_g2, ch1_g2_error, heralded_g2, heralded_g2_error])
1140 return infoVars
##### Functions to turn measurements into histograms: #####
1142 def separateData(Data):
    ch0_Data=np.array([line for line in Data if line[2]==0])
1144    ch1_Data=np.array([line for line in Data if line[2]==1])
    return ch0_Data, ch1_Data
1146
def binData(rawData, binSize, maxTime=120, convFactor=0.25):
1148    binNum=int(maxTime/binSize)
    #Convert to nanoseconds:#
1150    timeDiffs=rawData[:,5]*convFactor
    #Initializes histogram: #
1152    histogram=np.zeros((binNum,2))
    histogram[:,0]=np.arange(binNum)*binSize
1154    #Fills histogram: #
    histogramPlace=(timeDiffs/binSize).astype(int)
1156    for point in histogramPlace:
        if point<binNum:
1158            histogram[point,1]=histogram[point,1]+1
    return histogram
1160
def combinedBinnedData(ch0_rawData, ch1_rawData, ch1_offset, binSize, double_count_timewindow=1, maxTime
=120, convFactor=0.25):
1162    binNum=int(maxTime/binSize)
    #Initializes histogram: #
1164    histogram=np.zeros((binNum,2))
    histogram[:,0]=np.arange(binNum)*binSize
1166    #Offset for channel 1 and convert to ns:#
    ch0_offsetData=np.copy(ch0_rawData)
1168    ch0_offsetData[:,5]=ch0_offsetData[:,5]*convFactor
    ch1_offsetData=np.copy(ch1_rawData)
1170    ch1_offsetData[:,5]=ch1_offsetData[:,5]*convFactor
    ch1_offsetData[:,5]=ch1_offsetData[:,5]+ch1_offset
1172    #Finds double coincidence events: #
    for ch0_point in ch0_offsetData:
1174        index=np.searchsorted(ch1_offsetData[:,3], ch0_point[3]) #finds the closest sync count
        try: #the ch0 and ch1 arrays can have slightly different lengths
1176            if ch0_point[3]==ch1_offsetData[index,3]:#happened during the same sync event
                #print('Event happened in same sync period')
                if abs(ch0_point[5]-ch1_offsetData[index,5]) < double_count_timewindow: #happened
1178                    in allowed time window
                    #print('Event happened in window')
                    if (ch0_point[5]/binSize).astype(int)<binNum: #the coincidence falls in the
1180                        hist
                            binPlace=(ch0_point[5]/binSize).astype(int)
                            #print("Added to Histogram in bin: "+str(binPlace))
                            histogram[binPlace,1]=histogram[binPlace,1]+1
1182                    except:
                        pass
1184    return histogram
##### Functions to turn analyze histograms: #####
1188 def findg2(data, peakIndex, corrPeakNum, numBinsArea):
1190    counts=data[:,1]
    counts=counts-findOffset(counts, peakIndex, numBinsArea)
```

```

1192 peakAreas=np.array([np.sum(counts[(peak-numBinsArea):(peak+numBinsArea+1)])\
1193                     for peak in peakIndex])
1194 SPAreas=np.array([peakAreas[i] for i in range(len(peakIndex)) \
1195                  if i!=corrPeakNum])
1196 CPEArea=peakAreas[corrPeakNum]
1197 avgSPAArea=np.average(SPAreas)
1198 stdSPAArea=np.std(SPAreas)
1199 g2=CPEArea/avgSPAArea
1200 error=g2*np.sqrt((stdSPAArea/avgSPAArea)**2+(1/CPEArea))
1201 return g2,error
1202
1203 def findPeakIndex(data, title='no name', expectedPeakNum=25, minLength=9):
1204     peakIndex=signal.find_peaks_cwt(data, np.arange(0.1, 12), min_length=minLength)
1205     if len(peakIndex)!=expectedPeakNum:
1206         print("WARNING: unexpected peak number in"+str(title))
1207         print("{} peaks found when {} were expected".format(len(peakIndex), expectedPeakNum))
1208     return peakIndex
1209
1210 def findOffset(data, peakIndex, numBinsArea):
1211     total=np.sum(data)
1212     peakAreas=np.array([np.sum(data[(peak-numBinsArea):(peak+numBinsArea+1)])\
1213                        for peak in peakIndex])
1214     peaks=np.sum(peakAreas)
1215     return (total-peaks)/(len(data)-(1+2*numBinsArea)*len(peakIndex))
1216
1217 def findChCounts(fileName):
1218     countRx=re.compile(r'(Syncrate|Countrate\[0\]|Countrate\[1\])=(\d+)/s')
1219     f = open(fileName, 'rt')
1220     for line in f:
1221         match = countRx.search(line)
1222         if match != None:
1223             if match.group(1)=='Syncrate':
1224                 counts_sync=match.group(2)
1225             if match.group(1)=='Countrate[0]':
1226                 counts_ch0=match.group(2)
1227             if match.group(1)=='Countrate[1]':
1228                 counts_ch1=match.group(2)
1229     f.close()
1230     return counts_sync, counts_ch0, counts_ch1
1231
1232 def find_heralded_g2(S_counts_rate, tot_histogram, measTime, peakIndex_ch0, peakIndex_ch1, \
1233                    corrPeakNum_ch0, corrPeakNum_ch1, numBinsArea):
1234     S_counts=S_counts_rate*measTime
1235
1236     SaS_ch0_Data=tot_histogram[:, 1]
1237     SaS_ch0_counts=np.sum(
1238         SaS_ch0_Data[(peakIndex_ch0[corrPeakNum_ch0]-numBinsArea):\
1239                     (peakIndex_ch0[corrPeakNum_ch0]+numBinsArea+1)])
1240     SaS_ch1_Data=tot_histogram[:, 2]
1241     SaS_ch1_counts=np.sum(
1242         SaS_ch1_Data[(peakIndex_ch1[corrPeakNum_ch1]-numBinsArea):\
1243                     (peakIndex_ch1[corrPeakNum_ch1]+numBinsArea+1)])
1244     SaSaS_Data=tot_histogram[:, 3]
1245     SaSaS_counts=np.sum(
1246         SaSaS_Data[(peakIndex_ch0[corrPeakNum_ch0]-numBinsArea):\
1247                   (peakIndex_ch0[corrPeakNum_ch0]+numBinsArea+1)])
1248     print('SaSaS_counts: ' +str(SaSaS_counts))
1249     g2_cond=(SaSaS_counts*S_counts)/(SaS_ch0_counts*SaS_ch1_counts)
1250
1251     if SaSaS_counts!=0:

```

## Chapter 10. Code for "Preparation and decay of a single quantum of vibration at ambient conditions"

```
1252     g2_cond_error=g2_cond*np.sqrt(
1253         (1/S_counts)+(1/SaS_ch0_counts)+(1/SaS_ch1_counts)+(1/SaS_counts))
1254     else:
1255         g2_cond_error=2
1256
1257     print('Heralded g2: {} +- {}'.format(g2_cond,g2_cond_error))
1258     return g2_cond,g2_cond_error
1259
1260 ### Saving graphs and information: ###
1261 def saveHist(name,histogram,infoVars):
1262     info='Sync counts: {} / s\nCh0 counts: {} / s\nCh1 counts: {} / s\ng2_ch0: {} +- {} \ng2_ch1: {} +- {} \n'.format(*infoVars)
1263     cols='Time(ns)\tCounts_ch0\tCounts_ch1\tDouble_coincidences '
1264     headerStr=info+cols
1265     np.savetxt(name,histogram,delimiter='\t',header=headerStr)
1266     return
1267 def saveTotalHist(name,histogram,infoVars):
1268     info='Sync counts: {} / s\nCh0 counts: {} / s\nCh1 counts: {} / s\ng2_ch0: {} +- {} \ng2_ch1: {} +- {} \nheralded_g2 {} +- {} \n'.format(*infoVars)
1269     cols='Time(ns)\tCounts_ch0\tCounts_ch1\tDouble_coincidences '
1270     headerStr=info+cols
1271     np.savetxt(name,histogram,delimiter='\t',header=headerStr)
1272     return
1273 def saveFinalResult(name,Results):
1274     headerStr='DelayTime(ps)\tSync_counts/s\tCh0_counts/s\tCh1_counts:/s\tg2_ch0\tg2_ch0_err\tg2_ch1\tg2_ch1_err\tg2_cond\tg2_cond_err\n'
1275     np.savetxt(name,Results,delimiter='\t',header=headerStr)
1276     return
1277
1278
1279 def plotStability(indices,infoVars,title):
1280     fig,axarr=plt.subplots(2,2)
1281     axarr[0,0].set_title('Stokes counts /s')
1282     axarr[0,0].scatter(indices,infoVars[:,0])
1283     axarr[0,1].set_title('Anti-Stokes counts /s')
1284     axarr[0,1].scatter(indices,infoVars[:,1])
1285     axarr[0,1].scatter(indices,infoVars[:,2],c='g')
1286     axarr[1,0].set_title('g2 S-aS_ch0')
1287     axarr[1,0].errorbar(indices,infoVars[:,3],yerr=infoVars[:,4],fmt="o")
1288     axarr[1,1].set_title('g2 S-aS_ch1')
1289     axarr[1,1].errorbar(indices,infoVars[:,5],yerr=infoVars[:,6],fmt="o",c='g')
1290     fig.suptitle(title)
1291     for ax in axarr.flat:
1292         ax.set_ylim(0)
1293         ax.grid(True)
1294     fig.subplots_adjust(hspace=0.3)
1295     fig.savefig(str(title)+'.png')
1296     return
1297
1298 def saveStabilityInfo(indices,measInfo,title):
1299     headerStr='fileNumber\tSync_counts/s\tCh0_counts/s\tCh1_counts:/s\tg2_ch0\tg2_ch0_err\tg2_ch1\tg2_ch1_err\t'
1300     data=np.append(np.array([indices]).T,measInfo,axis=1)
1301     np.savetxt(title,data,delimiter='\t',header=headerStr)
1302     return
1303
1304 def plotFinalResult(title,Results):
1305     fig,axarr=plt.subplots(2,1)
1306     axarr[0].set_title('S-aS Decay')
1307     axarr[0].errorbar(Results[:,0],Results[:,4],yerr=Results[:,5],fmt="o",label='CH0')
1308     axarr[1].set_title('S-aS Decay')
```



```

1310     axarr[0].errorbar(Results[:,0],Results[:,6],yerr=Results[:,7],fmt="o",c='g',label='CH1')

    axarr[1].set_title('Conditional aS-aS')
1312     axarr[1].errorbar(Results[:,0],Results[:,8],yerr=Results[:,9],fmt="o",label='aS-aS')
    for ax in axarr.flat:
1314         ax.set_ylim(0)
        ax.grid(True)
1316     fig.subplots_adjust(hspace=0.3)
    fig.savefig(str(title)+'.png')
1318     return

1320
main()

```

## 10.2 Code for data acquisition

This code is written in Python, combining standard functionality with the dedicated libraries provided by PicoQuant.

```

1000 import time
    import ctypes as ct
1002 from ctypes import byref
    import sys
1004 import struct
    import os
1006 import visa

1008 # From th260defn.h
    LIB_VERSION = "3.1"
1010 MAXDEVNUM = 4
    MODE_T2 = 2
1012 MODE_T3 = 3
    MAXLENCODE = 5
1014 MAXINPCHAN = 2
    TTREADMAX = 131072
1016 FLAG_OVERFLOW = 0x0001
    FLAG_FIFOFULL = 0x0002

1018 # Measurement parameters, these are hardcoded since this is just a demo
1020 mode = MODE_T3 # set T2 or T3 here, observe suitable Syncdivider and Range!
    binning = 0 # you can change this, meaningful only in T3 mode
1022 offset = 0 # you can change this, meaningful only in T3 mode
    tacq = 60000 # Measurement time in millisec, you can change this
1024 syncDivider = 1 # you can change this, observe mode! READ MANUAL!
    ### For TimeHarp 260 N
1026 syncTriggerEdge = 0 # you can change this
    syncTriggerLevel = 300 # you can change this
1028 inputTriggerEdge = 0 # you can change this
    inputTriggerLevel = 300 # you can change this

1030 # Variables to store information read from DLLs
1032 buffer = (ct.c_uint * TTREADMAX)()
    dev = []
1034 libVersion = ct.create_string_buffer(b"", 8)###
    hwSerial = ct.create_string_buffer(b"", 8)

```

## Chapter 10. Code for "Preparation and decay of a single quantum of vibration at ambient conditions"

```
1036 hwPartno = ct.create_string_buffer(b"", 8)
1037 hwVersion = ct.create_string_buffer(b"", 16)
1038 hwModel = ct.create_string_buffer(b"", 16)
1039 errorString = ct.create_string_buffer(b"", 40)
1040 numChannels = ct.c_int()
1041 resolution = ct.c_double()
1042 syncRate = ct.c_int()
1043 countRate = ct.c_int()
1044 flags = ct.c_int()
1045 nRecords = ct.c_int()
1046 ctcstatus = ct.c_int()
1047 warnings = ct.c_int()
1048 warningstext = ct.create_string_buffer(b"", 16384)

1050 #th260lib = ct.CDLL("th260lib.dll")
1051 th260lib = ct.windll.th260lib

1052 def closeDevices():
1053     for i in range(0, MAXDEVNUM):
1054         th260lib.TH260_CloseDevice(ct.c_int(i))
1055     exit(0)

1058 def stoppttr():
1059     tryfunc(th260lib.TH260_StopMeas(ct.c_int(dev[0])), "StopMeas")
1060     #closeDevices()

1062 def tryfunc(retcode, funcName, measRunning=False):
1063     if retcode < 0:
1064         th260lib.TH260_GetErrorString(errorString, ct.c_int(retcode))
1065         print("TH260.%s error %d (%s). Aborted." % (funcName, retcode, \
1066             errorString.value.decode("utf-8")))
1067         if measRunning:
1068             stoppttr()
1069         else:
1070             closeDevices()

1072 ##### Measurement: #####
1073 def Measure(fileName, delayStage):
1074     ##Save acquisition settings and counts##
1075     settingsFile=open(fileName+'_info.txt', "w")
1076     settingsFile.write(time.strftime("%Y-%m-%d %H:%M:%S", time.gmtime()))
1077     settingsFile.write("\nUsing the following settings:\n")
1078     settingsFile.write("Mode : %d\n" % mode)
1079     settingsFile.write("Binning : %d\n" % binning)
1080     settingsFile.write("Offset : %d\n" % offset)
1081     settingsFile.write("AcquisitionTime : %d\n" % tacq)
1082     settingsFile.write("SyncDivider : %d\n" % syncDivider)
1083     settingsFile.write("SyncTriggerEdge : %d\n" % syncTriggerEdge)
1084     settingsFile.write("SyncTriggerLevel : %d\n" % syncTriggerLevel)
1085     settingsFile.write("InputTriggerEdge : %d\n" % inputTriggerEdge)
1086     settingsFile.write("InputTriggerLevel : %d\n" % inputTriggerLevel)
1087     settingsFile.write("\nDelayStagePosition: "+findDelayStagePos(delayStage))
1088     settingsFile.write("\nMeasuring input rates...")
1089     # Note: after Init or SetSyncDiv allow 150 ms for valid count rate readings
1090     time.sleep(0.15)

1092     tryfunc(th260lib.TH260_GetSyncRate(ct.c_int(dev[0]), byref(syncRate)),
1093         "GetSyncRate")
1094     settingsFile.write("\nSyncrate=%ld/s\n" % syncRate.value)
1095     print("Syncrate=%ld/s\n" % syncRate.value)
```

```

1096 for i in range(0, numChannels.value):
1097     tryfunc(
1098         th260lib.TH260_GetCountRate(ct.c_int(dev[0]), ct.c_int(i), byref(countRate)), \
1099         "GetCountRate")
1100     settingsFile.write("Countrate[%ld]=%ld/s\n" % (i, countRate.value))
1101 # after getting the count rates you can check for warnings
1102 tryfunc(th260lib.TH260_GetWarnings(ct.c_int(dev[0]), byref(warnings)), "GetWarnings")
1103 if warnings.value != 0:
1104     th260lib.TH260_GetWarningsText(ct.c_int(dev[0]), warningstext, warnings)
1105     print("\n\r%s\n" % warningstext.value.decode("utf-8"))
1106 settingsFile.close()

1107 ###Actual measurement###
1108 print("Starting data collection for "+fileName)
1109 outputfile = open(fileName+'.out', "wb+")
1110 tryfunc(th260lib.TH260_StartMeas(ct.c_int(dev[0]), ct.c_int(tacq)), "StartMeas")
1111 while True:
1112     tryfunc(th260lib.TH260_GetFlags(ct.c_int(dev[0]), byref(flags)), "GetFlags")
1113
1114     if flags.value & FLAG_FIFOFULL > 0:
1115         print("\n\rFiFo Overrun!")
1116         stoptttr()
1117
1118     tryfunc(
1119         th260lib.TH260_ReadFiFo(ct.c_int(dev[0]), byref(buffer), TIREADMAX,
1120                                byref(nRecords)), \
1121         "ReadFiFo", measRunning=True
1122     )
1123
1124     if nRecords.value > 0:
1125         # We could just iterate through our buffer with a for loop, however,
1126         # this is slow and might cause a FIFO overrun. So instead, we shrinken
1127         # the buffer to its appropriate length with array slicing, which gives
1128         # us a python list. This list then needs to be converted back into
1129         # a ctype array which can be written at once to the output file
1130         outputfile.write((ct.c_uint*nRecords.value)(*buffer[0:nRecords.value]))
1131     else:
1132         tryfunc(th260lib.TH260_CTCStatus(ct.c_int(dev[0]), byref(ctcstatus)), \
1133                 "CTCStatus")
1134         if ctcstatus.value > 0:
1135             print("\n\rDone")
1136             stoptttr()
1137             break
1138         # within this loop you can also read the count rates if needed.
1139     outputfile.close()

1140
1141 ##### Functions filenames: #####
1142 def nDontOverwrite(FileName):
1143     n=1
1144     while FileName+'-{:03d}.out'.format(n) in os.listdir():
1145         n=n+1
1146     return n
1147
1148 def moveToFolder(folderName):
1149     try:
1150         os.mkdir(folderName)
1151     except:pass
1152     os.chdir(folderName)
1153
1154 ### Control Delay Stage ###
1155 def initializeStage():
1156     rm = visa.ResourceManager()

```

## Chapter 10. Code for "Preparation and decay of a single quantum of vibration at ambient conditions"

```
1156     rm.list_resources()
1157     delayStage= rm.open_resource('GPIO0::1::INSTR')
1158     return delayStage
1159 def findDelayStagePos(delayStage):
1160     return str(delayStage.query('1TP'))
1161 def moveDelayStage(delayStage, pos):
1162     delayStage.write('1PA'+str(pos))
1163     time.sleep(2)
1164     return
1165
1166 ##### TimeHarp DLL #####
1167
1168 th260lib.TH260_GetLibraryVersion(libVersion)
1169 print("Library version is %s" % libVersion.value.decode("utf-8"))
1170 if libVersion.value.decode("utf-8") != LIB_VERSION:
1171     print("Warning: The application was built for version %s" % LIB_VERSION)
1172
1173 ##### Finding and Opening Device: #####
1174 print("\nSearching for TimeHarp devices...")
1175 print("DevIdx      Status")
1176
1177 for i in range(0, MAXDEVNUM):
1178     retcode = th260lib.TH260_OpenDevice(ct.c_int(i), hwSerial)
1179     if retcode == 0:
1180         print(" %ld      S/N %s" % (i, hwSerial.value.decode("utf-8")))
1181         dev.append(i)
1182     else:
1183         if retcode == -1: # TH260_ERROR_DEVICE_OPEN_FAIL
1184             print(" %ld      no device" % i)
1185         else:
1186             th260lib.TH260_GetErrorString(errorString, ct.c_int(retcode))
1187             print(" %ld      %s" % (i, errorString.value.decode("utf8")))
1188 # In this demo we will use the first TimeHarp device we find, i.e. dev[0].
1189 if len(dev) < 1:
1190     print("No device available.")
1191     closeDevices()
1192     print("Using device #%ld" % dev[0])
1193     print("\nInitializing the device...")
1194
1195 # with internal clock
1196 tryfunc(th260lib.TH260_Initialize(ct.c_int(dev[0]), ct.c_int(mode)), "Initialize")
1197
1198 tryfunc(th260lib.TH260_GetHardwareInfo(dev[0], hwModel, hwPartno, hwVersion), \
1199         "GetHardwareInfo")
1200 print("Found Model %s Part no %s Version %s" % (hwModel.value.decode("utf-8"), \
1201         hwPartno.value.decode("utf-8"), hwVersion.value.decode("utf-8")))
1202
1203 tryfunc(th260lib.TH260_GetNumOfInputChannels(ct.c_int(dev[0]), byref(numChannels)), \
1204         "GetNumOfInputChannels")
1205 print("Device has %i input channels." % numChannels.value)
1206
1207 ##### Configuring Setting: #####
1208 print("\nUsing the following settings:")
1209 print("Mode          : %d" % mode)
1210 print("Binning         : %d" % binning)
1211 print("Offset          : %d" % offset)
1212 print("AcquisitionTime : %d" % tacq)
1213 print("SyncDivider     : %d" % syncDivider)
1214 if hwModel.value.decode("utf-8") == "TimeHarp 260 N":
```

```

1216     print("SyncTriggerEdge   : %d" % syncTriggerEdge)
1217     print("SyncTriggerLevel  : %d" % syncTriggerLevel)
1218     print("InputTriggerEdge   : %d" % inputTriggerEdge)
1219     print("InputTriggerLevel  : %d" % inputTriggerLevel)
1220 else:
1221     print("Unknown hardware model %s. Aborted." % hwModel.value.decode("utf-8"))
1222     closeDevices()

1224 tryfunc(th260lib.TH260_SetSyncDiv(ct.c_int(dev[0]), ct.c_int(syncDivider)),
1225         "SetSyncDiv")
1226 if hwModel.value.decode("utf-8") == "TimeHarp 260 N":
1227     tryfunc(
1228         th260lib.TH260_SetSyncEdgeTrg(ct.c_int(dev[0]), ct.c_int(syncTriggerLevel),\
1229                                     ct.c_int(syncTriggerEdge)),\
1230         "SetSyncEdgeTrg"
1231     )
1232     # we use the same input settings for all channels, you can change this
1233     for i in range(0, numChannels.value):
1234         retcode = th260lib.TH260_SetInputEdgeTrg(ct.c_int(dev[0]), ct.c_int(i),\
1235                                                  ct.c_int(inputTriggerLevel),\
1236                                                  ct.c_int(inputTriggerEdge))
1237         if retcode < 0:
1238             print("TH260_SetInputCFD error %d. Aborted." % retcode)
1239             closeDevices()

1240 tryfunc(th260lib.TH260_SetSyncChannelOffset(ct.c_int(dev[0]), ct.c_int(0)),\
1241         "SetSyncChannelOffset")

1244 for i in range(0, numChannels.value):
1245     tryfunc(
1246         th260lib.TH260_SetInputChannelOffset(ct.c_int(dev[0]), ct.c_int(i),\
1247                                              ct.c_int(0)),\
1248         "SetInputChannelOffset"
1249     )

1250 tryfunc(th260lib.TH260_SetBinning(ct.c_int(dev[0]), ct.c_int(binning)), "SetBinning")####
1252 tryfunc(th260lib.TH260_SetOffset(ct.c_int(dev[0]), ct.c_int(offset)), "SetOffset")####
1253 tryfunc(th260lib.TH260_GetResolution(ct.c_int(dev[0]), byref(resolution)),\
1254         "GetResolution")
1255 print("Resolution is %1.1lfps" % resolution.value)

1256 ##### Countrate and Warnings: #####
1258 print("\nMeasuring input rates...")

1260 # Note: after Init or SetSyncDiv allow 150 ms for valid count rate readings
1261 time.sleep(0.15)

1262 tryfunc(th260lib.TH260_GetSyncRate(ct.c_int(dev[0]), byref(syncRate)),
1263         "GetSyncRate")
1264 print("\nSyncrate=%ld/s" % syncRate.value)

1266 for i in range(0, numChannels.value):
1267     tryfunc(
1268         th260lib.TH260_GetCountRate(ct.c_int(dev[0]), ct.c_int(i), byref(countRate)),\
1269         "GetCountRate"
1270     )
1271     print("Countrate[%ld]=%ld/s" % (i, countRate.value))

1274 # after getting the count rates you can check for warnings
1275 tryfunc(th260lib.TH260_GetWarnings(ct.c_int(dev[0]), byref(warnings)), "GetWarnings")

```

## Chapter 10. Code for "Preparation and decay of a single quantum of vibration at ambient conditions"

---

```
1276 if warnings.value != 0:
1277     th260lib.TH260_GetWarningsText(ct.c_int(dev[0]), warningstext, warnings)
1278     print("\n\n%s" % warningstext.value.decode("utf-8"))
1280
1281 expName='Test'
1282 posList=[0.4,0.5,0.7,0.9,1.1,1.3,1.5,1.7,2.0]
1283 measurementNum=60
1284 cwd=os.getcwd()
1285 delayStage=initializeStage()
1286 for pos in posList:
1287     baseName=expName+'Pos{:03.2f}'.format(pos)
1288     os.chdir(cwd)
1289     moveToFolder(cwd+"\\ "+expName+'Pos{:03.2f}'.format(pos))
1290     moveDelayStage(delayStage, pos)
1291     fileName=nDontOverwrite(baseName)
1292     for i in range(measurementNum):
1293         fileName=baseName+'-{:03d}'.format(fileName)
1294         Measure(fileName, delayStage)
1295         fileName=fileName+1
1296
1297 closeDevices()
```

# 11 Jones calculus for "Bell Correlations between light and vibration"

In this appendix we provide an alternative model to the one presented in Ch. 7. In contrast with the published model, this one relies heavily on our physical intuition of how the experiment behaves, which detracts from its general validity. The advantage is that, by directly incorporating our expectation of what is occurring in the experiment, it allowed us to test potential sources of error, which was extremely valuable when building and troubleshooting the experiment.

In this section we explain how we model the experiment in order to obtain the fitting function for the CHSH parameter plotted in Fig. 2 of the main text. We first use Jones calculus to find the effect of the optical elements on the quantum state of the Stokes–anti-Stokes photon pair. We then consider how an ideal Bell state is modified by the inclusion of the most relevant experimental imperfections.

To make the link between optical elements and the corresponding mathematical operations more explicit, we describe the two time-bin modes in term of the associated polarisation of the Raman photons through the mapping implemented by the polarisation selective unbalanced interferometer:  $|E_s\rangle \rightarrow |V_s\rangle$ ;  $|E_a\rangle \rightarrow |V_a\rangle$  and  $|L_s\rangle \rightarrow |H_s\rangle$ ;  $|L_a\rangle \rightarrow |H_a\rangle$ .

## 11.0.1 Jones calculus to model the experiment

We use Jones calculus to find the operators representing the optical elements (VR and PBS) in the reduced Hilbert space with exactly one photon existing in two possible polarisations. Specifically, a variable retarder with the retardation axis along the vertical axis is represented by (up to a global phase)

$$M_{VR}(\theta) = \begin{pmatrix} e^{-i\theta/2} & 0 \\ 0 & e^{i\theta/2} \end{pmatrix} \quad (11.1)$$

where  $\theta$  is the phase retardation introduced between vertical and horizontal components. We also define the matrix for a polarizer  $M_{P+}$  with the transmission axis along the vertical

direction, and a polarizer  $M_{P-}$  with the transmission axis along the horizontal direction as

$$M_{P+} = \begin{pmatrix} 0 & 0 \\ 0 & 1 \end{pmatrix} \quad M_{P-} = \begin{pmatrix} 1 & 0 \\ 0 & 0 \end{pmatrix} \quad (11.2)$$

The matrix for a variable retarder oriented at an arbitrary angle  $\alpha$  with respect to vertical are then given by  $M_{VR}^\alpha(\theta) = R(-\alpha)M_{VR}(\theta)R(\alpha)$ , where  $R(\alpha)$  is the rotation matrix

$$R(\alpha) = \begin{pmatrix} \cos(\alpha) & \sin(\alpha) \\ -\sin(\alpha) & \cos(\alpha) \end{pmatrix} \quad (11.3)$$

We then find the total operator (in the Hilbert space with exactly one Stokes and one anti-Stokes photon) for the two variable retarders at  $45^\circ$  ( $\frac{\pi}{4}$  rad) acting on the Stokes and anti-Stokes fields by taking the tensor product

$$M_{VR}(\theta, \varphi) = M_{VR}^{\frac{\pi}{4}}(\theta) \otimes M_{VR}^{\frac{\pi}{4}}(\varphi) \quad (11.4)$$

The state after going through the variable retarders is transformed according to

$$\hat{\rho}_{out} = M_{VR}(\theta, \varphi) \hat{\rho}_{in} M_{VR}(\theta, \varphi)^\dagger \quad (11.5)$$

We define  $M_{P_{xy}}$  as the operator for a polarizer with the transmission along the  $x$  axis for the Stokes field and  $y$  axis for the anti-Stokes field. For example,  $M_{P_{-+}}$  is defined as  $M_{P_{-+}} \equiv M_{P_-} \otimes M_{P_+}$ .

We can then compute the expectation values of relevant observables for assessing the CHSH parameter, i.e.  $n_{xy} = \text{Tr}(\hat{\rho}_{out} M_{P_{xy}})$ . With the  $n_{xy}$  coefficients we can then calculate the correlation parameters as explained in the main text.

### 11.0.2 Corner density matrix

We present here the analytical solution for a special case that will appear multiple times in this section. We consider the case of a density matrix that only has non-zero elements in the corners, i.e.

$$\hat{\rho} = \begin{pmatrix} x_{11} & 0 & 0 & x_{14} \\ 0 & 0 & 0 & 0 \\ 0 & 0 & 0 & 0 \\ x_{41} & 0 & 0 & x_{44} \end{pmatrix} \quad (11.6)$$

corresponding to  $\hat{\rho} = x_{11}|H_s H_a\rangle\langle H_s H_a| + x_{44}|V_s V_a\rangle\langle V_s V_a| + x_{14}|H_s H_a\rangle\langle V_s V_a| + x_{41}|V_s V_a\rangle\langle H_s H_a|$ .

By using the methodology described above, we find that the values of the correlation parame-



ters are

$$\begin{aligned}
E\left(0, \frac{\pi}{4}\right) &= \frac{1}{\sqrt{2}} \\
E\left(0, -\frac{\pi}{4}\right) &= \frac{1}{\sqrt{2}} \\
E\left(\frac{\pi}{2}, \frac{\pi}{4}\right) &= -\frac{1}{\sqrt{2}} \left( \frac{x_{14} + x_{41}}{x_{11} + x_{44}} \right) \\
E\left(\frac{\pi}{2}, -\frac{\pi}{4}\right) &= \frac{1}{\sqrt{2}} \left( \frac{x_{14} + x_{41}}{x_{11} + x_{44}} \right)
\end{aligned} \tag{11.7}$$

And the visibility curves at  $\theta = 0$  and  $\theta = \pi/2$  are given by

$$\begin{aligned}
E(0, \varphi) &= \cos(\varphi) \\
E(\pi/2, \varphi) &= -\sin(\varphi) \left( \frac{x_{14} + x_{41}}{x_{11} + x_{44}} \right)
\end{aligned} \tag{11.8}$$

These expressions simplify further considering that  $x_{11} + x_{44} = \text{Tr}(\hat{\rho}) = 1$  for a density matrix. We can clearly see that a density matrix of this form will always have ideal visibility of unity for the  $\theta = 0$  curve, while the visibility of the  $\theta = \pi/2$  curve will depend on the off diagonal elements.

### 11.0.3 Unbalanced initial state

We first analyze the effect of having different weights between the two elements of a Bell state, i.e.  $|\psi\rangle = \frac{1}{\sqrt{2}}(\sqrt{1+\epsilon}|H_s H_a\rangle - \sqrt{1-\epsilon}|V_s V_a\rangle)$ , where  $\epsilon$  gives the imbalance between them. This state has the form described in section 11.0.2, and therefore

$$\begin{aligned}
E\left(\frac{\pi}{2}, \frac{\pi}{4}\right) &= -\frac{1}{\sqrt{2}} \sqrt{1-\epsilon^2} \\
E\left(\frac{\pi}{2}, -\frac{\pi}{4}\right) &= \frac{1}{\sqrt{2}} \sqrt{1-\epsilon^2}
\end{aligned} \tag{11.9}$$

An unequal splitting of power in our experiment, which leads to this type of asymmetry, will therefore reduce the visibility of the correlations when  $\varphi = \pi/2$ . It will also affect the measurement of the marginal state, and we use this in order to find our experimental  $\epsilon$ .

The marginal of this state is represented by  $\hat{\rho}_a = \frac{1+\epsilon}{2}|H_a\rangle\langle H_a| + \frac{1-\epsilon}{2}|V_a\rangle\langle V_a|$ . We calculate the difference between the expectation values at the two outputs of the measurement system,

$$\langle M_{P+} \rangle - \langle M_{P-} \rangle = \epsilon \cos(\varphi) \tag{11.10}$$

and fit this function to the difference between normalized count rates shown in Figure 2b of the main text. We find that for our experiment  $\epsilon = 0.027$ , which leads to a loss of visibility of 0.04%. In the following analysis we neglect this contribution.

#### 11.0.4 Pure initial state

We consider the pure entangled (and Bell correlated) state  $|\psi\rangle = \frac{1}{\sqrt{2}}(|H_s H_a\rangle + e^{i\phi}|V_s V_a\rangle)$ , which is represented by the density matrix

$$\hat{\rho} = \frac{1}{2} \left( |H_s H_a\rangle\langle H_s H_a| + |V_s V_a\rangle\langle V_s V_a| + e^{-i\phi}|H_s H_a\rangle\langle V_s V_a| + e^{i\phi}|V_s V_a\rangle\langle H_s H_a| \right) \quad (11.11)$$

This density matrix is of the type described in section 11.0.2, and therefore

$$\begin{aligned} E\left(\frac{\pi}{2}, \frac{\pi}{4}\right) &= -\frac{1}{\sqrt{2}} \cos(\phi) \\ E\left(\frac{\pi}{2}, -\frac{\pi}{4}\right) &= \frac{1}{\sqrt{2}} \cos(\phi) \end{aligned} \quad (11.12)$$

In our experiment  $\phi$ , the accumulated phase difference between the early and late states, could arise from differences in path lengths within the folded interferometer, or from birefringence in the optical elements (as discussed above). For the chosen measurement basis and settings, the maximum Bell inequality violation will be found with  $\phi = 0$  or  $\phi = \pi$ . When experimentally optimising the visibility of the two-photon interference, we choose to set the phase to  $\phi = \pi$ .

The visibility of the correlation parameter for  $\theta = \pi/2$  is determined by  $\cos(\phi)$ . This means that any deviation from  $\phi = 0$  or  $\phi = \pi$  translates into a reduced visibility of the two photon interference curve with  $\theta = \pi/2$ , compared to that with  $\theta = 0$ , as shown in Fig. 11.2. We can also discriminate between the states with  $\phi = 0$  or  $\phi = \pi$  by considering in which direction the curve obtained with  $\theta = \pi/2$  shifts compared to the one at  $\theta = 0$ , as illustrated in Fig. 11.1. By comparing with Fig. 2 of the main text we can claim that we are preparing a state close to  $|\Psi\rangle = \frac{1}{\sqrt{2}}(|H_s H_a\rangle - |V_s V_a\rangle) \equiv |\phi_-\rangle$ .

#### Upper bound on unwanted phase

In the experiment we observe a ratio between the two-photon interference visibility at  $\theta = \pi/2$  and that at  $\theta = 0$  of 0.814. If we attribute all the loss of visibility to a phase deviating away from  $\phi = \pi$  (assuming perfect temporal overlap and therefore pure state) we find that the phase must be within  $\phi = \pi \pm 0.620$  rad to be able to reproduce our results.

#### 11.0.5 Initial state with a mixed component

Another effect that can lead to a loss of visibility is an imperfect overlap after the second pass through the interferometer. If it does not perfectly undo the delay introduced by the first pass, the photons will not be perfectly indistinguishable in their temporal modes. This imperfect temporal overlap is too short for our detectors to resolve, but it makes partial information about the time bin of origin of the photons in principle available. This results in a mixed state as opposed to a pure entangled state. By mapping the time bin degree of freedom to

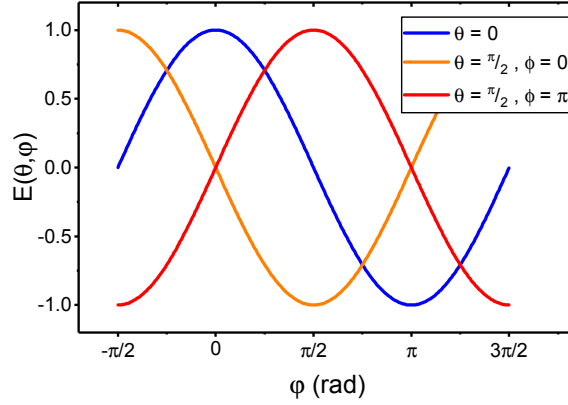


Figure 11.1: Calculated curves for the correlation parameter  $E$  inferred from a quantum state of the form  $|\psi\rangle = \frac{1}{\sqrt{2}}(|H_s H_a\rangle + e^{i\phi}|V_s V_a\rangle)$ , with different values of  $\phi$ . The curve obtained for  $\theta = 0$  does not depend on the phase  $\phi$ , while the curves computed for  $\theta = \pi/2$  let us distinguish  $|H_s H_a\rangle + |V_s V_a\rangle$  from  $|H_s H_a\rangle - |V_s V_a\rangle$ .

polarisation, our scheme produces pairs of photons that are either vertically or horizontally polarized before being overlapped. Therefore, we can write the general density matrix

$$\hat{\rho} = \lambda|\psi\rangle\langle\psi| + (1 - \lambda)\hat{\rho}_m$$

as a sum of the pure entangled state

$$|\psi\rangle = \frac{1}{\sqrt{2}}(|H_s H_a\rangle + e^{i\phi}|V_s V_a\rangle)$$

and a mixed state

$$\hat{\rho}_m = |H_s H_a\rangle\langle H_s H_a| + |V_s V_a\rangle\langle V_s V_a|$$

which results from the non-overlapping temporal modes.

This again leads to the case described in Sec. 11.0.2, with the correlation parameter for a fixed  $\theta = \pi/2$  being expressed by  $E(\pi/2, \varphi) = -\lambda \cos(\phi) \sin(\varphi)$ . Any mixed component from imperfect temporal overlap will therefore decrease the visibility, and the maximum CHSH parameter will only be obtained for the pure entangled state.

Experimentally, we cannot discriminate between the effect of an incorrect phase  $\phi \neq \pi$  that was discussed in Sec. 11.0.4, and imperfect temporal overlap. The two could in principle be distinguished by changing the measurement basis to one in which  $\phi = \pi/2$  gives a maximum CHSH violation, which would allow us to quantify the contribution of each effect. This would however entails a change in setup configuration and therefore in temporal overlap, so it is unlikely to yield a definite answer.

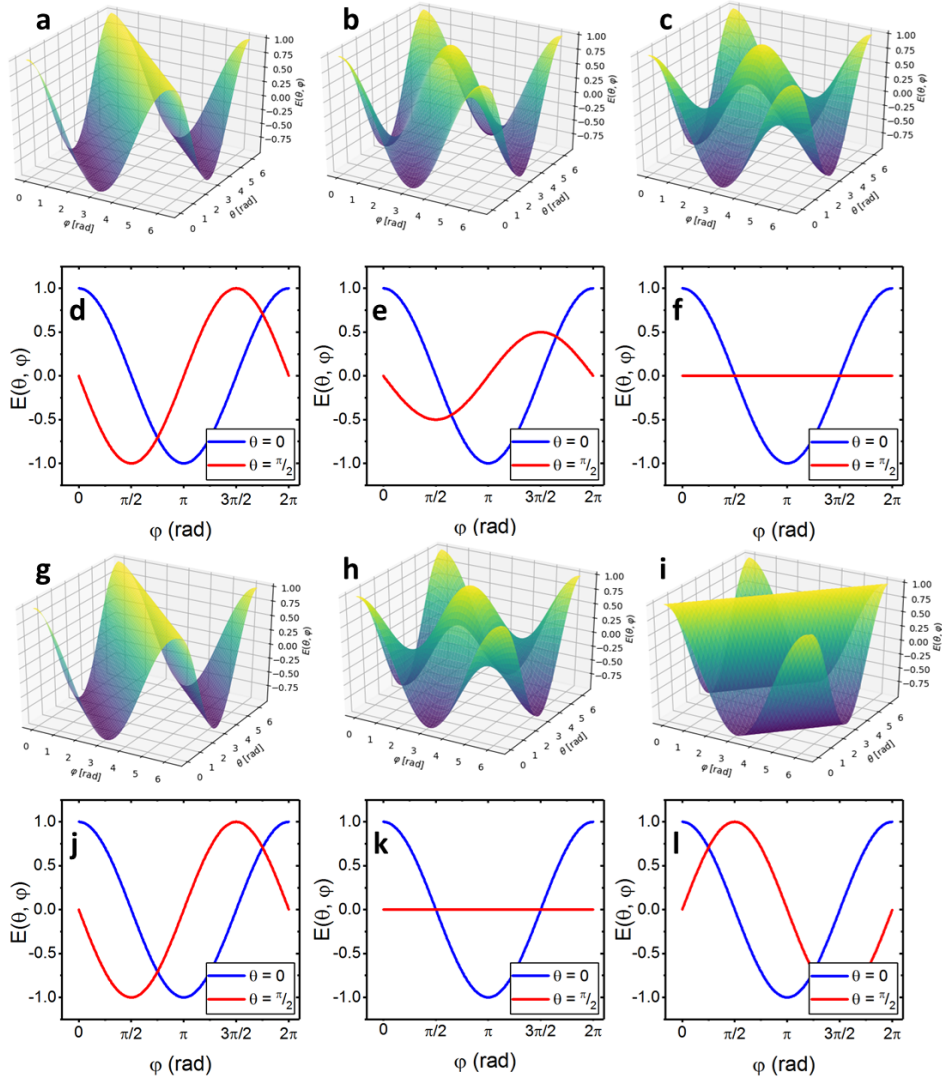


Figure 11.2: **Computed two-photon coincidence curves.** Panels **a-c** show the value of the correlation parameter  $E$  for the density matrix  $\hat{\rho} = \lambda|\phi_{-}\rangle\langle\phi_{-}| + (1 - \lambda)\hat{\rho}_m$  (see text). In **a**,  $\lambda = 1$  (pure state), while in **b**,  $\lambda = 1/2$  (partially mixed state), and in **c**,  $\lambda = 0$  (fully mixed state). The panels **d-f** show cuts at  $\theta = 0$  and  $\theta = \pi/2$  for the surface plots above them. Panels **g-i** show the value of the correlation parameter  $E$  for the pure state  $|\psi\rangle = \frac{1}{\sqrt{2}}(|H_s, H_a\rangle + e^{i\phi}|V_s, V_a\rangle)$ . In **g**,  $\phi = 0$ , while in **h**,  $\phi = \pi/2$ , and in **i**,  $\phi = \pi$ . Panels **j-l** again show cuts at  $\theta = 0$  and  $\theta = \pi/2$  for the surface plots above them.

With this complete model, we obtain the correlation parameters for the settings used to

---

compute the CHSH parameter

$$\begin{aligned}
E\left(0, \frac{\pi}{4}\right) &= E\left(0, -\frac{\pi}{4}\right) = \frac{1}{\sqrt{2}} \\
E\left(\frac{\pi}{2}, \frac{\pi}{4}\right) &= -\frac{1}{\sqrt{2}}\lambda \cos(\phi) \\
E\left(\frac{\pi}{2}, -\frac{\pi}{4}\right) &= \frac{1}{\sqrt{2}}\lambda \cos(\phi)
\end{aligned} \tag{11.13}$$

From which we derive the CHSH parameter

$$S = \sqrt{2}(1 + V_0) \tag{11.14}$$

where  $V_0 = \lambda \cos(\phi)$  is the loss of visibility due to the imperfect phase and temporal overlap, which is measured experimentally as the ratio of the amplitudes of the visibility curves at  $\theta = \pi/2$  and  $\theta = 0$ .

### Upper bound on mixed component

By considering the case in which all the loss of visibility between the  $\theta = 0$  and the  $\theta = \pi/2$  curve is due to a mixed component in the state, we can obtain a lower bound on the purity of the state. This lower bound is  $\lambda = 0.814$ .



## 12 Code for "Bell Correlations between light and vibration"

This appendix shows the code used to acquire and process the data shown in Ch. 7. The acquisition takes place as explained in Sec. 7.2.2, and is analyzed as explained in Sec. 7.2.13.

### 12.1 Code for data acquisition

```
1000 #Controls for the variable retarders, italian correlation card, and delay stage
1001 #VR calibration for OPO at 695nm and TiSa at 800nm
1002
1003 import time
1004 import sys
1005 import os
1006 import visa
1007 import subprocess
1008 import numpy as np
1009 import re
1010 import Exp_VisCurves_v2
1011
1012 #Variable retarder: #
1013 sys.path.append(r'C:\Program Files\ARCOptix\ARCOptix LC Driver 1.2\')
1014 import clr
1015 clr.AddReference("LCDriver")
1016 from ARCOptix.LCdriver import *
1017 import ctypes
1018 VR_CH0 = b'\x00'
1019 VR_CH1 = b'\x01'
1020
1021 def main():
1022     expName='DelaySweep3'
1023     repetitions=10
1024     thA1=np.pi/2
1025     thA2=0
1026     thB1=-np.pi/4
1027     thB2=np.pi/4
1028     expConditions=['0','1','1']#[seconds,minutes,number of meas for card]
1029     expPhases=[[thA1,thB1],
1030               [thA1,thB2],
```

## Chapter 12. Code for "Bell Correlations between light and vibration"

```
1032         [thA2, thB1],
1033         [thA2, thB2],
1034         [0, 0],
1035         [np.pi/2, np.pi/2]]
1036 print("Target phase configuration: ")
1037 print(expPhases)
1038 posList=[-0.20,-0.10,0.00,0.10,0.20,0.30,0.50,0.70,1.00,1.30,1.60,2.00,
1039          2.30,2.60,2.90,3.30,3.70,4.2]
1040 measurementNum=1
1041 LCD = initializeVR()
1042 delayStage=initializeStage()
1043 cwd=os.getcwd()
1044 for i in range(repetitions):
1045     os.chdir(cwd)
1046     Exp_VisCurves_v2.main()
1047     for pos in posList:
1048         baseName=expName+'Pos{:03.2f}'.format(pos)
1049         os.chdir(cwd)
1050         moveToFolder(cwd+"\\ "+expName+'Pos{:03.2f}'.format(pos))
1051         moveDelayStage(delayStage, pos)
1052         for phases in expPhases:
1053             fileName="{_thA_{:05.4f}_thB_{:05.4f}}".format(baseName,*phases)
1054             setPhase_S(LCD, VR_CH0, phases[0])
1055             setPhase_aS(LCD, VR_CH1, phases[1])
1056             MeasureCoincidenceNum(fileName, expConditions)
1057     os.chdir(cwd)
1058     return
1059
1060 ### Functions to control correlation card: ###
1061 def MeasureCoincidenceNum(fileName, expConditions):
1062     if fileName[-4:]==' .txt': fileName=fileName[:-4]
1063     fileName="{_{}_{}_s_{}_min_{}_acq.txt".format(fileName,*expConditions)
1064     fileName=dontOverride(fileName)
1065     cwd=os.getcwd()
1066     c_executable=r"C:\Users\Hamamatsu\Desktop\Release10\SaveCorrelationClient\TestClient.exe"
1067     file=cwd+"\\ "+fileName
1068     command=c_executable+' '+file+' '+ ' '.join(expConditions)
1069     subprocess.run(command)
1070     #print(command)
1071     print('Waiting for measurement '+fileName)
1072     wait((int(expConditions[0])+60*int(expConditions[1]))*int(expConditions[2]))
1073     outputFileName=fileName[:-4]+'-{:}.txt'.format(expConditions[2])
1074     checkFileExists(outputFileName)
1075     return
1076
1077 def dontOverride(fileName):
1078     'Returns a fileName that wont override existing files'
1079     if fileName[-4:]==' .txt': fileName=fileName[:-4]
1080     if re.compile(r'-.d\d\d').search(fileName[-4:])==None:
1081         fileName=fileName+'-001.txt'
1082     n=1
1083     while fileName[:-4]+'-1.txt' in os.listdir():
1084         fileName=fileName[:-7]+'{:03d}'.format(n)
1085         n=n+1
1086     return fileName
1087
1088 def wait(sleepTime):
1089     for i in range(int(sleepTime)):
```



```

time.sleep(1)
1092     return

1094 def checkFileExists(fileName):
    fileList=os.listdir()
1096     while fileName not in fileList:
        print('Measurement is taking longer than expected...')
1098         wait(1)
        fileList=os.listdir()
1100     print('Measurement done')
    return

1102
1103     ### Functions to control the Delay Stage: ###
1104 def initializeStage():
    rm = visa.ResourceManager()
1106     rm.list_resources()
    delayStage= rm.open_resource('GPIB0::1::INSTR')
1108     return delayStage
def findDelayStagePos(delayStage):
1110     return str(delayStage.query('1TP'))
def moveDelayStage(delayStage, pos):
1112     delayStage.write('1PA'+str(pos))
    time.sleep(2)
1114     return

1116
1117     ### Functions to control the Variable Retarder: ###
1118 def initializeVR():
    LCD = LCDriver(True)
1118     print("Number of connected devices: {}".format(LCD.GetNumberOfDevicesConnected()))
1120     print("Serial Number: {}".format(LCD.GetSerialNumber(0)))
    print("Max Voltage: {} V".format(LCD.GetMaxVoltage()))
1122     return LCD

1124 def setVRvol(LCD,CH,voltage, maxVoltage=8.3):
    if (voltage >= 0) and (voltage < maxVoltage):
1126         print('Changed Voltage: {}'.format(
            LCD.SetDACVoltage(float(voltage),CH,0)))
    else: print("Voltage not allowed")
1128     return

1130
1131 def setPhase(LCD,CH,phase):
1132     voltage=VRcalibration(phase)
    setVRvol(LCD,CH,voltage)
1134     return
def setPhase_S(LCD,CH,phase):
1136     voltage=VRcalibration_S(phase)
    setVRvol(LCD,CH,voltage)
1138     return
def setPhase_aS(LCD,CH,phase):
1140     voltage=VRcalibration_aS(phase)
    setVRvol(LCD,CH,voltage)
1142     return

1144 def VRcalibration(phase):
    'Returns the voltage required to set a given phase'
1146     minShift=-2.483311269
    maxShift=3.1415926540000001
1148     if (phase < minShift) or (phase > maxShift):
        print("WARNING: target phase shift outside range!")
1150     v_all=np.array([0,0.1,0.2,0.3,0.4,0.5,0.6,0.7,0.8,0.9,1,1.05,1.1,1.15,

```

## Chapter 12. Code for "Bell Correlations between light and vibration"

```
1152         1.2,1.25,1.3,1.35,1.4,1.45,1.5,1.55,1.6,1.65,1.7,1.75,
1153         1.8,1.85,1.9,1.95,2,2.05,2.1,2.15,2.2,2.25,2.3,2.35,2.4,
1154         2.45,2.5,2.6,2.7,2.8,2.9,3,3.1,3.2,3.3,3.4,3.5,3.6,3.7,
1155         3.8,4,4.2,4.4,4.6,4.8,5,5.4,5.8,6.2,6.6,7,7.4,7.8,8.2])
1156     ph_all=np. array([-2.483311269,-2.483311269,-2.483311269,-2.483311269,
1157                     -2.483311269,-2.483311269,-2.483311269,-2.483311269,
1158                     -2.459284667,-2.459284667,-2.3910858,-2.3275533,-2.229307863,
1159                     -2.120445443,-1.937145169,-1.747839158,-1.537954602,
1160                     -1.30808325,-1.069460949,-0.809925709,-0.553392756,
1161                     -0.319941777,0.232322341,0.404236443,0.633483795,0.87396484,
1162                     1.103195151,1.326585086,1.534967766,1.735722093,1.937145169,
1163                     2.113458937,2.267627813,2.464032367,2.623280734,2.752815115,
1164                     2.896641838,2.968603351,3.141592654,3.141592654,2.968603351,
1165                     2.715161634,2.588199898,2.413235043,2.299189813,2.155843614,
1166                     2.072131704,1.975808393,1.882671175,1.812387841,1.743303519,
1167                     1.679574588,1.629824536,1.584727142,1.471906664,1.392259533,
1168                     1.323085635,1.255048566,1.192745115,1.143761682,1.050034438,
1169                     0.972926175,0.900183781,0.847281298,0.794940488,0.753032308,
1170                     0.70915886,0.670204182])
1171     v=v_all[:39]
1172     ph=ph_all[:39]
1173     voltage=np. interp (phase,ph,v)
1174     return voltage
1175 def VRcalibration_S(phase):
1176     'Returns the voltage required to set a given phase for Stokes'
1177     minShift=-1.569926457
1178     maxShift=5.614910831
1179     if (phase < minShift) or (phase > maxShift):
1180         print("WARNING: target phase shift outside range!")
1181     v_all=np. array (
1182         [0,0.1,0.2,0.3,0.4,0.5,0.6,0.7,0.8,0.9,1,1.05,1.1,1.15,1.2,1.25,1.3,
1183         1.35,1.4,1.45,1.5,1.52,1.54,1.56,1.58,1.6,1.62,1.64,1.66,1.68,1.7,
1184         1.75,1.8,1.85,1.9,1.95,2,2.05,2.1,2.15,2.2,2.25,2.3,2.35,2.4,2.45,2.5,
1185         2.55,2.6,2.65,2.7,2.75,2.8,2.85,2.9,2.95,3,3.1,3.2,3.3,3.4,3.5,3.6,
1186         3.7,3.8,3.9,4,4.1,4.2,4.3,4.4,4.5,4.7,4.9,5.1,5.3,5.5,5.7,5.9,6.1,6.3,
1187         6.5,6.7,6.9,7.1,7.3,7.5,7.7,7.9,8.1,8.3])
1188     ph_all=np. array (
1189         [-1.569926457,-1.57880922,-1.575520108,-1.556040283,-1.555407578,
1190         -1.554190573,-1.547682201,-1.541705652,-1.526059772,-1.499987226,
1191         -1.427647686,-1.354768912,-1.255904124,-1.115275865,-0.943638581,
1192         -0.753732344,-0.546573435,-0.339762316,-0.158326014,0.198848036,
1193         0.409705667,0.501398952,0.596682684,0.687619608,0.778237172,
1194         0.871617989,0.963276224,1.054412127,1.145800867,1.239231172,
1195         1.322109726,1.540753059,1.757799229,1.956270301,2.156749094,
1196         2.34808006,2.520707301,2.647610611,2.776389665,2.906447291,
1197         3.141592654,3.259580566,3.263199597,3.413937887,3.51484494,
1198         3.595729535,3.692546995,3.780857241,3.846693884,3.93423095,
1199         3.998357168,4.059390236,4.122390242,4.181794329,4.239636168,
1200         4.286589138,4.332429929,4.419538859,4.503784161,4.572559323,
1201         4.643327118,4.703149509,4.753216418,4.808148311,4.852143668,
1202         4.901935078,4.939851431,4.979097352,5.013678059,5.046549668,
1203         5.077581515,5.103962872,5.155914572,5.207535179,5.252519517,
1204         5.295060208,5.324709157,5.359650041,5.387628798,5.415521192,
1205         5.444514664,5.468066246,5.491431134,5.514261272,5.535144039,
1206         5.549028467,5.567984243,5.58271833,5.597220129,5.61603158,5.614910831])
1207     v,ph=v_all , ph_all
1208     voltage=np. interp (phase,ph,v)
1209     return voltage
1210 def VRcalibration_aS(phase):
1211     'Returns the voltage required to set a given phase for anti-Stokes'
```

```

1212 minShift=-2.006954224
1213 maxShift=5.687018301
1214 if (phase < minShift) or (phase > maxShift):
1215     print("WARNING: target phase shift outside range!")
1216 v_all=np.array(
1217     [0,0.1,0.2,0.3,0.4,0.5,0.6,0.7,0.8,0.9,1,1.05,1.1,1.15,1.2,1.25,1.3,
1218     1.35,1.4,1.45,1.5,1.52,1.54,1.56,1.58,1.6,1.62,1.64,1.66,1.68,1.7,
1219     1.75,1.8,1.85,1.9,1.95,2,2.05,2.1,2.15,2.2,2.25,2.3,2.35,2.4,2.45,2.5,
1220     2.55,2.6,2.65,2.7,2.75,2.8,2.85,2.9,2.95,3,3.1,3.2,3.3,3.4,3.5,3.6,
1221     3.7,3.8,3.9,4,4.1,4.2,4.3,4.4,4.5,4.7,4.9,5.1,5.3,5.5,5.7,5.9,6.1,6.3,
1222     6.5,6.7,6.9,7.1,7.3,7.5,7.7,7.9,8.1,8.3])
1223 ph_all=np.array(
1224     [-2.006954224,-1.985707153,-1.990174204,-1.991619303,-1.993616454,
1225     -1.984128613,-1.990242997,-1.993892064,-1.982962568,-1.948314203,
1226     -1.90614004,-1.838029653,-1.758618063,-1.64272319,-1.479425599,
1227     -1.31400835,-1.127943469,-0.899213436,-0.688693271,-0.45303961,
1228     -0.293058257,-0.221995076,0.230399669,0.270460551,0.323697141,
1229     0.409129703,0.487163012,0.57974153,0.676240803,0.766917177,
1230     0.855334592,1.084365281,1.304186458,1.513764504,1.714277338,
1231     1.915737566,2.114896829,2.260128186,2.462002935,2.596685133,
1232     2.738598412,2.877452907,3.141592654,3.204016758,3.377008966,
1233     3.453717592,3.482137765,3.62612226,3.709695465,3.805534327,
1234     3.861382346,3.904283753,4.005422407,4.049239641,4.121340384,
1235     4.168068158,4.239233196,4.303785786,4.419461281,4.521368493,
1236     4.574175081,4.650474653,4.714852844,4.751996141,4.828776168,
1237     4.867524671,4.907021867,4.958343714,5.011914038,5.049092272,
1238     5.086356034,5.112546932,5.162207292,5.222784249,5.268609065,
1239     5.319370281,5.357598834,5.395016216,5.429683513,5.454295839,
1240     5.500193978,5.513104252,5.53964263,5.578434329,5.592615764,
1241     5.612687321,5.647535832,5.662072286,5.667273655,5.694218355,
1242     5.687018301])
1243 v,ph=v_all,ph_all
1244 voltage=np.interp(phase,ph,v)
1245 return voltage
1246
1247 ### Misc. Functions: ###
1248 def moveToFolder(folderName):
1249     try:
1250         os.mkdir(folderName)
1251     except:pass
1252     os.chdir(folderName)
1253     return
1254
1255 if __name__=="__main__": #execute only if run as script
1256     for i in range(1):
1257         main()

```

## 12.2 Code for data analysis

```

1000 #Analysis of Correlation Coefficients for a Bell test
1002 #Structure of result arrays: (results_X[i])
1004 #results_Bell:

```

## Chapter 12. Code for "Bell Correlations between light and vibration"

```
# [[time, Ea1b1, Ea1b2, Ea2b1, Ea2b2, S, S_error] ,...]
```

```
1006 #results_Aggregated (All results for the same pos and phases added)
```

```
1008 # [[time, thA, thB, n11, n12, n21, n22, E, E_error] ,...]
```

```
1010 #results_Disociated
```

```
1012 # [[time, repNum, thA, thB, n11, n12, n21, n22, E, E_error] ,...]
```

```
1012 #results_g2
```

```
1014 # [[time, thA, thB, g2_12, g2_12_err, g2_13, g2_13_err, g2_14, g2_14_err, g2_23,
```

```
1016 #   g2_23_err, g2_24, g2_24_err, g2_12_34, g2_12_34_err] ,...]
```

```
1016 import numpy as np
```

```
1018 import matplotlib.pyplot as plt
```

```
1020 import re
```

```
1020 import os
```

```
1022 def main():
```

```
1024     baseName = 'DelaySweep3'
```

```
1024     auxSettings = True
```

```
1026     # Bell Test Settings: #
```

```
1026     thA1=0
```

```
1028     thA2=np.pi/2
```

```
1028     thB1=np.pi/4
```

```
1030     thB2=-np.pi/4
```

```
1030     bellPhases=[[thA1, thB1],
```

```
1032                  [thA1, thB2],
```

```
1032                  [thA2, thB1],
```

```
1034                  [thA2, thB2]]
```

```
1034     if auxSettings: auxPhases = [[0,0],[np.pi/2]]
```

```
1036     cwd = os.getcwd()
```

```
1038     # Finding folders to analyse: #
```

```
1038     cwd = os.getcwd()
```

```
1040     folderNames, delayPositions = findFolders(baseName)
```

```
1040     delayTime=(delayPositions*2)/((3*10**8)*(10**3))*(10**12)
```

```
1042     results_Bell=[]
```

```
1042     results_Aggregated=[]
```

```
1044     results_Disociated=[]
```

```
1044     result_g2=[]
```

```
1046     for i in range(len(folderNames)):
```

```
1048         print(folderNames[i])
```

```
1048         os.chdir(cwd)
```

```
1050         os.chdir(cwd+'\\'+folderNames[i])
```

```
1050         #allDataPosX=readPosFiles(folderNames[i],delayTime[i])
```

```
1052         #AgregatedPosX=aggregateData(allDataPosX)
```

```
1052         #SPosX=BellAnalysis(AgregatedPosX, bellPhases)
```

```
1054         #g2 calculation:
```

```
1056         allDataPosX_allCHN = readPosFiles_allCHN(folderNames[i],delayTime[i])
```

```
1056         AggregatedPosX_allCHN = aggregateData_allCHN(allDataPosX_allCHN)
```

```
1058         g2PosX=g2Analysis(AgregatedPosX_allCHN, bellPhases)
```

```
1060         ##
```

```
1060         print("Folder Name: {}".format(folderNames[i]))
```

```
1062         print(AgregatedPosX_allCHN)
```

```
1062         ##
```

```
1064         #Merging results:
```

```

1066     #results_Disociated.append(allDataPosX)
1067     #results_Agregated.append(AgregatedPosX)
1068     #results_Bell.append(SPosX)
1069     result_g2.append(g2PosX)
1070     #results_Disociated = np.array(results_Disociated)
1071     #results_Agregated = np.array(results_Agregated)
1072     #results_Bell = np.array(results_Bell)
1073     result_g2 = np.array(result_g2)
1074
1075     os.chdir(cwd)
1076     #E_Stability(results_Disociated)
1077     #S_Stability(results_Disociated, bellPhases)
1078     #g2_Stability
1079     #VisCurves_Stability
1080     #saveFinalResult('resultsBell.txt', results_Bell)
1081     #saveAgregatedResults('resultsAgregated.txt', results_Agregated)
1082     #saveDisociatedResults('resultsDisociated.txt', results_Disociated)
1083     save_g2_results('results_g2.txt', result_g2)
1084
1085     #plt.show()
1086     return
1087
1088 def findE(Na1b1, Na1b2, Na2b1, Na2b2):
1089     return (Na1b1+Na2b2-Na1b2-Na2b1) / (Na1b1+Na1b2+Na2b1+Na2b2)
1090
1091 def readPosFiles(folder, time):
1092     fileNames, phases, num=findFiles(folder)
1093     allData=np.zeros((len(fileNames),10))
1094     allData[:,0]=time*np.ones(allData[:,0].shape)
1095     for i in range(len(fileNames)):
1096         data=np.genfromtxt(fileNames[i], skip_header=1)
1097         E=findE(data[5], data[6], data[7], data[8])
1098         E_error=findE_error(data[5:9])
1099         allData[i,1] = num[i]
1100         allData[i,2:4] = phases[i]
1101         allData[i,4:8] = data[5:9]
1102         allData[i,8] = E
1103         allData[i,9] = E_error
1104     return allData
1105     # [[time, repNum, thA, thB, n11, n12, n21, n22, E, E_error], ...]
1106
1107 def aggregateData(allData):
1108     phaseCombinations = []
1109     for data in allData:
1110         #print(data[2:4])
1111         if all((data[2:4] != phase).any() for phase in phaseCombinations):
1112             phaseCombinations.append(np.array(data[2:4]))
1113     phaseCombinations = np.array(phaseCombinations)
1114
1115     aggregatedData=np.zeros((len(phaseCombinations),9))
1116     aggregatedData[:,0]=allData[0,0]*np.ones(aggregatedData[:,0].shape)
1117
1118     for i in range(len(phaseCombinations)):
1119         aggregatedData[i,1:3]=phaseCombinations[i]
1120         for data in allData:
1121             if (data[2:4]==phaseCombinations[i]).all():###
1122                 aggregatedData[i,3:7]=aggregatedData[i,3:7]+data[4:8]
1123         E=findE(aggregatedData[i,3], aggregatedData[i,4], aggregatedData[i,5],
1124               aggregatedData[i,6])

```

## Chapter 12. Code for "Bell Correlations between light and vibration"

```

    E_error=findE_error(agregatedData[i,3:7])
1126     agregatedData[i,7]=E
        agregatedData[i,8]=E_error
1128     return agregatedData
# [[time,thA,thB,n11,n12,n21,n22,E,E_error],...]
1130
def BellAnalysis(agregatedData,bellPhases):
1132     results = np.zeros(7)
    results[0] = agregatedData[0,0]
1134     Setting_counts=np.zeros((4,4))
    phaseExists=True
1136     for i in range(len(bellPhases)):
        phase=bellPhases[i]
1138         if phaseExists==False: print("Warning: Phase setting not found!\n")
        for data in agregatedData:
1140             phaseExists=False
            #if data[1]==phase[0] and data[2]==phase[1]:
1142             if np.isclose(data[1],phase[0],atol=1e-4) and \
                np.isclose(data[2],phase[1],atol=1e-4):
1144                 Setting_counts[i,:]=data[3:7]
                results[i+1]=data[7]
1146                 phaseExists=True
                break
1148         if phaseExists==False: print("Warning: Phase setting not found!\n")
    S,S_err=Scalculatoin(Setting_counts)
1150     results[5:7]=S,S_err
    return results
1152 # [[time,Ea1b1,Ea1b2,Ea2b1,Ea2b2,S,S_error],...]

1154 def findFolders(baseName):
    folderRegex=re.compile('('+baseName+r'Pos')([-]?\d+[.]?\d*)')
1156     directoryContent=os.listdir()
    folderNames=[]
1158     delays=[]
    for name in directoryContent:
1160         match=folderRegex.search(name)
        if match!=None:
1162             folderNames.append(name)
            delays.append(float(match.group(2)))
1164     return folderNames,np.array(delays)

1166 def findFiles(folder):
    fileRegex=re.compile('('+folder+r'_thA_')([-]?\d[.]\d{4})(_thB_')([-]?\d[.]\d{4})_d*s_\d*min_\d*acq
-((\d{3})-\d*.txt)')
1168     directoryContent=os.listdir()
    fileNames=[]
1170     phases=[]
    num=[]
1172     for name in directoryContent:
        match=fileRegex.search(name)
1174         if match!=None:
            fileNames.append(name)
1176             phases.append([float(match.group(2)),float(match.group(4))])
            num.append(match.group(5))
1178     return np.array(fileNames),np.array(phases),np.array(num)

1180
##### Error Barr calculation : #####
1182 def Scalculatoin(expCounts,n_iter_max=3000,conv=1e-5):
    S,std,results=monteCarloError_S(expCounts,n_iter_max,conv)
```

```

1184     #plot_error_histogram(results)
1185     return S, std
1186
1187 def findS(Counts):
1188     E_array=np.array(
1189         [findE(Counts[i,0],Counts[i,1],Counts[i,2],Counts[i,3])
1190          for i in range(4)])
1191     #print(E_array)
1192     S=E_array[0]+E_array[1]-E_array[2]+E_array[3]
1193     return S
1194
1195 def monteCarloError_S(expCounts, n_iter_max=1000, conv_crit=1e-5):
1196     expS=findS(expCounts)
1197     n_iter=0
1198     conv_S=1
1199     conv_std=1
1200     S_avg_prev=999
1201     std_prev=999
1202     S_array=[]
1203     while ((abs(conv_S)>abs(conv_crit) or abs(conv_std)>abs(conv_crit))
1204            and (n_iter < n_iter_max)):
1205         perturbCounts=PoissonianPerturbation(expCounts)
1206         S_current=findS(perturbCounts)
1207         S_array.append(S_current)
1208
1209         conv_S=1-np.average(S_array)/S_avg_prev
1210         conv_std=1-np.std(S_array)/std_prev
1211
1212         S_avg_prev=np.average(S_array)
1213         if n_iter != 0:
1214             std_prev=np.std(S_array)
1215             n_iter=n_iter+1
1216
1217     if n_iter == n_iter_max:
1218         print("WARNING: Maximum number of iterations reached!")
1219     std=np.std(S_array)
1220     print("Finished with conv_S = {}, conv_std = {} after {} \
1221 iterations\n".format(conv_S, conv_std, n_iter))
1222     return expS, std, np.array(S_array)
1223
1224 def PoissonianPerturbation(expCounts):
1225     perturbCounts=np.array(
1226         [[np.random.poisson(expCounts[i,j],1)[0]
1227          for j in range(len(expCounts[0,:]))]
1228          for i in range(len(expCounts[:,0]))])
1229     return perturbCounts
1230
1231 def findS(Counts):
1232     E_array=np.array(
1233         [findE(Counts[i,0],Counts[i,1],Counts[i,2],Counts[i,3])
1234          for i in range(4)])
1235     #print(E_array)
1236     S=E_array[0]+E_array[1]+E_array[2]-E_array[3]
1237     return S
1238
1239 def plot_error_histogram(results):
1240     Fig,ax=plt.subplots(1,1)
1241     ax.hist(results, bins=20)
1242     ax.set_xlabel('S')
1243     ax.set_ylabel('# of trials')

```

## Chapter 12. Code for "Bell Correlations between light and vibration"

```
1244     ax.set_title('Monte Carlo trials')
1245     return
1246
1248 def findE_error(expCounts, n_iter_max=1000, conv_crit=1e-5):
1249     try: #Making sure the shape is [[x,x,x,x]]
1250         tmp=expCounts[0,0]
1251     except: expCounts=np.array([expCounts])
1252     expE=findE(expCounts[0,0], expCounts[0,1], expCounts[0,2], expCounts[0,3])
1253     n_iter=0
1254     conv_E=1
1255     conv_std=1
1256     E_avg_prev=999
1257     std_prev=999
1258     E_array=[]
1259     while ((abs(conv_E)>abs(conv_crit) or abs(conv_std)>abs(conv_crit))
1260            and (n_iter < n_iter_max)):
1261         perturbCounts=PoissonianPerturbation(expCounts)
1262         E_current=findE(perturbCounts[0,0], perturbCounts[0,1],
1263                        perturbCounts[0,2], perturbCounts[0,3])
1264         E_array.append(E_current)
1265
1266         conv_E=1-np.average(E_array)/E_avg_prev
1267         conv_std=1-np.std(E_array)/std_prev
1268
1269         E_avg_prev=np.average(E_array)
1270         if n_iter != 0:
1271             std_prev=np.std(E_array)
1272         n_iter=n_iter+1
1273
1274     #if n_iter == n_iter_max:
1275         #print("WARNING: Maximum number of iterations reached!")
1276     std=np.std(E_array)
1277     #print("Finished with conv_E = {}, conv_std = {} after {} \
1278 #iterations\n".format(conv_E, conv_std, n_iter))
1279     return std#expE, std, np.array(E_array)
1280
1281 ##### g2 calculation #####
1282 def g2Analysis(aggregatedData, bellPhases):
1283     results = np.zeros(3)
1284     results[0] = aggregatedData[0,0]
1285     SingleCHN_counts=np.zeros(4)
1286     coincidence_counts=np.zeros(4)
1287     phaseExists=True
1288     for i in range(len(bellPhases)):
1289         phase=bellPhases[i]
1290         if phaseExists==False: print("Warning: Phase setting not found!\n")
1291         for data in aggregatedData:
1292             phaseExists=False
1293             if np.isclose(data[1], phase[0], atol=1e-4) and \
1294                np.isclose(data[2], phase[1], atol=1e-4):
1295                 SingleCHN_counts = data[3:7]
1296                 coincidence_counts = data[8:12]
1297                 phaseExists=True
1298                 break
1299         if phaseExists==False: print("Warning: Phase setting not found!\n")
1300     g2, g2_err = find_g2(SingleCHN_counts, coincidence_counts)
1301     results[1:]=g2, g2_err
1302     return results
```



```

1304 # [[time, g2, g2_Err], ...]
1306
1307 def readPosFiles_allCHN(folder, time):
1308     fileNames, phases, num = findFiles(folder)
1309     allData = np.zeros((len(fileNames), 19))
1310     allData[:, 0] = time * np.ones(allData[:, 0].shape)
1311     for i in range(len(fileNames)):
1312         data = np.genfromtxt(fileNames[i], skip_header=1)
1313         allData[i, 1] = num[i]
1314         allData[i, 2:4] = phases[i]
1315         allData[i, 4:] = data[:, 1:]
1316     return allData
1317 # [[time, repNum, thA, thB, n1, n2, n3, n4, n12, n13, n14, n23, n24, n34, n123, n124, n134, n234, n1234], ...]
1318
1319 def aggregateData_allCHN(allData):
1320     phaseCombinations = []
1321     for data in allData:
1322         #print(data[2:4])
1323         if all((data[2:4] != phase).any() for phase in phaseCombinations):
1324             phaseCombinations.append(np.array(data[2:4]))
1325     phaseCombinations = np.array(phaseCombinations)
1326     aggregatedData = np.zeros((len(phaseCombinations), 18))
1327     aggregatedData[:, 0] = allData[:, 0] * np.ones(aggregatedData[:, 0].shape)
1328     for i in range(len(phaseCombinations)):
1329         aggregatedData[i, 1:3] = phaseCombinations[i]
1330         for data in allData:
1331             if (data[2:4] == phaseCombinations[i]).all(): ###
1332                 aggregatedData[i, 3:18] = aggregatedData[i, 3:18] + data[4:19]
1333     return aggregatedData
1334 # [[time, thA, thB, n1, n2, n3, n4, n12, n13, n14, n23, n24, n34, n123, n124, n134, n234, n1234], ...]
1335
1336 def find_g2(SingleCounts, Coincidences, aq_time=240):
1337     rep_rate = 80.7e6
1338     S_tot = SingleCounts[0] + SingleCounts[1]
1339     aS_tot = SingleCounts[2] + SingleCounts[3]
1340     coinc_tot = np.sum(Coincidences)
1341     g2 = ((coinc_tot) / (S_tot * aS_tot)) * rep_rate * aq_time
1342     g2_err = g2 * np.sqrt((1 / coinc_tot) + (1 / S_tot) + (1 / aS_tot))
1343     return g2, g2_err
1344
1345 ##### Stability information #####
1346 def E_Stability(results):
1347     #Finding list of repetitions:
1348     rep_list = []
1349     for pos in results:
1350         for meas in pos:
1351             if meas[1] not in rep_list:
1352                 rep_list.append(meas[1])
1353     rep_list = np.array(rep_list)
1354
1355     color_idx = np.linspace(0, 1, len(rep_list))
1356
1357     #Finding phase settings:
1358     ph_pairs_list = []
1359     for pos in results:
1360         for meas in pos:
1361             if all((meas[2:4] != phase).any() for phase in ph_pairs_list):
1362                 ph_pairs_list.append(np.array(meas[2:4]))
1363     ph_pairs_list = np.array(ph_pairs_list)

```

## Chapter 12. Code for "Bell Correlations between light and vibration"

```
1364 #Creating fig and axes (in two cols) correlated to a phase setting:
1366 fig, axarr=plt.subplots(int(np.ceil(len(ph_pairs_list)/2)),2)
1368 ph_pair_ax_array=np.array(
    [[ph_pairs_list[i,0], ph_pairs_list[i,1], axarr[int(i/2),i%2]]
     for i in range(len(ph_pairs_list))])
1370
1372 for pos in results:
1374     for meas in pos:
1376         for ph in ph_pair_ax_array:
1378             if meas[2] == ph[0] and meas[3] == ph[1]:
1380                 ph[2].errorbar(
1382                     meas[0],meas[8],meas[9],fmt='o',capsize=3,
1384                     c = plt.cm.winter(
1386                         color_idx[rep_list.tolist().index(meas[1])])
1388 for i in range(len(ph_pair_ax_array)):
1390     ph_pair_ax_array[i,2].set_title(
1392         "phA = {:} , phB = {}".format(*ph_pair_ax_array[i,:2]))
1394 fig.suptitle("Stability information")
1396 #savefig
1398 return
1400
1402 def S_Stability(results, bellPhases):
1404     #Finding list of repetitions:
1406     rep_list = []
1408     S_stab_res = []
1410     for pos in results:
1412         for meas in pos:
1414             if meas[1] not in rep_list:
1416                 rep_list.append(meas[1])
1418     rep_list=np.array(rep_list)
1420     color_idx=np.linspace(0,1,len(rep_list))
1422     fig,ax=plt.subplots(1,1)
1424     for pos in results:
1426         for rep in rep_list:
1428             repData=np.array([[meas[0],*meas[2:]]
1430                             for meas in pos if meas[1]==rep])
1432             #print(repData)
1434             try: #accounts for different number of repetitions in diff positions
1436                 resBell=BellAnalysis(repData, bellPhases)
1438                 ax.errorbar(resBell[0],resBell[5],resBell[6],fmt='o',capsize=3,
1440                             c = plt.cm.winter(color_idx[
1442                                 rep_list.tolist().index(rep)])
1444                 S_stab_res.append([resBell[0],rep,*resBell[1:]])
1446             except: pass
1448     fig.suptitle("S stability information")
1450     saveSStabilityResults("S_stability.txt",S_stab_res)
1452     #savefig
1454     return
1456 #results_Disociated
1458 # [[time, repNum, thA, thB, n11, n12, n21, n22, E, E_error] , ...]
1460
1462 #Bell Results:
1464 # [[time, Ea1b1, Ea1b2, Ea2b1, Ea2b2, S, S_error] , ...]
1466
1468 ##### Saving Text Files #####
1470 def saveFinalResult(name, Results, thA1=0, thA2=np.pi/2, thB1=np.pi/4,
1472                     thB2=-np.pi/4):
1474     info='Results for a1={:05.4f}, a2={:05.4f}, b1={:05.4f},\
1476         b2={:05.4f}\n'.format(thA1, thA2, thB1, thB2)
```

```

1424     cols='DelayTime(ps)\tEa1b1\tEa1b2\tEa2b1\tEa2b2\tS\tS_error\n'
1425     headerStr=info+cols
1426     np.savetxt(name, Results, delimiter='\t', header=headerStr, newline='\r\n')
1427     return
1428
1429 def saveAgregatedResults(name, Results):
1430     reshaped=[] #result must be saved as a 2d array
1431     for pos in Results:
1432         for meas in pos:
1433             reshaped.append(meas)
1434     headerStr='time\tthA\tthB\tn11\tn12\tn21\tn22\tE\tE_error\n'
1435     np.savetxt(name, reshaped, delimiter='\t', header=headerStr, newline='\r\n')
1436     return
1437
1438 def saveDisociatedResults(name, Results):
1439     Results=np.array(Results)
1440     reshaped=[]
1441     for pos in Results:
1442         for meas in pos:
1443             reshaped.append(meas)
1444     headerStr='time\trepNum\tthA\tthB\tn11\tn12\tn21\tn22\tE\tE_error\n'
1445     np.savetxt(name, reshaped, delimiter='\t', header=headerStr, newline='\r\n')
1446     return
1447
1448 def saveSStabilityResults(name, Results, thA1=0, thA2=np.pi/2, thB1=np.pi/4,
1449                             thB2=-np.pi/4):
1450     info='Stability results for a1={:05.4f}, a2={:05.4f}, b1={:05.4f},\
1451     b2={:05.4f}\r\n'.format(thA1, thA2, thB1, thB2)
1452     cols='DelayTime(ps)\tRepNum\tEa1b1\tEa1b2\tEa2b1\tEa2b2\tS\tS_error\n'
1453     headerStr=info+cols
1454     np.savetxt(name, Results, delimiter='\t', header=headerStr, newline='\r\n')
1455     return
1456
1457 def save_g2_results(name, Results):
1458     headerStr='time\tg2\tg2_err\r\n'
1459     np.savetxt(name, Results, delimiter='\t', header=headerStr, newline='\r\n')
1460     return
1461
1462 if __name__=="__main__":
1463     main()

```



# 13 Numerical model for "Collective Vibrational Quantum Coherence in Spontaneous Raman Scattering"

This appendix shows the code used to model the results shown in Ch. 5.

```
1000 import numpy as np
1001 import matplotlib.pyplot as plt
1002 import qutip as qt

1004 def main():
1005     t0_R_values= np.linspace(0,20,60)
1006     g2_ideal_values = []
1007     g2_real_values = []
1008     for t0_R in t0_R_values:
1009         g2_ideal, g2_real = g2(t0_R)
1010         g2_ideal_values.append(g2_ideal)
1011         g2_real_values.append(g2_real)
1012     Fig,ax=plt.subplots(1,1)
1013     ax.plot(t0_R_values, g2_real_values)
1014     Fig.suptitle("Realistic Detection")

1016     t_exp = -4.5+np.array([6.33333, 6.46667, 4.0, 5.33333, 6.0, 6.66667, 7.33333, 8.0, 8.66667,
1017     9.33333, 10.0, 10.66667, 11.33333, 12.0, 12.66667, 13.33333, 14.0, 14.66667, 15.33333, 16.0,
1018     16.66667, 17.33333, 18.0, 18.66667, 19.33333, 20.0, 20.66667, 21.33333, 22.0, 22.66667,
1019     23.33333, 24.0, 24.66667, 25.33333, 26.0, 26.66667, 6.8, 7.0, 7.66667, 8.33333, 9.0])
1020     g2_exp = (1/1.13)*np.array([2.68364, 3.17592, 1.13028, 1.24126, 1.53424, 3.28627, 2.26673,
1021     1.66663, 1.56197, 1.68411, 1.81954, 1.84657, 1.65895, 1.52434, 1.45698, 1.51444, 1.55709,
1022     1.46913, 1.49168, 1.43269, 1.48734, 1.39537, 1.40791, 1.40163, 1.33711, 1.36824, 1.3717,
1023     1.36602, 1.35518, 1.29194, 1.30265, 1.21828, 1.27087, 1.27272, 1.3025, 1.29854, 2.96373, 2.582,
1024     1.90601, 1.55667, 1.57542])
1025     g2_exp_error = [0.09043, 0.10422, 0.04542, 0.04867, 0.05731, 0.10804, 0.08002, 0.06429,
1026     0.05968, 0.06509, 0.06765, 0.06727, 0.06236, 0.05934, 0.05729, 0.05811, 0.05923, 0.05743,
1027     0.05836, 0.0564, 0.05794, 0.05597, 0.05706, 0.0565, 0.0535, 0.05367, 0.05359, 0.05416, 0.0549,
1028     0.0522, 0.05143, 0.04929, 0.05165, 0.05267, 0.05344, 0.05352, 0.09859, 0.08822, 0.07085,
1029     0.05988, 0.06125]
1030     ax.scatter(t_exp, g2_exp)
1031     ax.set_xlim(0,20)

1033     Fig,ax=plt.subplots(1,1)
1034     ax.plot(t0_R_values, g2_ideal_values)
1035     Fig.suptitle("Ideal Detection")

1037     print(t0_R_values)
```

## Chapter 13. Numerical model for "Collective Vibrational Quantum Coherence in Spontaneous Raman Scattering"

```

1028     print(g2_real_values)
1029     print(g2_ideal_values)
1030     plt.show()
1031
1032 def g2(t0_R):
1033     ##### Model Inputs: #####
1034
1035     N=3          #Dimensionality for each Fock space (all currently share the same)
1036     t=np.linspace(0,30,12000) #Time steps for calculation
1037
1038     ### Laser parameters: ###
1039     A_W=1         #Amplitude Write pulse (for now all controlled through coupling)
1040     sig_W=0.2     #Bandwidth of Write Pulse
1041     t0_W=2        #Arrival time of Write Pulse
1042
1043     A_R=1         #Amplitude Read pulse (for now all controlled through coupling)
1044     sig_R=0.2     #Bandwidth of Read Pulse
1045
1046     ### Phonon parameters: ###
1047     w_b1=19.666*2*np.pi #Frequency of b1
1048     w_b2=19.397*2*np.pi #Frequency of b2
1049     nth = 0.04         #Phonon occupancy at room temperature
1050
1051     ### Interaction parameters: ###
1052     lamda_W=1.04E-1     #Coupling parameter for Write pulse
1053     lamda_R=1.36E-1     #Coupling parameter for Read pulse
1054     lamda_FWM = 1.0E-2  #Coupling parameter for the coherent process
1055     b1_coeff = np.sqrt(1/3) #Parameter giving ratio of b1 vs b2 creation
1056     b2_coeff = np.sqrt(2/3) #Parameter giving ratio of b1 vs b2 creation
1057     theta=np.pi/6       #Phase shift during interaction
1058
1059     ### Detection parameters: ###
1060     eta_S=0.1           #Detection efficiency for Stokes
1061     pdc_S=2.6E-4#0      #Probability of dark count for Stokes
1062     eta_aS=0.1          #Detection efficiency for anti-Stokes
1063     pdc_aS=1.04E-4#0    #Probability of dark count for anti-Stokes
1064     expOrder = 10      #Expansion order for the realistic detection operator
1065
1066     ##### Intermediate calculations: #####
1067
1068     del_S = -1 * (w_b1+w_b2)/2 #Stokes frequency difference
1069     del_aS = (w_b1+w_b2)/2    #Anti-Stokes frequency difference
1070     del_W = 0
1071     del_R = 0
1072     W=gaussianPulse(A_W, t, t0_W, sig_W,del_W) #Write Pulse
1073     R=gaussianPulse(A_R, t, t0_R, sig_R,del_R) #Read Pulse
1074
1075     ##### Model: #####
1076
1077     ### Initial Quantum State: ###
1078     psi0_ph1 = qt.thermal_dm(N,nth) #Initial state phonon 1
1079     psi0_ph2 = qt.thermal_dm(N,nth) #Initial state phonon 2
1080     psi0_S = qt.fock_dm(N,0)        #Initial state Stokes
1081     psi0_aS = qt.fock_dm(N,0)       #Initial state anti-Stokes
1082     psi0=qt.tensor(psi0_ph1,psi0_ph2,psi0_S,psi0_aS) #Initial State of the system
1083
1084     ### Creation/Anihilation Operators: ###
1085     b1 = qt.tensor(qt.destroy(N), qt.qeye(N), qt.qeye(N), qt.qeye(N)) #phonon1 annihilation

```

```

1088 n_b1 = [b1.dag()*b1]
1090 b2 = qt.tensor( qt.qeye(N), qt.destroy(N), qt.qeye(N), qt.qeye(N)) #phonon2 annihilation
1092 n_b2 = [b2.dag()*b2]
1094 c_S = qt.tensor(qt.qeye(N), qt.qeye(N), qt.destroy(N), qt.qeye(N)) #stokes annihilation
1096 c_aS = qt.tensor(qt.qeye(N),qt.qeye(N), qt.qeye(N), qt.destroy(N)) #anti-stokes annihilation
1098 ### Photon Number operators: ###
1099 n_S = [c_S.dag()*c_S]
1100 n_aS = [c_aS.dag()*c_aS]
1101 n_S_aS = [c_S.dag()*c_aS.dag()*c_aS*c_S]
1102
1103 #Hamiltonian
1104 H_I_W = [[lamda_W * b1_coeff * c_S.dag() * b1.dag(),W],
1105           [lamda_W * b1_coeff * c_S * b1,W.conj()]] \
1106           +[[lamda_W * b2_coeff * c_S.dag() * b2.dag(),W*np.exp(-1j*theta)],
1107             [lamda_W * b2_coeff * c_S * b2,W.conj()*np.exp(-1j*theta).conj()]]
1108
1109 H_I_R = [[lamda_R * b1_coeff * c_aS.dag() * b1,R],
1110           [lamda_R * b1_coeff * c_aS * b1.dag(),R.conj()]] \
1111           +[[lamda_R * b2_coeff * c_aS.dag() * b2,R],
1112             [lamda_R * b2_coeff * c_aS * b2.dag(),R.conj()]]
1113
1114 H_FWM = [[lamda_FWM * c_S.dag() * c_aS.dag(), W * R],
1115           [lamda_FWM * c_S * c_aS, W.conj() * R.conj()]]
1116
1117 H = [w_b1*n_b1[0]] + [w_b2*n_b2[0]] + [del_S*n_S[0]] + [del_aS*n_aS[0]]\
1118      + H_I_W \
1119      + H_I_R \
1120      + H_FWM
1121
1122
1123
1124 # collapse operator that describes dissipation
1125 # Build collapse operators for the thermal bath
1126 kappa1 = 1/8.4
1127 kappa2 = 1/1.7
1128 c_ops = []
1129 c_ops.append(np.sqrt(kappa1 * (1 + nth)) * b1)
1130 c_ops.append(np.sqrt(kappa1 * nth) * b1.dag())
1131 c_ops.append(np.sqrt(kappa2 * (1 + nth)) * b2)
1132 c_ops.append(np.sqrt(kappa2 * nth) * b2.dag())
1133 # c_ops = [] # no decay
1134
1135 result=qt.mesolve(H, psi0, t, c_ops, [], options=qt.Options(nsteps=1000))
1136
1137
1138 print("\nFor t0_R = "+str(t0_R))
1139 print(result)
1140 g2 =qt.expect(n_S_aS,result.states[-1])/(qt.expect(n_S,result.states[-1])*qt.expect(n_aS,
1141 result.states[-1]))
1142 try:
1143     g2_ideal = g2_CrossCor_ideal(c_S,c_aS,result.states[-1])
1144 except:
1145     g2_ideal = -1
1146 g2_real = g2_CrossCor_realistic(eta_S,pdc_S,c_S,eta_aS,pdc_aS,c_aS,result.states[-1],expOrder)

```

## Chapter 13. Numerical model for "Collective Vibrational Quantum Coherence in Spontaneous Raman Scattering"

```

1148     print("g2 = "+str(g2))
1149     print("g2 Ideal = "+str(g2_ideal))
1150     print("g2 Real = "+str(g2_real))
1151     print("n_S = "+str(qt.expect(n_S, result.states[-1])))
1152     print("p_S = "+str(eta_S*qt.expect(n_S, result.states[-1])))
1153     print("n_aS = "+str(qt.expect(n_aS, result.states[-1])))
1154     print("p_aS = "+str(eta_aS*qt.expect(n_aS, result.states[-1])))
1155     print("n_S_aS = "+str(qt.expect(n_S_aS, result.states[-1])))
1156
1157     return g2_ideal, g2_real
1158
1159 ##### Laser pulse definition: #####
1160 def gaussianPulse(A, t, t0, sig, delta):
1161     x=A*np.exp(-((t-t0)**2)/(2*sig**2))*np.exp(-1j*delta*t)
1162     return x
1163
1164 ##### Realistic detection definitions: #####
1165 def Dx(eta, pdc, a, expOrder=5):
1166     "Takes the efficiency, dark count rate, annihilation operator, and order of the Taylor
1167     expansion. Returns realistic number operator"
1168     D = 1 - (1-pdc) * binomTerm(eta, a, expOrder)
1169     return D
1170
1171 def binomTerm(eta, a, expOrder):
1172     operator = 0
1173     for k in range(expOrder+1):
1174         operator = operator + ((np.log(1-eta)**k)/(np.math.factorial(k)))*(a.dag()*a)**k
1175     return operator
1176
1177 def DxDx(eta, pdc, a, expOrder=5):
1178     "I'm not sure I'm handling the operator ordering correctly"
1179     D = 2*Dx(eta/2, pdc, a, expOrder) - 1 + ((1-pdc)**2)*binomTerm(eta, a, expOrder)
1180     return D
1181
1182 def g2_AutoCor_ideal(a, psi):
1183     "Returns second order autocorrelation function under ideal detection for mode described by a"
1184     g2 = (qt.expect(a.dag()*a.dag()*a*a, psi))/(qt.expect(a.dag()*a, psi)**2)
1185     return g2
1186
1187 def g2_AutoCor_realistic(eta, pdc, a, psi, expOrder = 5):
1188     "Returns second order autocorrelation function under realistic detection conditions for mode
1189     described by a"
1190     g2 = qt.expect(DxDx(eta, pdc, a, expOrder), psi)/(qt.expect(Dx(eta/2, pdc, a, expOrder), psi)**2)
1191     return g2
1192
1193 def g2_CrossCor_ideal(a_x, a_y, psi):
1194     n_x = a_x.dag()*a_x
1195     n_y = a_y.dag()*a_y
1196     n_xy = a_x.dag()*a_y.dag()*a_y*a_x
1197     g2 = qt.expect(n_xy, psi)/(qt.expect(n_x, psi)*qt.expect(n_y, psi))
1198     return g2
1199
1200 def g2_CrossCor_realistic(eta_x, pdc_x, a_x, eta_y, pdc_y, a_y, psi, expOrder=5):
1201     D_x = Dx(eta_x, pdc_x, a_x, expOrder)
1202     D_y = Dx(eta_y, pdc_y, a_y, expOrder)
1203     D_xy = D_x * D_y
1204     g2 = qt.expect(D_xy, psi)/(qt.expect(D_x, psi)*qt.expect(D_y, psi))

```



---

```
1206     return g2
1208 if __name__ == "__main__":
    main()
```



# Bibliography

- [1] M. Planck, *Verh. Deut. Phys. Ges* **2**, 202 (1900).
- [2] M. Planck, *Annalen der physik* **4**, 1 (1901).
- [3] A. Einstein, *Annalen der physik* **4** (1905).
- [4] R. H. Brown, R. Q. Twiss, *The London, Edinburgh, and Dublin Philosophical Magazine and Journal of Science* **45**, 663 (1954).
- [5] R. H. Brown, R. Q. Twiss, *Nature* **177**, 27 (1956).
- [6] R. H. Brown, R. Twiss, *Nature* **178**, 1447 (1956).
- [7] R. J. Glauber, *Physical Review* **131**, 2766 (1963).
- [8] R. J. Glauber, *Physical Review* **130**, 2529 (1963).
- [9] R. J. Glauber, *Physical Review Letters* **10**, 84 (1963).
- [10] C. V. Raman, K. S. Krishnan, *Nature* **121**, 501 (1928).
- [11] D. N. Klyshko, *Sov. J. Quantum Electron.* **7**, 755 (1977).
- [12] M. Kasparczyk, A. Jorio, E. Neu, P. Maletinsky, L. Novotny, *Optics Letters* **40**, 2393 (2015).
- [13] M. Kasparczyk, *et al.*, *Phys. Rev. Lett.* **117**, 243603 (2016).
- [14] K. C. Lee, *et al.*, *Nat. Photon.* **6**, 41 (2012).
- [15] D. G. England, P. J. Bustard, J. Nunn, R. Lausten, B. J. Sussman, *Phys. Rev. Lett.* **111**, 243601 (2013).
- [16] D. G. England, *et al.*, *Phys. Rev. Lett.* **114**, 053602 (2015).
- [17] K. A. G. Fisher, *et al.*, *Phys. Rev. A* **96**, 012324 (2017).
- [18] P. J. Bustard, *et al.*, *Opt. Lett.*, *OL* **40**, 922 (2015).
- [19] K. A. G. Fisher, *et al.*, *Nat. Commun.* **7**, 11200 (2016).

## Bibliography

---

- [20] P. J. Bustard, D. G. England, K. Heshami, C. Kupchak, B. J. Sussman, *Phys. Rev. A* **95**, 053816 (2017).
- [21] D. J. Griffiths, D. F. Schroeter, *Introduction to quantum mechanics* (Cambridge University Press, 2018).
- [22] M. Fox, *Quantum optics: an introduction*, vol. 15 (OUP Oxford, 2006).
- [23] M. J. Stevens, S. Glancy, S. W. Nam, R. P. Mirin, *Optics express* **22**, 3244 (2014).
- [24] P. Sekatski, *et al.*, *J. Phys. B At. Mol. Opt. Phys.* **45**, 124016 (2012).
- [25] M. Reid, D. Walls, *Phys. Rev. A* **34**, 1260 (1986).
- [26] H. Paul, *Reviews of Modern Physics* **54**, 1061 (1982).
- [27] H. J. Kimble, M. Dagenais, L. Mandel, *Physical Review Letters* **39**, 691 (1977).
- [28] A. B. Klimov, S. M. Chumakov, *A group-theoretical approach to quantum optics: models of atom-field interactions* (John Wiley & Sons, 2009).
- [29] A. Einstein, B. Podolsky, N. Rosen, *Phys. Rev.* **47**, 777 (1935).
- [30] J. S. Bell, *Physics* **1**, 195 (1964).
- [31] A. Aspect, P. Grangier, G. Roger, *Phys. Rev. Lett.* **47**, 460 (1981).
- [32] A. Aspect, J. Dalibard, G. Roger, *Phys. Rev. Lett.* **49**, 1804 (1982).
- [33] A. Aspect, P. Grangier, G. Roger, *Phys. Rev. Lett.* **49**, 91 (1982).
- [34] N. Brunner, D. Cavalcanti, S. Pironio, V. Scarani, S. Wehner, *Reviews of Modern Physics* **86**, 419 (2014).
- [35] T. Von Foerster, R. Glauber, *Physical Review A* **3**, 1484 (1971).
- [36] C. A. Parra-Murillo, M. F. Santos, C. H. Monken, A. Jorio, *Phys. Rev. B* **93**, 125141 (2016).
- [37] M. K. Schmidt, R. Esteban, A. González-Tudela, G. Giedke, J. Aizpurua, *ACS Nano* **10**, 6291 (2016).
- [38] A. Saraiva, *et al.*, *Phys. Rev. Lett.* **119**, 193603 (2017).
- [39] T. P. Purdy, K. E. Grutter, K. Srinivasan, J. M. Taylor, *Science* **356**, 1265 (2017).
- [40] V. Sudhir, *et al.*, *Phys. Rev. X* **7**, 031055 (2017).
- [41] R. Riedinger, *et al.*, *Nature* **530**, 313 (2016).
- [42] S. Hong, *et al.*, *Science* **358**, 203 (2017).
- [43] P.-Y. Hou, *et al.*, *Nature Communications* **7**, 11736 (2016).

- 
- [44] P. J. Bustard, R. Lausten, D. G. England, B. J. Sussman, *Phys. Rev. Lett.* **111**, 083901 (2013).
- [45] P. J. Bustard, D. G. England, K. Heshami, C. Kupchak, B. J. Sussman, *Opt. Lett., OL* **41**, 5055 (2016).
- [46] R. J. Glauber, *Phys. Rev.* **130**, 2529 (1963).
- [47] C. Galland, N. Sangouard, N. Piro, N. Gisin, T. J. Kippenberg, *Phys. Rev. Lett.* **112**, 143602 (2014).
- [48] A. Kuzmich, *et al.*, *Nature* **423**, 01714 (2003).
- [49] M. S. Liu, L. A. Bursill, S. Prawer, R. Beserman, *Phys. Rev. B* **61**, 3391 (2000).
- [50] S. Yampolsky, *et al.*, *Nat Photon* **8**, 650 (2014).
- [51] A. Divochiy, *et al.*, *Nat. Photonics* **2**, nphoton.2008.51 (2008).
- [52] E. A. Dauler, *et al.*, *J. Mod. Opt.* **56**, 364 (2009).
- [53] M. J. Fitch, B. C. Jacobs, T. B. Pittman, J. D. Franson, *Phys. Rev. A* **68**, 043814 (2003).
- [54] J. Kim, S. Takeuchi, Y. Yamamoto, H. H. Hogue, *Appl. Phys. Lett.* **74**, 902 (1999).
- [55] A. J. Miller, S. W. Nam, J. M. Martinis, A. V. Sergienko, *Appl. Phys. Lett.* **83**, 791 (2003).
- [56] H. Wang, *et al.*, *Phys. Rev. Lett.* **101**, 240401 (2008).
- [57] H. Flayac, V. Savona, *Phys. Rev. Lett.* **113**, 143603 (2014).
- [58] V. C. Vivoli, T. Barnea, C. Galland, N. Sangouard, *Phys. Rev. Lett.* **116**, 070405 (2016).
- [59] M. M. Wilde, J. M. McCracken, A. Mizel, *Proc. R. Soc. Lond. Math. Phys. Eng. Sci.* **466**, 1347 (2010).
- [60] E. J. O'Reilly, A. Olaya-Castro, *Nat. Commun.* **5**, 3012 (2014).
- [61] D. F. Walls, *Zeitschrift für Physik A Hadrons and nuclei* **237**, 224 (1970).
- [62] D. F. Walls, *Zeitschrift für Physik A Hadrons and nuclei* **244**, 117 (1971).
- [63] T. von Foerester, R. J. Glauber, *Phys. Rev. A* **3**, 1484 (1971).
- [64] J. Mostowski, M. Raymer, *Optics Communications* **36**, 237 (1981).
- [65] M. G. Raymer, J. Mostowski, *Phys. Rev. A* **24**, 1980 (1981).
- [66] M. G. Raymer, I. A. Walmsley, J. Mostowski, B. Sobolewska, *Phys. Rev. A* **32**, 332 (1985).
- [67] I. A. Walmsley, M. G. Raymer, *Phys. Rev. Lett.* **50**, 962 (1983).
- [68] M. G. Raymer, Z. W. Li, I. A. Walmsley, *Phys. Rev. Lett.* **63**, 1586 (1989).

## Bibliography

---

- [69] K. C. Lee, *et al.*, *Science* **334**, 1253 (2011).
- [70] K. C. Lee, *et al.*, *Nature Photonics* **6**, 41 (2012).
- [71] K. A. Fisher, *et al.*, *Nature Communications* **7**, 5 (2016).
- [72] F. Waldermann, *et al.*, *Phys. Rev. B* **78**, 155201 (2008).
- [73] S. Meiselman, O. Cohen, M. F. DeCamp, V. O. Lorenz, *Journal of the Optical Society of America B* **31**, 2131 (2014).
- [74] S. T. Velez, V. Sudhir, N. Sangouard, C. Galland, *Science Advances* **6**, eabb0260 (2020).
- [75] K. Thapliyal, J. Peřina Jr, *Physical Review A* **103**, 033708 (2021).
- [76] R. A. Diaz, C. Monken, A. Jorio, M. F. Santos, *Physical Review B* **102**, 134304 (2020).
- [77] K. Shinbrough, Y. Teng, B. Fang, V. O. Lorenz, O. Cohen, *Phys. Rev. A* **101**, 013415 (2020).
- [78] P. Roelli, C. Galland, N. Piro, T. J. Kippenberg, *Nat. Nano.* **11**, 164 (2016).
- [79] Y. Zhang, J. Aizpurua, R. Esteban, *ACS Photonics* **7**, 1676 (2020).
- [80] M. K. Schmidt, R. Esteban, G. Giedke, J. Aizpurua, A. Gonzalez-Tudela, *Quantum Science and Technology* (2021).
- [81] D. W. Oxtoby, *Annual Review of Physical Chemistry* **32**, 77 (1981).
- [82] B. Schrader, *Infrared and Raman spectroscopy: methods and applications* (John Wiley & Sons, 2008).
- [83] D. A. Long, *The Raman Effect* (John Wiley & Sons, Ltd, 2002), pp. 85–152.
- [84] E. Le Ru, P. Etchegoin, *Principles of Surface-Enhanced Raman Spectroscopy: and related plasmonic effects* (Elsevier, 2008).
- [85] L. Sun, *et al.*, *Nano Letters* **21**, 1434 (2021). PMID: 33508204.
- [86] R. Beams, L. G. Cancado, S.-H. Oh, A. Jorio, L. Novotny, *Phys. Rev. Lett.* **113**, 186101 (2014).
- [87] L. G. Cancado, R. Beams, A. Jorio, L. Novotny, *Phys. Rev. X* **4**, 031054 (2014).
- [88] R. S. Alencar, *et al.*, *Nano Letters* **19**, 7357 (2019). PMID: 31469281.
- [89] M. D. Anderson, *et al.*, *Physical Review Letters* **120**, 233601 (2018).
- [90] C. K. Wu, G. B. B. M. Sutherland, *The Journal of Chemical Physics* **6**, 114 (1938).
- [91] A. Laubereau, G. Wochner, W. Kaiser, *Optics Communications* **17**, 91 (1976).
- [92] J. Konarska, *et al.*, *Physical Chemistry Chemical Physics* **18**, 16046 (2016).

- 
- [93] J. R. Johansson, P. D. Nation, F. Nori, *Computer Physics Communications* **183**, 1760 (2012).
- [94] J. R. Johansson, P. D. Nation, F. Nori, *Comp. Phys. Comm* **184**, 1234 (2013).
- [95] S. T. Velez, *et al.*, *Physical Review X* **9**, 41007 (2019).
- [96] S. Hong, *et al.*, *Science* **358**, 203 (2017).
- [97] G. Vidal, R. F. Werner, *Physical Review A* **65**, 032314 (2002).
- [98] M. B. Plenio, *Physical review letters* **95**, 090503 (2005).
- [99] K. Mølmer, *Physical Review A* **55**, 3195 (1997).
- [100] S. D. BARTLETT, T. RUDOLPH, R. W. SPEKKENS, *International Journal of Quantum Information* **04**, 17 (2006).
- [101] A. Karnieli, N. Rivera, A. Arie, I. Kaminer, *Science Advances* **7** (2021).
- [102] K. E. Dorfman, S. Mukamel, *Proceedings of the National Academy of Sciences* **115**, 1451 (2018).
- [103] J. Galego, F. J. Garcia-Vidal, J. Feist, *Phys. Rev. X* **5**, 041022 (2015).
- [104] F. C. Spano, *The Journal of Chemical Physics* **142**, 184707 (2015).
- [105] F. Herrera, F. C. Spano, *Phys. Rev. Lett.* **116**, 238301 (2016).
- [106] A. G. Avramenko, A. S. Rury, *The Journal of Physical Chemistry C* **123**, 30551 (2019).
- [107] A. Shalabney, *et al.*, *Angewandte Chemie International Edition* **54**, 7971 (2015).
- [108] J. del Pino, J. Feist, F. J. Garcia-Vidal, *The Journal of Physical Chemistry C* **119**, 29132 (2015).
- [109] J. del Pino, F. J. Garcia-Vidal, J. Feist, *Phys. Rev. Lett.* **117**, 277401 (2016).
- [110] A. Strashko, J. Keeling, *Phys. Rev. A* **94**, 023843 (2016).
- [111] P. Roelli, D. Martin-Cano, T. J. Kippenberg, C. Galland, *Phys. Rev. X* **10**, 031057 (2020).
- [112] S. Hughes, A. Settineri, S. Savasta, F. Nori, *arXiv* p. 2103.08670 (2021).
- [113] R. F. Ribeiro, L. A. Martínez-Martínez, M. Du, J. Campos-Gonzalez-Angulo, J. Yuen-Zhou, *Chem. Sci.* **9**, 6325 (2018).
- [114] A. H. Compton, *Phys. Rev.* **21**, 483 (1923).
- [115] D. von der Linde, J. Kuhl, H. Klingenberg, *Phys. Rev. Lett.* **44**, 1505 (1980).
- [116] J. A. Kash, J. C. Tsang, J. M. Hvam, *Physical Review Letters* **54**, 2151 (1985).

## Bibliography

---

- [117] D. Song, *et al.*, *Physical Review Letters* **100**, 225503 (2008).
- [118] T. Jiang, *et al.*, *Nano Lett.* **18**, 2590 (2018).
- [119] S. Mukamel, *Principles of nonlinear optical spectroscopy*, vol. 29 (Oxford university press New York, 1995).
- [120] K. C. Lee, *et al.*, *Diamond and Related Materials* **19**, 1289 (2010).
- [121] G. A. Garrett, A. G. Rojo, A. K. Sood, J. F. Whitaker, R. Merlin, *Science* **275**, 1638 (1997).
- [122] K. C. Lee, *et al.*, *Science* **334**, 1253 (2011).
- [123] M. Aspelmeyer, T. J. Kippenberg, F. Marquardt, *Rev. Mod. Phys.* **86**, 1391 (2014).
- [124] J. Cripe, *et al.*, *Nature* **568**, 364 (2019).
- [125] E. E. Wollman, *et al.*, *Science* **349**, 952 (2015).
- [126] R. Riedinger, *et al.*, *Nature* **556**, 473 (2018).
- [127] C. F. Ockeloen-Korppi, *et al.*, *Nature* **556**, 478 (2018).
- [128] Y. Chu, *et al.*, *Nature* **563**, 666 (2018).
- [129] L. M. Duan, M. D. Lukin, J. I. Cirac, P. Zoller, *Nature* **414**, 413 (2001).
- [130] P. Grangier, G. Roger, A. Aspect, *EPL* **1**, 173 (1986).
- [131] L. Mandel, E. Wolf, *Optical Coherence and Quantum Optics* (Cambridge University Press, 1995).
- [132] I. Marinković, *et al.*, *Phys. Rev. Lett.* **121**, 220404 (2018).
- [133] T. von Foerster, R. J. Glauber, *Phys. Rev. A* **3**, 1484 (1971).
- [134] N. Bloembergen, *Nonlinear Optics* (W. A. Benjamin, 1965).
- [135] M. D. Anderson, *et al.*, *Phys. Rev. Lett.* **120**, 233601 (2018).
- [136] A. Weinstein, *et al.*, *Phys. Rev. X* **4**, 041003 (2014).
- [137] E. Knill, R. Laflamme, G. J. Milburn, *Nature* **409**, 46 (2001).
- [138] A. L. Lacaita, F. Zappa, S. Bigliardi, M. Manfredi, *IEEE Transactions on Electron Devices* **40**, 577 (1993).
- [139] S. Friberg, C. K. Hong, L. Mandel, *Opt. Comm.* **54**, 311 (1985).
- [140] M. Brune, *et al.*, *Phys. Rev. Lett.* **101**, 240402 (2008).
- [141] P. Klemens, *Physical Review* **148**, 845 (1966).



- 
- [142] A. Debernardi, S. Baroni, E. Molinari, *Physical review letters* **75**, 1819 (1995).
- [143] F. Benz, *et al.*, *Science* **354**, 726 (2016).
- [144] A. Lombardi, *et al.*, *Phys. Rev. X* **8**, 011016 (2018).
- [145] A. Jorio, *et al.*, *Nano Lett.* **14**, 5687 (2014).
- [146] L. Chen, *et al.*, *Science* **363**, 158 (2019).
- [147] J. F. Clauser, M. A. Horne, A. Shimony, R. A. Holt, *Phys. Rev. Lett.* **23**, 880 (1969).
- [148] S. J. Freedman, J. F. Clauser, *Phys. Rev. Lett.* **28**, 938 (1972).
- [149] C.-W. Chou, *et al.*, *Science* **316**, 1316 (2007).
- [150] J. Hofmann, *et al.*, *Science* **337**, 72 (2012).
- [151] R. Blatt, D. Wineland, *Nature* **453**, 1008 (2008).
- [152] D. N. Matsukevich, *et al.*, *Phys. Rev. Lett.* **95**, 040405 (2005).
- [153] L. Li, O. Dudin, A. Kuzmich, *Nature* **498**, 466 (2013).
- [154] N. J. Engelsen, R. Krishnakumar, O. Hosten, M. Kasevich, *Phys. Rev. Lett.* **118**, 140401 (2017).
- [155] M. Ansmann, *et al.*, *Nature* **461**, 504 (2009).
- [156] L. DiCarlo, *et al.*, *Nature* **467**, 574 (2010).
- [157] J. P. Dehollain, *et al.*, *Nat. Nano.* **11**, 242 (2016).
- [158] B. Hensen, *et al.*, *Nature* **526**, 682 (2015).
- [159] A. Jorio, *et al.*, *Phys. Status Solidi B* **252**, 2380 (2015).
- [160] D. G. England, *et al.*, *Phys. Rev. Lett.* **117**, 073603 (2016).
- [161] S. T. Velez, *et al.*, *Phys. Rev. X* **9**, 041007 (2019).
- [162] H. De Riedmatten, *et al.*, *Phys. Rev. Lett.* **97**, 113603 (2006).
- [163] I. Marcikic, *et al.*, *Phys. Rev. A* **66**, 062308 (2002).
- [164] J.-D. Bancal, K. Redeker, P. Sekatski, W. Rosenfeld, N. Sangouard, Device-independent certification of an elementary quantum network link (2018).
- [165] D. Berry, H. Jeong, M. Stobinska, T. C. Ralph, *Phys. Rev. A* **81**, 012109 (2010).
- [166] D. Orsucci, J.-D. Bancal, N. Sangouard, P. Sekatski, *Quantum* **4**, 238 (2020).
- [167] A. H. Ghadimi, *et al.*, *Science* **360**, 764 (2018).

## Bibliography

---

- [168] M. Żukowski, A. Zeilinger, M. A. Horne, A. K. Ekert, *Phys. Rev. Lett.* **71**, 4287 (1993).
- [169] J. T. Hill, A. H. Safavi-Naeini, J. Chan, O. Painter, *Nat. Commun.* **3**, 1196 (2012).
- [170] L. Chen, *et al.*, *Science* **363**, 158 (2018).
- [171] S. S. Kondov, *et al.*, *Nat. Phys.* **15**, 1118 (2019).
- [172] C. P. Koch, M. Lemesko, D. Sugny, *Reviews of Modern Physics* **91**, 035005 (2019).
- [173] V. V. Albert, J. P. Covey, J. Preskill, *Physical Review X* **10**, 031050 (2020).
- [174] A. Maser, B. Gmeiner, T. Utikal, S. Götzinger, V. Sandoghdar, *Nat Photon* **10**, 450 (2016).
- [175] D. Riedel, S. Flågan, P. Maletinsky, R. J. Warburton, *Phys. Rev. Applied* **13**, 014036 (2020).
- [176] A. Halpin, *et al.*, *Nat. Chem.* **6**, 196 (2014).
- [177] H.-G. Duan, *et al.*, *Proc Natl Acad Sci U S A* **114**, 8493 (2017).
- [178] Z. Ou, S. F. Pereira, H. Kimble, K. Peng, *Physical Review Letters* **68**, 3663 (1992).
- [179] S. Mancini, V. Giovannetti, D. Vitali, P. Tombesi, *Physical review letters* **88**, 120401 (2002).
- [180] L.-M. Duan, G. Giedke, J. I. Cirac, P. Zoller, *Physical Review Letters* **84**, 2722 (2000).
- [181] B. Julsgaard, A. Kozhekin, E. S. Polzik, *Nature* **413**, 400 (2001).
- [182] C. Silberhorn, *et al.*, *Physical Review Letters* **86**, 4267 (2001).
- [183] J. C. Howell, R. S. Bennink, S. J. Bentley, R. W. Boyd, *Physical Review Letters* **92**, 210403 (2004).
- [184] A. C. Dada, J. Leach, G. S. Buller, M. J. Padgett, E. Andersson, *Nature Physics* **7**, 677 (2011).
- [185] B. Eckmann, *et al.*, *Optics Express* **28**, 31553 (2020).
- [186] F. S. de Aguiar Júnior, *et al.*, *Physical Review B* **99**, 100503 (2019).
- [187] F. S. de Aguiar Júnior, M. F. Santos, C. H. Monken, A. Jorio, *Physical Review Research* **2**, 013084 (2020).
- [188] X.-Q. Yan, X.-L. Zhang, S. Shi, Z.-B. Liu, J.-G. Tian, *Optics express* **19**, 5559 (2011).
- [189] S. Ikawa, E. Whalley, *The Journal of Chemical Physics* **86**, 1836 (1987).
- [190] R. A. Diaz, C. Monken, A. Jorio, M. F. Santos, *Physical Review B* **102**, 134304 (2020).
- [191] S. Anand, P. Verma, K. Jain, S. Abbi, *Physica B: Condensed Matter* **226**, 331 (1996).
- [192] M. Kuball, J. Hayes, Y. Shi, J. Edgar, *Applied Physics Letters* **77**, 1958 (2000).

- [193] J. Pomeroy, *et al.*, *Applied Physics Letters* **86**, 223501 (2005).
- [194] H. Zhang, *et al.*, *Nature Photonics* **5**, 628 (2011).
- [195] A. Trügler, U. Hohenester, *Physical Review B* **77**, 115403 (2008).
- [196] E. Le Ru, P. Etchegoin, *Principles of Surface-Enhanced Raman Spectroscopy: and related plasmonic effects* (Elsevier, 2008).



## Santiago Tarragó Vélez

Email: [santi\\_tarrago@hotmail.com](mailto:santi_tarrago@hotmail.com)

### **EDUCATION**

July 2017- August 2021	<b>PhD in Physics</b>
	École Polytechnique Fédérale de Lausanne, Vaud, Switzerland.
	Laboratory of Quantum Nano-Optics Adviser: Prof. Christophe Galland Thesis: “Studying non-classical phonon states by single photon time-correlated Raman spectroscopy” Area of Study: Quantum Optics, Photonics, Optomechanics, Spectroscopy
September 2011- December 2015	<b>Bachelors degree in Engineering Physics</b>
	Universidad Iberoamericana, Mexico City, Mexico.
	Graduated with an honorable mention, and a GPA of 9.74/10

### **WORK AND RESEARCH EXPERIENCE**

February 2020 – February 2021	<b>President</b>
	EPFL Photonics Chapter
	<ul style="list-style-type: none"><li>• President of the Optical Society of America (OSA) and The International Society for Optical Engineering (SPIE) student chapters at École Polytechnique Fédérale de Lausanne.</li></ul>
October 2016 – June 2017	<b>Trainee in the Magnets Project Team</b>
	The European Joint Undertaking for ITER and the Development of Fusion Energy (Fusion for Energy)
	<ul style="list-style-type: none"><li>• Preliminary checks on the magnetic measurements meant to model the Toroidal Field Coils, as well as help assess potential sources of error and estimate their effect.</li><li>• Analysis on the results on mechanical and welding deformation simulations.</li></ul>
October 2011 – August 2016	<b>Research Student</b>
	Nanoscience and Nanotechnology Laboratory, Universidad Iberoamericana
	<ul style="list-style-type: none"><li>• Synthesis of decorated multi-walled carbon nanotubes (MWCNTs)</li><li>• Synthesis of single and few-layered MoS<sub>2</sub> and MoSe<sub>2</sub> nanostructures.</li></ul>

	<ul style="list-style-type: none"> <li>Characterization of samples by electronic microscopy, EDX, and Raman spectroscopy.</li> </ul>
August 2015 – February 2016	<b>Research Assistant</b> Social Service at the Research Unit on Metabolic Diseases, Mexican Institute of Social Security <ul style="list-style-type: none"> <li>Designing, testing and troubleshoot an ELISA assays to detect IAPP oligomers for early diabetes detection.</li> </ul>
May 2015 – August 2015	<b>Research Intern</b> Superconducting Quantum Device Group, Institute for Quantum Computing, University of Waterloo. Joined as part of the MITACS Globalink Research Internship 2015 <ul style="list-style-type: none"> <li>Designing and modelling magnetic shields for use inside a dilution refrigerator using finite element methods.</li> <li>Assist in designing the experimental setup inside the cryostat.</li> </ul>

## **PUBLICATIONS AND PRESENTATIONS**

<b>Publications</b>	<p><b>Tarrago Velez, Santiago</b>, Anna Pogrebna, and Christophe Galland. "Collective Vibrational Quantum Coherence in a Molecular Liquid under Spontaneous Raman Scattering." arXiv preprint arXiv:2105.00213 (2021).</p> <p><b>Tarrago Velez, Santiago</b>, Vivishek Sudhir, Nicolas Sangouard, and Christophe Galland. "Bell correlations between light and vibration at ambient conditions." Science Advances 6, no. 51 (2020): eabb0260.</p> <p><b>Tarrago Velez, Santiago</b>, Kilian Seibold, Nils Kipfer, Mitchell D. Anderson, Vivishek Sudhir, and Christophe Galland. "Preparation and decay of a single quantum of vibration at ambient conditions." Physical Review X 9, no. 4 (2019): 041007.</p> <p>Anderson, Mitchell D., <b>Santiago Tarrago Velez</b>, Kilian Seibold, Hugo Flayac, Vincenzo Savona, Nicolas Sangouard, and Christophe Galland. "Two-color pump probe measurement of photonic quantum correlations mediated by a single phonon." Physical review letters 120, no. 23 (2018): 233601.</p> <p>Cecilia Mercado-Zúñiga, Carlos Torres-Torres, Martin Trejo-Valdez, Reydezel Torres-Martínez, <b>Santiago Tarrago Velez</b>, Felipe Cervantes-Sodi, and Jorge Roberto Vargas García. "Mechano-optic regulation of photoconduction in functionalized carbon nanotubes decorated with platinum" International Journal of Photoenergy, 2014.</p>
<b>Oral Presentations</b>	<p>"Bell Correlations Between Light and Vibrations at Ambient Condition" CLEO Europe. Virtual. 21/06/2021 – 25/06/2021</p>

	<p>“Bell correlations between light and vibrations at ambient conditions”. Q-Turn. Virtual. 23/11/2020 – 27/11/2020</p> <p>“Single Photon Counting and Light-Vibration Entanglement”. Single Photon based Quantum Technologies. Virtual. 15/09/2020 – 17/09/2020</p> <p>“Preparing and measuring non-classical states of room temperature phonons”. QSIT Junior Meeting. Flumserberg, Switzerland. 03/06/2019 – 06/06/2019</p> <p>“Heralded single-phonon preparation in diamond”. Symposium Latsis 2019 on Diamond Photonics LATSIS2019. Lausanne, Switzerland. 19/05/2019 – 22/05/2019</p> <p>“Preparation and detection of a phonon Fock state at room temperature”. European Quantum Technologies Conference. Grenoble, France. 17/02/2019 – 22/02/2019</p> <p>“Towards an optomechanical Bell test with room temperature phonons: Phonon mediated correlations and sub-Poissonian statistics”. Heraus Seminar - Advances in open systems and fundamental tests of quantum mechanics. Bad-Honnef, Germany. 02/12/2018 – 05/12/2018</p> <p>“Ultrafast photonic quantum correlations mediated by individual phonons” SPIE Photonics. Strasbourg. 22/04/2018 – 26/04/2018</p> <p>“Silicon doped single walled carbon nanotubes: Synthesis and characterization” International Congress on Applications of Nanotechnology (ICANano). Mexico City. 2014</p>
--	------------------------------------------------------------------------------------------------------------------------------------------------------------------------------------------------------------------------------------------------------------------------------------------------------------------------------------------------------------------------------------------------------------------------------------------------------------------------------------------------------------------------------------------------------------------------------------------------------------------------------------------------------------------------------------------------------------------------------------------------------------------------------------------------------------------------------------------------------------------------------------------------------------------------------------------------------------------------------------------------------------------------------------------------------------------------------------------------------------------------------------------------------------------------------------------------------------------------------------------------------------------------------------------------------------------------------------------------------------